

PE&RS

July 2022

Volume 88, Number 7

Celebrating

50

YEARS

Landsat

1972-2022

Las Vegas, NV

September 13, 1972

Landsat 1

path/row 42/35

band combination 7|5|4

Las Vegas, NV

April 30, 2022

Landsat 9

path/row 39/35

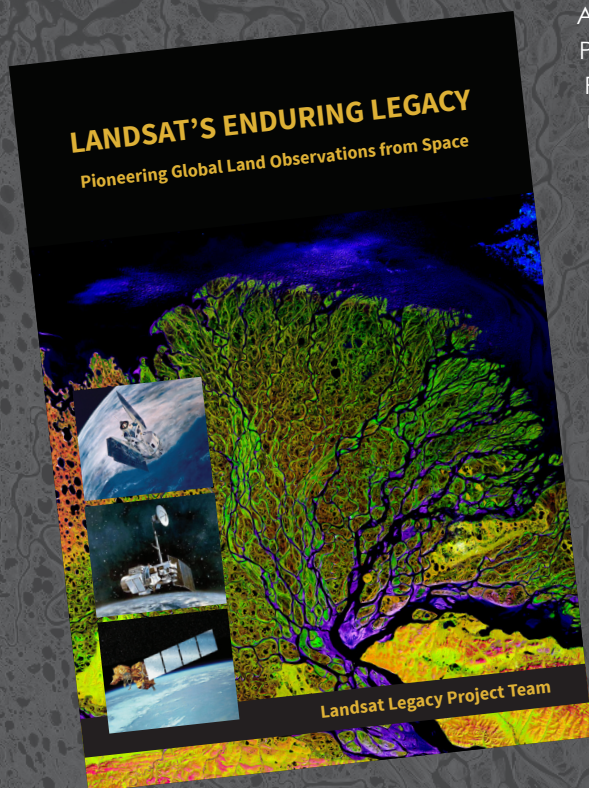
band combination 5|4|3

PHOTOGRAMMETRIC ENGINEERING & REMOTE SENSING

The official journal for imaging and geospatial information science and technology

LANDSAT'S ENDURING LEGACY

PIONEERING GLOBAL LAND OBSERVATIONS FROM SPACE



After more than 15 years of research and writing, the Landsat Legacy Project Team published, in collaboration with the American Society for Photogrammetry and Remote Sensing (ASPRS), a seminal work on the nearly half-century of monitoring the Earth's lands with Landsat. Born of technologies that evolved from the Second World War, Landsat not only pioneered global land monitoring but in the process drove innovation in digital imaging technologies and encouraged development of global imagery archives. Access to this imagery led to early breakthroughs in natural resources assessments, particularly for agriculture, forestry, and geology. The technical Landsat remote sensing revolution was not simple or straightforward. Early conflicts between civilian and defense satellite remote sensing users gave way to disagreements over whether the Landsat system should be a public service or a private enterprise. The failed attempts to privatize Landsat nearly led to its demise. Only the combined engagement of civilian and defense organizations ultimately saved this pioneer satellite land monitoring program. With the emergence of 21st century Earth system science research, the full value of the Landsat concept and its continuous 45-year global archive has been recognized and embraced. Discussion of Landsat's future continues but its heritage will not be forgotten.

The pioneering satellite system's vital history is captured in this notable volume on Landsat's Enduring Legacy.

Landsat Legacy Project Team

Samuel N. Goward
Darrel L. Williams
Terry Arvidson
Laura E. P. Rocchio
James R. Irons
Carol A. Russell
Shaida S. Johnston

Landsat's Enduring Legacy

Hardback, 2017, ISBN 1-57083-101-7

Student	\$36*
Member	\$48*
Non-member	\$60*

* Plus shipping

Order online at
www.asprs.org/landsat



asprs THE IMAGING & GEOSPATIAL
INFORMATION SOCIETY

ANNOUNCEMENTS

URISA is pleased to invite applications for its Vanguard Cabinet. The Vanguard Cabinet (VC), a URISA initiative, is an advisory board made up of passionate, young (35 years of age or younger) geospatial professionals who strive to engage young practitioners, increase their numbers in the organization, and better understand the concerns facing these future leaders of the geospatial community. The VC's mission is to collaborate with URISA's Board of Directors and URISA committees in creating and promoting programs and policies of benefit to young professionals and to enhance overall innovation, collaboration, networking, and professional development opportunities.

From managing a mentoring program and supporting student competitions to serving as committee leaders, conference chairs, and even being elected to the URISA Board of Directors, these professionals are the next generation of GIS leaders, providing valuable direction and enthusiasm to the community.

Applications are due on or before July 22, 2022 and will be reviewed by URISA's Leadership Development Committee. Each accepted applicant will serve a three-year term.

Learn more about URISA Vanguard Cabinet activities and access the application here: <https://www.urisa.org/vanguard-cabinet>.



Phase One, a leading developer of digital imaging technologies, announced its next-generation aerial mapping solutions. The Phase One PAS 880 oblique and PAS 280 nadir systems have been enhanced with 150MP near-infrared (NIR) sensors and the most productive workflow with the launch of the latest iX Suite SW solution.

The new PAS 880i offers the same outstanding image quality and unsurpassed image capture rate (2 frames/second) that gained its forerunner a reputation for reliability and productivity. The PAS 880i covers a wide swath across-track: more than 20,000 pixels in nadir and 14,000 pixels in each of the obliques, operated at a variety of airspeeds, altitudes, and lighting conditions.

"Already the most productive large-format aerial solution, the PAS 880i is now also the most versatile," said Anthony Garetto, VP, Phase One Geospatial. "Users have the option of operating the PAS 880i in full nadir/oblique mode for wide-area mapping and 3D city modeling projects, or nadir-only mode for photogrammetric applications. The enhanced PAS 880i now includes a 150MP near-infrared sensor with 50mm lens, adding simultaneous data capture of the near-infrared band for a complete 4-band solution."

Image sensors are one of the fastest developing technologies. Modern Bayer sensors are incredibly efficient and demosaicing algorithms have made huge progress over the last decade.

Phase One has been the leading developer of high-end Bayer processing algorithms and software for almost 30 years and has made it a business priority to keep pushing the limit of Bayer processing quality.

"In aerial mapping, Pan Sharpening is a complicated and cumbersome approach where multiple cameras must be pointed at the same areas on the ground to collect both luminance and color information. With the Bayer pattern sensors that we use at Phase One, this is not necessary resulting in much simpler and more compact systems for the same coverage. Bayer pattern technology provides a much better GSD/Coverage for any given pod size," said Lau Nørgaard, CTO at Phase One

With over 20,000 RGB pixels across flight direction, the PAS 280i is an effective large format aerial solution of 280MP combined with a 150MP NIR camera. This ensures a higher return on investment than other large-format systems. PAS 880i is based on the PAS 280i solution, enabling a seamless upgrade to a full oblique system, ensuring a future-proof and effective investment and flexibility in service offering.

The addition of the NIR sensor to the PAS 880 and PAS 280 solutions expands their utility in applications related to agricultural monitoring, environmental preservation, and land use/land cover programs

Learn more at <https://geospatial.phaseone.com/aerial-systems/>.



TCarta Marine, a global provider of hydrospatial products and services, has announced the formation of TCarta Canada based in Ottawa, Ontario. Offering the complete line of TCarta satellite-derived bathymetry (SDB) services and Trident SDB Toolbox software, the affiliate office is a partnership between TCarta Marine and Prof. Anders Knudby, a well-known marine geospatial researcher and consultant in Canada.

TCarta made the announcement at the Canadian Hydrographic Conference 2022 in Gatineau (Ottawa), Ontario, Canada.

TCarta Canada announced its first contract – a pilot project to update bathymetric navigation charts for Baffin Island's Cape Hooper and Kangok Fjord with SDB technology. The contract is administered by the Canadian Hydrographic Services, which has previously purchased SDB maps from TCarta.

The partnership between TCarta Marine and Knudby is an ideal merger of complementary technologies. Knudby, who will serve as Managing Partner for the new office, has pioneered development of SDB algorithms for Canada's coastal waters as a consultant and associate professor at University of Ottawa. TCarta has recently focused on expanding its SDB techniques for application in Arctic regions. Knudby's algorithms are being incorporated into the TCarta Project Trident SDB workflow.

"TCarta Canada will accelerate our research and push the boundaries for how we deliver marine geospatial products. The Canadian Arctic is an enormous area, difficult to access, often covered in cloud, ice, and darkness, and poorly charted," said Knudby. "But maritime traffic is increasing as the Arctic Sea ice recedes, and mariners crossing these waters need up-to-date information for safe navigation. TCarta Canada will play an important role here, turning satellite imagery into the information products that mariners need."

At the heart of TCarta Canada's offerings will be the new Trident (SDB) Toolbox, now available as a software-as-a-service product. The Toolbox is a series of software applications that operate within Esri ArcGIS Pro and allow organizations to perform their own extraction of bathymetric measurements from satellite, aerial, and UAV imagery.

With offices in the United States and Jamaica, TCarta has built an international business on cost-effectively and safely deriving onshore and offshore data sets using multispectral imagery captured by Earth observation satellites – without negative impact on the natural habitat. TCarta products and services are relied upon by governmental, insurance, oil & gas, environmental, and infrastructure development clients in applications as diverse as natural resource monitoring, tsunami modeling, disaster & hazard response, and hydrologic studies.

For more information, visit www.tcarta.com.

EVENTS

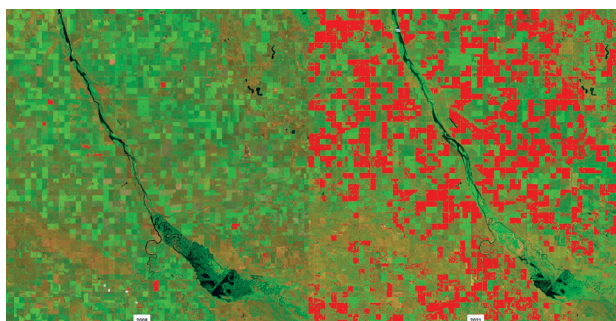
CaGIS proudly presents AutoCarto 2022— Ethics in Mapping: Integrity, Inclusion, and Empathy, the 24th International Research Symposium on cartography and GIScience, with its focus on the intersection of the two. AutoCarto 2022 will take place November 2–4, 2022, with workshops occurring on November 1st), at the Esri Campus in Redlands, California.

AutoCarto 2022 brings attention to the ethical responsibilities we face in all aspects of our practice, provides a forum for discussion on the power of maps and spatial analyses, and highlights opportunities for discussions of integrity, inclusion, and empathy in cartography and GIScience.

For more information, visit <https://cartogis.org/autocarto/autocarto-2022/>.

CALENDAR

- 8-12 August, **URISA GIS Leadership Academy**, Philadelphia, Pennsylvania. For more information, visit www.urisa.org/education-events/urisa-gis-leadership-academy/.
- 23 September, **ASPRS GeoByte — Allen Coral Atlas: A New Technology for Coral Reef Conservation**. For more information, visit <https://www.asprs.org/geobytes.html>.
- 3-6 October, **GIS-PRO 2022**, Boise, Idaho. For more information, visit <https://www.urisa.org/gis-pro>.
- 23-27 October, **Pecora 22**, Denver, Colorado. For more information, visit <https://pecora22.org/>.
- 31 October - 4 November, **URISA GIS Leadership Academy**, Santa Rosa, California. For more information, visit www.urisa.org/education-events/urisa-gis-leadership-academy/.
- 2-4 November, **AutoCarto 2022— Ethics in Mapping: Integrity, Inclusion, and Empathy**, Redlands, California. For more information, visit <https://cartogis.org/autocarto/autocarto-2022/>.



429 Seeing Our Planet Anew: Fifty Years of Landsat

By Thomas R. Loveland, Martha C. Anderson, Justin L. Huntington, James R. Irons, David M. Johnson, Laura E. P. Rocchio, Curtis E. Woodcock, and Michael A. Wulder



421 AmericaView and its Landsat Connection

By Russell G. Congalton, Roberta Lenczowski, Lisa Wirth, and Christopher McGinty

COLUMNS

- 425 GIS Tips & Tricks — Designing Color Style Sheets for your Mobile App — Easier Than You Think
- 427 Grids and Datums Update
This month we look at the Republic of Zambia

ANNOUNCEMENTS

- 428 Signatures
The Column of the Student Advisory Council
- 438 Headquarters News
- 438 New ASPRS Members
Join us in welcoming our newest members to ASPRS.

DEPARTMENTS

- 417 Industry News
- 418 Calendar
- 460 In-Press *PE&RS* Articles
- 487 Who's Who in ASPRS
- 488 ASPRS Sustaining Members

439 Hydrological Topography Data Set (HTD)— The Data Set for High Resolution 2D Urban Flood Modeling

Che-Hao Chang, Chih-Hung Hsu, Chih-Tsung Hsu, Shiang-Jen Wu, and Po-Hsien Chung

This article discusses the demand for better high resolution two-dimensional (2D) hydraulic modeling data and proposes a data set named "Hydrological Topography Data Set" (HTD).

451 Improving Land Cover Classification over a Large Coastal City Through Stacked Generalization with Filtered Training Samples

Feilin Lai and Xiaojun Yang

To improve remote sensing-based land cover mapping over heterogenous landscapes, we developed an ensemble classifier based on stacked generalization with a new training sample refinement technique for the combiner.

461 Evaluation of Urban Vegetation Phenology Using 250 m MODIS Vegetation Indices

Hongxin Zhang, Xiaoyue Wang, and Dailiang Peng

The dynamics of urban vegetation phenology play an important role in influencing human activities. Previous studies have shown high-resolution remote sensing as a tool for urban vegetation mapping, but the low temporal resolution of these data limits their use for phenological modeling. Therefore, it is of great significance to evaluate Moderate Resolution Imaging Spectroradiometer (MODIS) imagery for urban vegetation phenology monitoring.

469 Monocular Video Frame Optimization Through Feature-Based Parallax Analysis for 3D Pipe Reconstruction

Zhihua Xu, Xingzheng Lu, Wenliang Wang, Ershuai Xu, Rongjun Qin, Yiru Niu, Xu Qiao, Feng Yang, and Rui Yan

Structure-from-motion (SfM) techniques have been widely used for three-dimensional (3D) scene reconstruction from sequential video frames. However, for reconstructing narrow and confined spaces such as the interior of drainage pipes, selecting geometrically optimal frames is a major challenge, not only to reduce the number of needed frames but also to yield better geometry. This article introduces a coarse-to-fine method to optimize the selection of monocular video frames based on a geometric criterion called feature-based parallax analysis for 3D pipe reconstruction

479 Monitoring and Analysis of Urban Sprawl Based on Road Network Data and High-Resolution Remote Sensing Imagery: A Case Study of China's Provincial Capitals

Lin Ding, Hanchao Zhang, and Deren Li

The primary prerequisite for sustainable urban development is to accurately grasp the development of the city. The dynamic changes in the urban area can reflect the urban expansion process and spatial development model. Carrying out urban expansion monitoring and extracting urban areas is of great importance for grasping the law of urban development and promoting the sustainable development of cities. However, the related research reveals several problems such as insufficient accuracy and low intelligence of urban boundary extraction. In response to these problems, this article proposes a new method for urban area extraction based on the progressive learning model.

See the Cover Description on Page 420

COVER DESCRIPTION

If you could speed up time and see the changes in a fast-growing city like Las Vegas, what would the future look like? Landsat satellite imagery reveals a stunning view of this type of urban growth. The two Landsat images on this month's front cover were captured nearly 50 years apart. The top image was one of the earliest to come from the first Landsat satellite, then called Earth Resources Technology Satellite (ERTS), which launched as an experiment on July 23, 1972. The bottom image came from the most recent satellite in the series, Landsat 9, which launched September 27, 2021.

Both images use the satellites' color infrared band combinations, with near-infrared, red, and green bands. Because chlorophyll reflects near-infrared light, this band composition is useful for analyzing vegetation. Areas in bright red depict vegetation; urban areas are white or gray; and the darkest areas depict water. A plot of very light tan, indicating land clearing, can sometimes be seen right before a new residential area is built.

Brightly reflected areas outside of the city indicate the presence of salts, minerals, and clays in the sediment. Water once settled in these flat, lower-elevation areas, and the minerals remained. The brown-tan regions surrounding the city are likely steeper slopes where flowing water rinsed out minerals.

Lake Mead, the large body of water to the right in each image, is the largest reservoir in the United States. Lake Mead is part of a system that supplies water to at least 40 million people across seven states and northern Mexico, but it currently stands at its lowest level in almost 80 years. As a result, water will be allocated in much lower amounts to some states this year and possibly into the near future.

The Landsat Program changed the world in 1972, just by looking at it. Early discoveries ranged from mineral deposits and remote fires to unknown islands. Discoveries continue today in new imagery as well as the study of changes in the invaluable and unparalleled 50-year record of Earth surface data. Landsat and its archive will continue to deliver answers about the Earth's resources, their influence on humanity and ecosystems, and humanity's influence on them well into the future.

For more information, please visit <https://www.usgs.gov/landsat-missions>.



PHOTOGRAMMETRIC ENGINEERING & REMOTE SENSING

JOURNAL STAFF

Publisher ASPRS

Editor-In-Chief Alper Yilmaz

Director of Publications Rae Kelley

Electronic Publications Manager/Graphic Artist

Matthew Austin

Photogrammetric Engineering & Remote Sensing is the official journal of the American Society for Photogrammetry and Remote Sensing. It is devoted to the exchange of ideas and information about the applications of photogrammetry, remote sensing, and geographic information systems. The technical activities of the Society are conducted through the following Technical Divisions: Geographic Information Systems, Photogrammetric Applications, Lidar, Primary Data Acquisition, Professional Practice, Remote Sensing Applications, and Unmanned Autonomous Systems Division. Additional information on the functioning of the Technical Divisions and the Society can be found in the Yearbook issue of *PE&RS*.

Correspondence relating to all business and editorial matters pertaining to this and other Society publications should be directed to the American Society for Photogrammetry and Remote Sensing, 8550 United Plaza Boulevard, Suite 1001, Baton Rouge, LA 70809, including inquiries, memberships, subscriptions, changes in address, manuscripts for publication, advertising, back issues, and publications. The telephone number of the Society Headquarters is 301-493-0290; the fax number is 225-408-4422; web address is www.asprs.org.

PE&RS. *PE&RS* (ISSN0099-1112) is published monthly by the American Society for Photogrammetry and Remote Sensing, 425 Barlow Place, Suite 210, Bethesda, Maryland 20814-2144. Periodicals postage paid at Bethesda, Maryland and at additional mailing offices.

SUBSCRIPTION. For the 2022 subscription year, ASPRS is offering two options to our *PE&RS* subscribers—an e-Subscription and the print edition. e-Subscribers can add printed copies to their subscriptions for a small additional charge. Print and Electronic subscriptions are on a calendar-year basis that runs from January through December. We recommend that customers who choose print and e-Subscription with print renew on a calendar-year basis.

The rate for a Print subscription for the USA is \$1105.00 USD, for Canadian* is \$1164.00 USD, and for Non-USA is \$1235.00 USD.

The rate for e-Subscription (digital) Site License for the USA and Non-USA is \$1040.00 USD and for Canadian* is \$1089.00 USD.

The rate for e-Subscription (digital) plus Print for the USA is \$1405.00 USD, for Canadian* is \$1464.00 USD, and for Non-USA is \$1435.00 USD.

*Note: e-Subscription, Print subscription, and e-Subscription plus Print for Canada includes 5% of the total amount for Canada's Goods and Services Tax (GST #135123065). **PLEASE NOTE: All Subscription Agencies receive a 20.00 USD discount.**

POSTMASTER. Send address changes to *PE&RS*, ASPRS Headquarters, 8550 United Plaza Boulevard, Suite 1001, Baton Rouge, LA 70809. CDN CPM #40020812).

MEMBERSHIP. Membership is open to any person actively engaged in the practice of photogrammetry, photointerpretation, remote sensing and geographic information systems; or who by means of education or profession is interested in the application or development of these arts and sciences. Membership is for one year, with renewal based on the anniversary date of the month joined. Membership Dues include a 12-month electronic subscription to *PE&RS*. To receive a print copy of *PE&RS* there is an additional postage fee of \$60.00 USD for U.S. shipping; \$65.00 USD for Canadian shipping; or \$75.00 USD for international shipping per year. Annual Individual Member dues for members residing in the U.S. and Other Foreign Members are \$150.00 USD and \$158.00 USD for Canadians. Annual Student Member dues for members residing in the U.S. are \$50.00 USD; \$53.00 USD for Canadian; and \$60.00 USD for Other Foreign Members. A tax of 5% for Canada's Goods and Service Tax (GST #135123065) is applied to all members residing in Canada.

COPYRIGHT 2022. Copyright by the American Society for Photogrammetry and Remote Sensing. Reproduction of this issue or any part thereof (except short quotations for use in preparing technical and scientific papers) may be made only after obtaining the specific approval of the Managing Editor. The Society is not responsible for any statements made or opinions expressed in technical papers, advertisements, or other portions of this publication. Printed in the United States of America.

PERMISSION TO PHOTOCOPY. The copyright owner's consent that copies of the article may be made for personal or internal use or for the personal or internal use of specific clients. This consent is given on the condition, however, that the copier pay the stated per copy fee through the Copyright Clearance Center, Inc., 222 Rosewood Drive, Danvers, Massachusetts 01923, for copying beyond that permitted by Sections 107 or 108 of the U.S. Copyright Law. This consent does not extend to other kinds of copying, such as copying for general distribution, for advertising or promotional purposes, for creating new collective works, or for resale.

Be a part of ASPRS Social Media:

 facebook.com/ASPRS.org

 linkedin.com/groups/2745128/profile

 twitter.com/ASPRSorg

 youtube.com/user/ASPRS



AMERICAVIEW AND ITS LANDSAT CONNECTION

By Russell G. Congalton, Roberta Lenczowski, Lisa Wirth, and Christopher McGinty

What is AmericaView

AmericaView, a 501(c) (3) non-profit education and research organization, is a nationally organized, state-based consortium with more than 20 years of experience advancing the availability, timely distribution, education, and widespread use of remote sensing data and technology. AmericaView is divided into individual StateView members, with each hosted by a university in the corresponding state. Currently, there are 41 StateViews (see Figure 1) each led by a StateView Director who facilitates their state-based consortia. Combined, the StateViews consist of more than 300 local, state, and regional members with a directive of advancing the widespread use of remote sensing data and technology through education and outreach, workforce development, applied research, and technology transfer. Each StateView delivers remote sensing related educational, research, and operational products and services that meet the needs of the local, state, and regional communities that it serves. The success of AmericaView is a direct result of the power of collegiality and of the power of the AmericaView network.

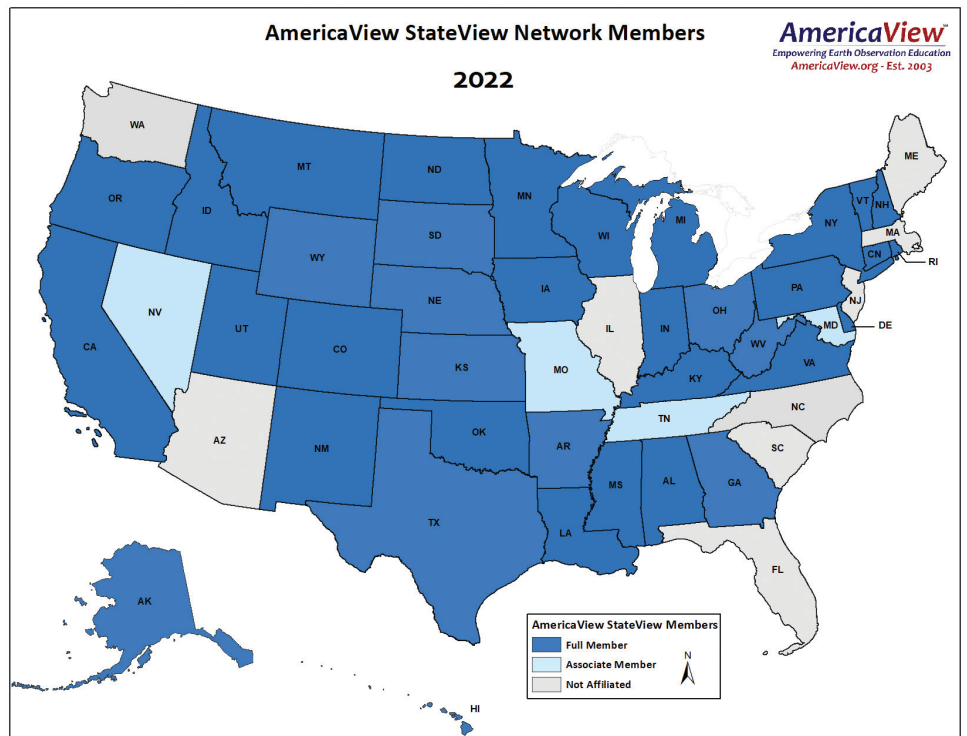


Figure 1. Distribution of StateViews as part of the AmericaView national consortium. Associate members are recent additions that are currently building their state consortium.

Photogrammetric Engineering & Remote Sensing
Vol. 88, No. 7, July 2022, pp. 421-424.
0099-1112/22/421-424

© 2022 American Society for Photogrammetry and Remote Sensing
doi: 10.14358/PERS.88.7.421

A Brief History

The concept of a national consortium to advance the adoption and use of remote sensing technologies and products at the state level was conceived in 1998 with the establishment of OhioView. One of the goals of OhioView was a partnership with the USGS Earth Resources Observation and Science (EROS) Data Center to ingest Landsat imagery and distribute it widely and effectively to the member institutions and to all the citizens of Ohio. Given the early success of OhioView, expansion to the national level was authorized by the United States Congress and achieved through the creation of AmericaView. Funding for AmericaView has since then been provided through the USGS National Land Imaging (NLI) Program National Land Remote Sensing Education Outreach and Research Activity (NLRSEORA). AmericaView was incorporated as a non-profit in 2003 beginning with 10 founding members (Arkansas, Georgia, Kansas, Mississippi, Ohio, South Dakota, Texas, West Virginia, Wyoming, and Nebraska).

From the outset of the consortium's incorporation, its pursuit of extending appreciation for and use of remote sensing has intentionally been inclusive of all. Provisioning access to and distribution of public domain Landsat imagery underpinned the earliest memorandum of understanding in 2002 between USGS and AmericaView. AmericaView, through its StateView members, has persistently sought and collaboratively nourished lasting education and research partnerships, networking their distributed academic perspectives. As a result of these activities, today an ever-expanding spectrum of users can properly apply remotely sensed imagery and its analysis to a wide variety of challenging issues. In an era focused on diversity, equity, and inclusion with belonging as an outcome, the last twenty years of AmericaView's active presence has bridged a time when only a privileged-few were using Landsat to a time when the "free and open" policy and effective academicians' training continue to overcome barriers to imagery access and use. All can belong to the community of contributors and benefactors.

Today, AmericaView is a locally facilitated and nationally coordinated consortium that has grown to 41 StateView members (see Figure 2). AmericaView StateView directors include

some of the foremost remote sensing scientists and educators in the nation, editors of major journals, authors of key remote sensing textbooks, and directors of major research laboratories. These remote sensing professionals impact the Earth science community in a wide variety of areas including, but not limited to, environmental monitoring; water quality, quantity, and utility studies; plant-phenology studies; natural resource management; traditional and precision agriculture; and disaster response and risk reduction. Collectively, the AmericaView directors are responsible for millions of dollars of competitive grants, lead quality research programs nationally and internationally, and have successfully disseminated their research outcomes through publications, presentations, and the Internet.

AmericaView powerfully facilitates the sharing of educational materials and research results through its national website, AmericaView.org, which shares remote sensing resources openly and freely to anyone who has interest. AmericaView's social media presence, including Twitter, LinkedIn, and YouTube, reach thousands of educators, students, decision makers and scientists across the nation and around the world. Metrics collected over the past decade indicate a broad interest base with hundreds of thousands of visits and revisits, from the merely curious to the sophisticated user. The volume of imagery and other geospatial data, training tutorials, StoryMaps, and articles that are viewed and/or downloaded through the website underscores the value of this information and the contribution AmericaView is making to the geospatial community and beyond.

AmericaView's national organization includes three committees: Education/Outreach, Strategic Planning, and Earth Sensors and Research. Each committee is chaired by a StateView member and composed of StateView consortium members. These committees align closely with key objectives of the USGS NLI NLRSEORA program. Through the committees, AmericaView has established working groups that have the ability to respond rapidly to specific topics of interest or organizational needs. For example, the Education/Outreach committee organized a STEAM (Science, Technology, Engineering, Arts, and Math) event reaching out to Baltimore County, MD middle schools to learn about remote sensing (Figure 3).



Figure 2. The AmericaView national consortium during the 2022 Annual Meeting in Fort Collins, Colorado (May 4, 2022)

The Landsat Connection

Members of AmericaView have been part of the Landsat community since the very beginning. To list a few examples, IndianaView Director Emeritus, Larry Biehl, along with Dr. David Landgrebe, from the Laboratory of Applications of Remote Sensing (LARS) at Purdue University, has been the driving force of the MultiSpec image processing software. Dr. James Merchant, KansasView Director Emeritus, of the Kansas Applications of Remote Sensing (KARS) lab was also an early Landsat researcher. South Dakota State University (home of SouthDakotaView) has had a synergistic relationship with the USGS EROS Center since the creation of this Landsat facility. Dr. Marvin Bauer, MinnesotaView Director Emeritus, was a research agronomist from 1970 – 1983 with LARS at Purdue University where he had key roles in the design, implementation, and data analysis of major agricultural remote sensing experiments with NASA and USDA. Dr. James Campbell, VirginiaView Director Emeritus, is the author of Introduction to Remote Sensing (Guilford Press), a leading remote sensing textbook. NewHampshireView Director Dr. Russell G. Congalton was a pioneer in assessing the accuracy of maps derived from Landsat imagery and continues this work to this day.

The connection between AmericaView and Landsat remains strong today as evidenced by the efforts made by StateView members in the areas of education, outreach, and applied research:

Education

StateView's have educated thousands of undergraduate students in the use of remote sensing and other geospatial technologies. In addition, hundreds of graduate students have conducted research projects using remote sensed imagery including Landsat that have been presented at conferences, published in scientific journals, and documented as theses and dissertations. Finally, tens of thousands of K-12 students have been introduced to Landsat and other remotely sensed imagery by hundreds of teachers trained by AmericaView members. Figure 4 shows the number of participants in activities over just the last 3 years ending in September of 2021. Most of these activities were accomplished while the Covid-19 pandemic was raging.

In addition, there are a large number of specific projects conducted by each state that clearly demonstrate AmericaView's impact on geospatial education. For example, Dr. Ramesh Sivanpillai, WyomingView Director, has worked with students and local ranchers using Landsat imagery on family lands, <https://bit.ly/WYViewLandsat>. MontanaView has worked with Native American students to use remotely sensed imagery to study the impacts of invasive grass species on tribal lands. Finally, the Education Committee has worked to identify places that remote sensing and other geospatial activities can be inserted into state earth science curriculum requirements which will ease the burden on teachers.

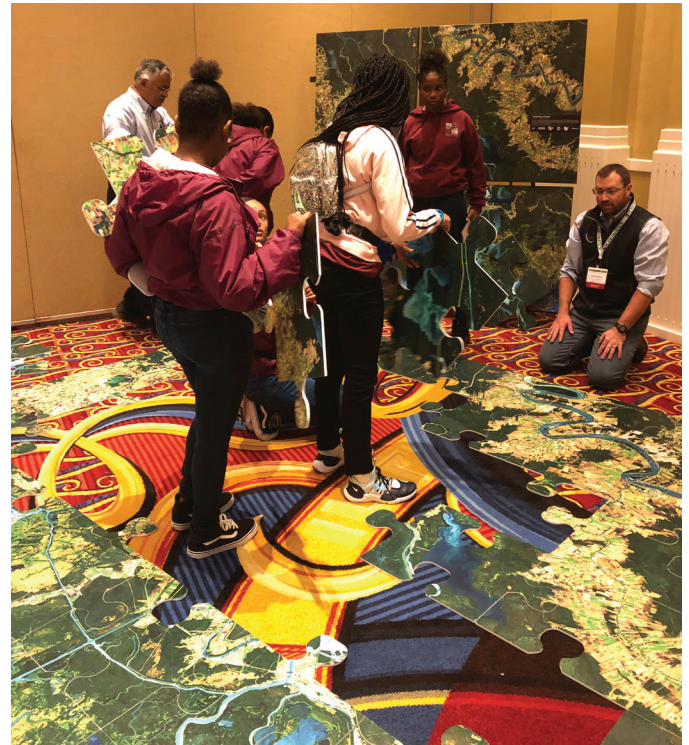


Figure 3. Middle school students from Baltimore County, MD working on a giant floor puzzle during a STEAM event held in Baltimore, MD. AmericaView Executive Director Chris McGinty can be seen kneeling over the puzzle to help while WyomingView Director Ramesh Sivanpillai helps in the background.

Total Individuals Educated in 2018-19, 2019-20, and 2020-21

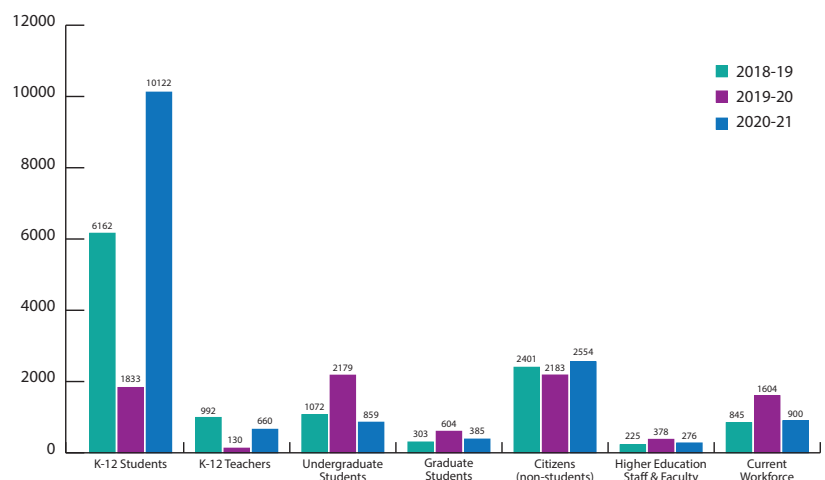


Figure 4. The numbers of individuals educated by various StateView activities over the last three year periods (October 2018-September 2019, October 2019-September 2020, October 2020-September 2021).

Outreach

Each year many AmericaView members participate in Earth Observation Day, an ongoing event as part of the American Geosciences Institute's Earth Science Week. Partnering with USGS and NASA, AmericaView members work to create a poster that demonstrates some themes related to earth observation from Landsat imagery. The back of the poster has a game that is designed to be fun while introducing learners of all ages to remote sensing.



Figure 5. An example of Earth as Art. Kevin Gallagher (near the center of the picture with the sports coat and one foot on the puzzle) USGS Core Science Systems Associate Director and other USGS and local participants assemble a floor puzzle, part of the AmericaView Earth as Art traveling exhibit.

Other outreach projects include a recent Google Earth Tour of the History of Landsat developed by UtahView State Coordinator, Ellie Leydsman McGinty. This history of Landsat was also presented as a GeoBytes Seminar through the American Society for Photogrammetry and Remote Sensing.

Developed by an increasing number of StateView's, a particularly effective outreach activity that has become increasingly popular with the public is Earth as Art. Figure 5 shows the Earth as Art exhibit that was presented at the Lompoc Library, California as part of the Landsat 9 launch events in September of 2021. In addition to the imagery shown on the easels is the large Earth as Art floor puzzle of Santa Barbara County.

Applied Research

AmericaView StateView's are very active in applied research that benefits their state or region. Some projects have been conducted jointly between universities within a state or sometimes in conjunction with other interested StateView's while others have been performed by a single university. One example of a StateView creating information that has become increasingly valuable and popular for local groups within the state of Georgia is a series of atlases generated from Landsat imagery that have various themes including forest change, croplands, and land cover <https://gaview.org/drupal893/>.

StateView applied research is extremely diverse based on the needs of that state. For example, OregonView has conducted research on shallow bathymetric mapping using Landsat 8 and ICESat-2 and the creation of the DEMs by fusing Landsat 8/Sentinel-2 and ICESat-2. ColoradoView has worked on missing pixel reconstruction using Landsat 8 ARD LST products. AmericaView's Program Director, Lisa Wirth, used Landsat 7 data to identify groundwater upwelling within an Interior Alaska glacially-fed river. These areas serve as prime spawning habitat for fall chum salmon, an important salmon species for subsistence. Recently, HawaiiView completed the first ever cloud-free mosaic of the state. Given cloud issues in Hawaii producing a cloud-free image is a major and extremely useful accomplishment.

Recently, the Earth Sensors and Research Committee coordinated an effort to produce a StoryMap showing the various



Figure 6. Looking to the future.

sensor capabilities and expertise of each StateView <https://bit.ly/AVSensors>. In addition, a second StoryMap was created to demonstrate research expertise of each StateView <https://bit.ly/AVResearch>. Together, these StoryMaps demonstrate the diversity of research being conducted within AmericaView while providing a plethora of information for those who want to know more about the uses of remotely sensed imagery.

Final Thoughts

As we celebrate the 50th anniversary of Landsat, it is worth looking back and seeing how far we have come. It is easy to be impressed by the overwhelming number of technological advances that have occurred since Landsat 1 was launched back in 1972. In many ways, computers were still in their infancy and our ability to process the amazing imagery acquired was extremely limited. There is no doubt that the AmericaView consortium has played a significant role in not only remotely sensed research, but perhaps even more importantly, in providing the imagery and the knowledge of how to use this imagery to an ever-expanding audience of school children, college students, professionals, local and state agencies, and the public.

As we look to the future (see Figure 6), more than ever we need remotely sensed imagery to aid in increasing awareness of the many environmental issues that are threatening the planet we call home. Our ability to map and monitor the Earth in real time with efficiency and accuracy has never been more important. AmericaView and the synergies created by the collegial consortium of StateViews will and must continue to bring remote sensing and other geospatial technologies, education, outreach, and research to everyone, especially the younger generations.

Russell G. Congalton is professor of remote sensing and GIS, University of New Hampshire and NewHampshireView Director; Roberta Lenczowski is secretary of the AmericaView Board of Directors and Deputy Chair of the Landsat Advisory Group; Lisa Wirth is the AmericaView Program Director; and Christopher McGinty is the AmericaView Executive Director.

Designing Color Style Sheets for your Mobile App — Easier Than You Think

Mobile apps are powerful communication tools, especially when it comes to sharing geographies of businesses, events, or other organizational needs. While most of us focus on setting up the back end of these apps, there are also front end design functions that need to be prioritized to keep your users' attention, such as the graphic user interface (GUI). Developing the GUI for mobile apps is a process that involves several moving parts, or in this case—several moving files. This can be a daunting task when trying to keep track of every linked design element and colors that match your app's brand. However, one easy way to save yourself time in applying your color scheme to your elements is to save them all to one style sheet, this month's "tip".

In Android Studio, an integrated development environment that is used to develop mobile apps for android and iOS devices, you can save your styling sheets and active codes to linked project folders. The style sheet files that are primarily used for this are the colors.xml and themes.xml files that are automatically created under your app's resources (res) folder.

1. In Android Studio, locate and open the colors.xml file in the project folder (app/res/values/colors.xml). In this template, there are a series of colors listed with HEX (hexadecimal) values and string values saved to each name variable, E.g.:

```
<tag variable = "string"> HEX value </tag>
```

```
<color name = "purple_200"> #FFBB86FC </color>.
```

The column to the left in Figure 1 previews each chosen color.

2. Click the Run button to generate an app preview in the emulator to see how the current color scheme appears (Figure 1).

3. Open the themes.xml file in the project folder (app/res/values/themes/themes.xml). Based on the template, default primary and secondary colors were applied for the app where each name variable is linked to the colors.xml file by calling @color and the string name of the variable (Figure 2), E.g.:

```
<item name = "colorPrimary"> @color/purple_500 </item>
in the themes.xml is directly linked to <color name =
"purple_500"> #FFBB86FC </color> in the colors.xml.
```

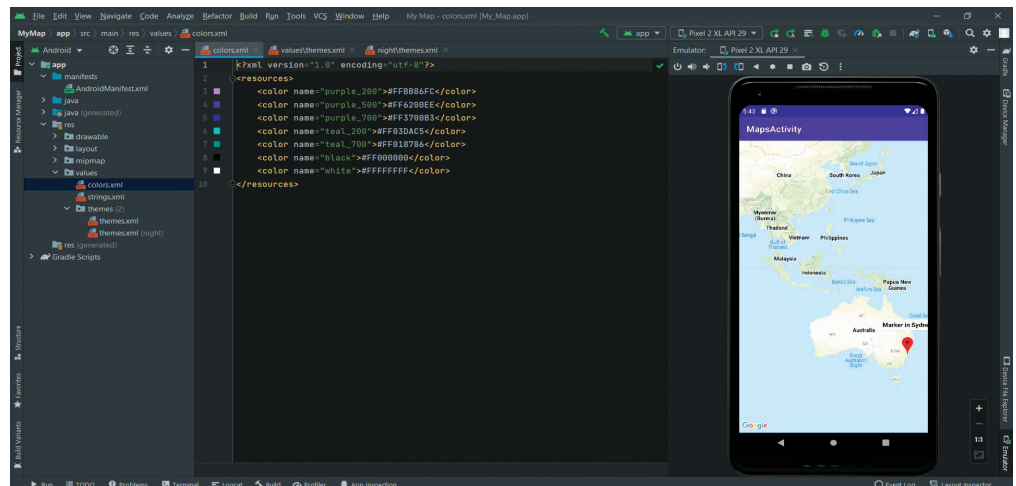


Figure 1: Default HEX values in colors.xml file and app preview.

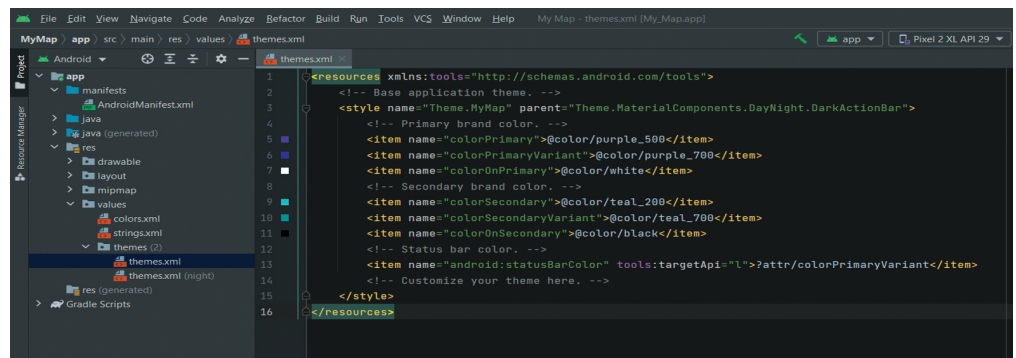


Figure 2: Set primary and secondary color schemes linked to themes.xml.

4. In the colors.xml file, replace the default HEX values with new values and replace the default string with another descriptor (Figure 3) E.g.:

```
<color name= "peach"> #D2506B </color>
```

5. In the themes.xml file, update the primary and secondary HEX values with the new reference colors (Figure 4), E.g.:

```
<item name = "colorPrimary"> @color/purple_500 </item> is now
<item name = "colorPrimary"> @color/peach </item>
```

6. Click the Run button to generate a new app preview in the emulator to see changes (Figure 5)

And voila!

Your updated style sheet can now be called upon for unique interface features or any additional theme you might create later on. If you encounter issues with calling colors from the style sheet, some quick ways to trouble shoot the issue can include:

- Check if you are updating the right xml file
- Make sure the string name you save the HEX value to is concise and easy to remember
- Check if you are calling the right variable (E.G. are you calling a secondary color from the themes.xml or a particular color from the colors.xml?)
- Run the emulator to refresh and see if your changes are applied to the right sections of the app

For more information on styling themes and color design management, visit the additional resources below.

Send your questions, comments, and tips to GISTT@ASPRS.org.

SOURCE

- Adobe Color [Web application]. (n.d.). Adobe. <https://color.adobe.com/create/color-wheel>.
- "Styles and Themes." (n.d.) Android Developers Documentation. Android. <https://developer.android.com/guide/topics/ui/look-and-feel/themes>.

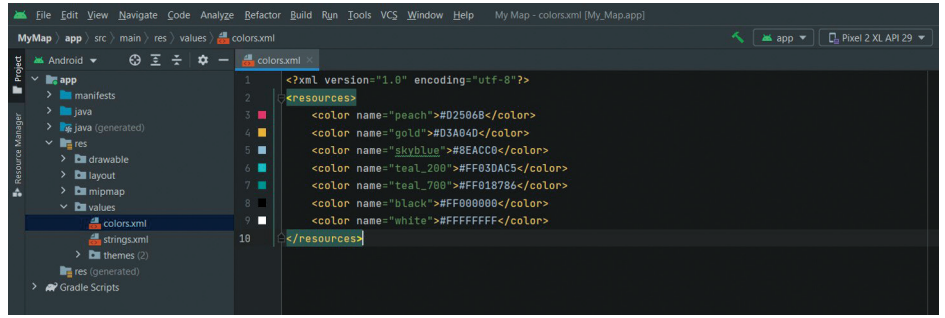


Figure 3: Colors.xml file with new HEX values.

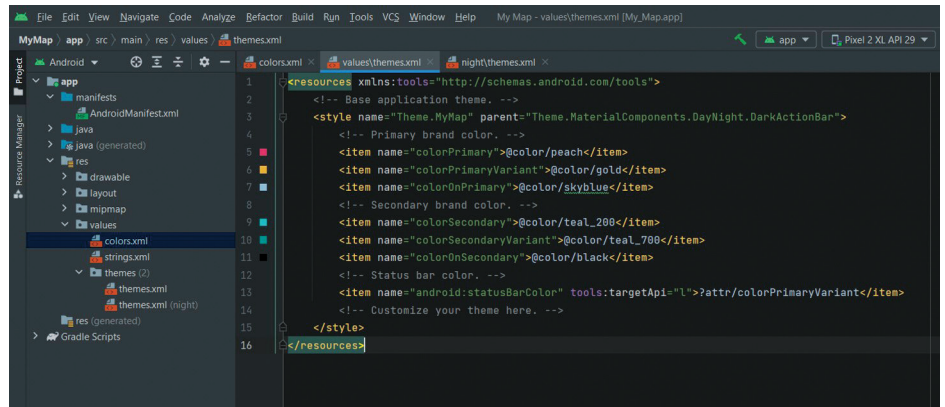


Figure 4: Primary and secondary color schemes linked to updated colors.xml file.

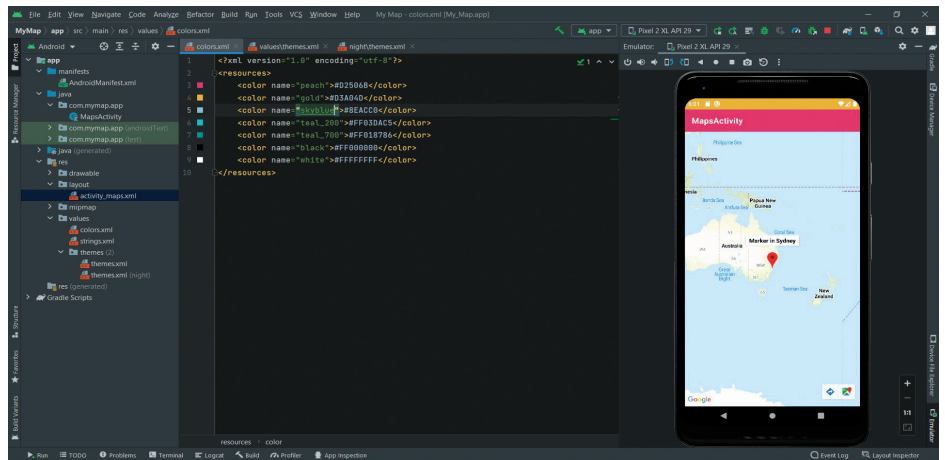


Figure 5: Updated app preview with new HEX values applied.

YoLani Martin is a Geospatial Analyst with Dewberry's Fairfax, VA office. She is a resource for open source tools and Python scripting. Al Karlin, Ph.D., CMS-L, GISP is with Dewberry's Geospatial and Technology Services group in Tampa, FL. As a senior geospatial scientist, Al works with all aspects of Lidar, remote sensing, photogrammetry, and GIS-related projects.



& GRIDS & DATUMS

BY Clifford J. Mugnier, CP, CMS, FASPRS

The Grids & Datums column has completed an exploration of every country on the Earth. For those who did not get to enjoy this world tour the first time, *PE&RS* is reprinting prior articles from the column. This month's article on the Republic of Zambia was originally printed in 2004 but contains updates to their coordinate system since then.

Evidence has been found north of Lusaka at Kabwe of human habitation that dates back 100,000 years. About 1000 AD, Swahili-Arab slave traders began intrusions into the area from the east. Between the 14th and 16th centuries, the Bantu-speaking Maravi migrated from the area presently know as Zaire, and established kingdoms in eastern and southeastern Zambia. The region came under the jurisdiction of the British South Africa Company in 1889, in 1911 it became Northern Rhodesia, and in 1924 it became a British Protectorate. From 1953 to 1963, it was part of the Federation of Rhodesia and Nyasaland (Malawi) and achieved independence as a republic, 58 years ago on 24 October 1964. Zambia is bordered by Angola (1,110 km) (*PE&RS*, March 2001), Democratic Republic of the Congo (1,930 km), Malawi (837 km), Moçambique (419 km) (*PE&RS*, September 1999), Namibia (233 km), Tanzania (338 km), and Zimbabwe (813 km) (*PE&RS*, November 2003). The climate is tropical, modified by the altitude of the mostly high plateau with some hills and mountains. The lowest point is the Zambezi River (329 m), and the highest point is in the Mafinga Hills (2,301 m).

Lake Tanganyika extends into a small portion of northern Zambia, and the Zambezi River (used as the origin of the country's name) forms the eastern border with Malawi. The famous Arc of the 30th Meridian follows the eastern shore of Lake Tanganyika and spans the Zambezi River. The Arc of the 30th Meridian is referenced to the Cape Datum of 1950 where the astronomic coordinates of the initial point of the Cape Datum near Port Elizabeth are for Buffelsfontein where $\Phi_0 = 33^{\circ} 59' 32.000''$ S and $\Lambda_0 = 25^{\circ} 30' 44.622''$ E. The ellipsoid of reference is the Clarke 1880, where $a = 6,378,249.145$ m and $1/f = 293.4663077$.

REPUBLIC OF ZAMBIA



The northwestern border of Zambia is common with the Democratic Republic of the Congo (Zaire), once known as the Belgian Congo. Zambia is adjacent to the Katanga province of the Congo, where a boundary commission published the results of a classical triangulation in 1954, *Comité Spécial du Katanga, Les Travaux Géodésiques du Service Géographique et Géologique*. The origin of the triangulation of Katanga (Le Point Fondamental) is the "A" end of the Tshinsenda baseline in Zambia where: $\Phi_0 = 12^{\circ} 20' 31.568''$ S and $\Lambda_0 = 28^{\circ} 01' 02.971''$ E. The altitude of the point was 1,331.31 m, as determined by trigonometric leveling from the 30th Arc triangulation performed in 1911. Subsequent double-run precise levels performed by then Major and later Brigadier Martin Hotine from Dar es Salaam in Tanzania necessitated a correction of +47 feet to the elevations in Zambia. Presumably, that correction was applied to the value published by the Belgians in 1954. The Tshinsenda Baseline was measured in 1912 with a length of 4,152.9912

continued on page 437

Photogrammetric Engineering & Remote Sensing
Vol. 88, No. 7, July 2022, pp. 427, 437.
0099-1112/22/427, 437

© 2022 American Society for Photogrammetry
and Remote Sensing
doi: 10.14358/PERS.88.7.427

ASPRS SAC: A YEAR IN REVIEW

This month we are delighted to highlight the role ASPRS SAC has played in strengthening the skills of our students through multiple virtual and in-person events. The following is a snapshot of each event and its impact.

ASPRS Webinar: Why Join ASPRS? September 15, 2021

A panel of ASPRS members from SAC, Early Career Professionals Council (ECPC), student chapters, and ASPRS Executive Director, Karen Schuckman discussed how ASPRS impacted their careers.

Impact: Students received an insight into the role of ASPRS in academia and beyond.

ASPRS Webinar: Scholarship Tips! October 4, 2021

Featured speakers, Dr. Lindi Quackenbush and Innocensia Owuor, answered prewritten questions on the ASPRS Awards and Scholarships Program.

Impact: Presenters answered questions and encouraged students to apply for scholarships.

SAC GIS Day Map Contest, November 18, 2021

ASPRS members were encouraged to create and submit a map to the contest. Submissions were judged by their peers and six winners were selected.

Impact: Participants got a chance to showcase their work. Additionally, the winners received a free one-year ArcGIS for Personal Use licenses from Esri and the opportunity to present their work at the ASPRS Annual Conference.

ASPRS Conference @ Geo Week February 5 - 7, 2022

Three of the SAC board members volunteered at the ASPRS Conference at Geo Week.

Impact: This was a great opportunity for SAC members to meet each other in person and to assist in the success of the conference.

ASPRS Virtual Conference Focus on Career Development: Spotlight on ASPRS Councils, March 22, 2022

The SAC provided a short presentation discussing its members, broad goals, and events as well as how to get involved. SAC

helped coordinate and plan the ASPRS Leadership Panel. SAC Communications Council Chair, Rabia Munsaf Khan, represented SAC on the panel.

Impact: This event yielded many interesting questions from the audience and provided valuable insight into why becoming an ASPRS member can and will enhance your personal and professional success.

ASPRS Pilot Mentorship Program, Ongoing

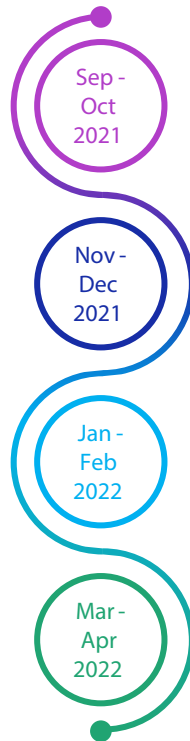
With six matched pairs, our mentor-mentee program is in full swing. Refer to our Signatures Column in the June 2022 issue of *PE&RS* for details about this program.

Impact: Both mentors and mentees are enjoying the program and calling it a two-way learning/conversation experience. This learning environment will help mentees gain personalized advice and shape their career path.

All in all, the goal of ASPRS SAC is to provide a support system for our ASPRS family.

If you are interested in participating in SAC activities:

- Join us every other Thursday from 10-11 am PST!
- Join us via this zoom link: <https://tinyurl.com/SACASPRSMeting>



Webinars

Why ASPRS?
ASPRS Scholarships Tips

Grants

GIS Map Contest
ASPRS In-person Conference

Networking

ASPRS Conference

Professional Development

SAC Panel Discussion
Mentor Mentee Program

ASPRS STUDENT ADVISORY COUNCIL

LAUREN MCKINNEY-WISE
COUNCIL CHAIR
OSCAR DURAN
DEPUTY COUNCIL CHAIR
CHUKWUMA JOHN OKOLIE
COMMUNICATIONS COUNCIL MEMBER

TBD
EDUCATION & PROFESSIONAL NETWORKING CHAIR
ALI ALRUZUQ
DEPUTY EDUCATION & PROFESSIONAL NETWORKING CHAIR
TESINI PRECIOUS DOMBO
COMMUNICATIONS COUNCIL MEMBER

RABIA MUNSAF KHAN
COMMUNICATIONS COUNCIL CHAIR
KENNETH EKPETERE
CHAPTERS COMMITTEE CHAIR
FREDA ELIKEM DORBU
COMMUNICATIONS COUNCIL MEMBER

SEEING OUR PLANET ANEW: FIFTY YEARS OF LANDSAT

Thomas R. Loveland, Martha C. Anderson, Justin L. Huntington, James R. Irons, David M. Johnson,
Laura E. P. Rocchio, Curtis E. Woodcock, and Michael A. Wulder

Introduction

The July 23, 1972 launch of the Earth Resources Technology Satellite (ERTS), later renamed Landsat 1, marks the first milestone of the Landsat journey. While the inception of the Landsat program began several years earlier (Goward et al. 2017), that first launch and the subsequent launches of eight more Landsat satellites define a timeline that leads us to celebrate the 50th anniversary of an ongoing satellite program with profound impacts on our observation and understanding of the Earth. Prior histories have addressed technical, programmatic, and scientific aspects of the Landsat program in a more-or-less chronological order (Mack 1990; Goward et al. 2017). Here, we briefly address the cumulative impacts of the Landsat program on key Earth science and environmental topics.

We attempt to address the “so what” questions. What do we know now about the Earth that we did not know 50 years ago due the Landsat data record? What are we able to do to protect, preserve, and wisely use our natural resources that we would not be able to do without Landsat data? The brevity of a feature article prevents comprehensive, exhaustive answers to these questions. Instead, we provide synopses of the impacts in four areas: land use and land cover change, agriculture, forestry and forest ecology, and water resources. Landsat data are employed for many other areas of research and application; we have chosen these four critical and representative topics to illustrate the value of the 50-year Landsat program.

Land Use and Land Cover Change

Land use and land cover characterize the land surface and how it is being managed, and maps of land cover and land use are foundational information for local to regional planning. One of the first uses of Landsat’s synoptic coverage was mapping land cover and land use, something that continues today and has improved through time. While projects that focus on local and regional land cover remain common, over time there has been steady progress toward maps that cover larger areas and multiple time periods. The first global land cover products were based on sensors with coarser spatial resolution: first at 1 km from AVHRR (Loveland et al. 2001) and then MODIS at

500 m (Friedl et al. 2002) and MERIS at 300 m (Arino et al. 2007). Following an extremely important change in data policy in 2008 enabling free and open access to the Landsat archive (Ryan and Freilich 2008; Woodcock et al. 2008), there has been an explosion in the scope of studies based on Landsat, including efforts that provided global land cover maps at 30 m (Chen et al. 2011; Gong et al. 2012; Zhu et al. 2019). Recently, an even finer spatial resolution (10 m) global map was released by ESA (Karra et al. 2021) based on Sentinel-2 and Sentinel-1 data.

While the role of Landsat in land cover and land use mapping has been important for decades, it is in the domain of land cover change that Landsat’s contribution is unique and its importance cannot be overstated. Landsat is the only program that has provided high quality satellite observations at spatial resolutions that capture human activity over many decades (Figure 1). Due to the wisdom and foresight

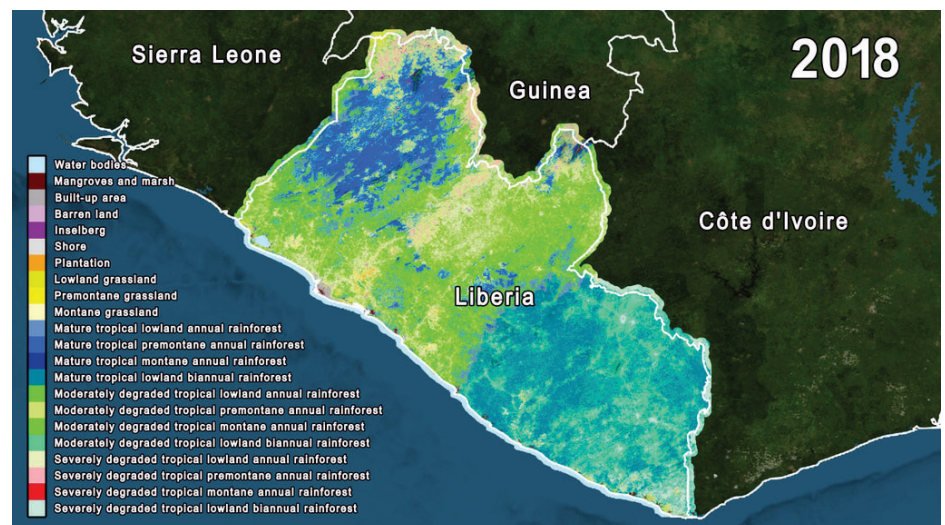


Figure 1. A NASA research team has made land cover maps of Liberia for every year in the last two decades using images from the joint NASA and United States Geological Survey’s Landsat mission. The team then refined the classifications using very high-resolution commercial satellite data and tree height information from the Global Ecosystem Dynamics Investigation (GED) lidar altimeter aboard the International Space Station. Source: NASA’s Science Visualization Studio; de Sousa et al. 2020.

Photogrammetric Engineering & Remote Sensing
Vol. 88, No. 7, July 2022, pp. 429-436.

0099-1112/22/429-436

© 2022 American Society for Photogrammetry
and Remote Sensing

doi: 10.14358/PERS.88.7.429

within the Landsat Program (Wulder et al. 2012), there is now a truly global archive populated with observations across seasons and years that contain a historical record of the Earth surface in the satellite era. As such, the data from Landsat continue to be mined to reveal how, when, and where land cover has been changing. And if maps of land cover are useful, maps of land cover change are dramatically more valuable as they document trends in surface conditions and the location and extent of human activities. At the U.S. national level, examples include the USGS National Land Cover Database (NLCD) (Wickham et al., 2020) and the USGS Land Change Monitoring, Assessment, and Projection (LCMAP) (Brown et al., 2020).

The availability of Landsat data has enabled mapping of the shifting extents of cities, forests, grasslands, savannas, agricultural fields, deserts, and glaciers, chronicling how each has changed over the past half century—a time period that has seen incredible modification of the surface of Earth as the world’s population has grown from 4 billion to almost 8 billion.

Agriculture

Agriculture constitutes the largest anthropogenic impact on the Earth’s terrestrial surface. Over one third of the global land surface is currently dedicated to growing food and fiber, or managing livestock. Of that, intensive cropping makes up about a third and the rest is comprised of pastures and rangelands used for forage and grazing (FAO 2022). The physical agricultural extent, and the practices within it, are rapidly evolving, growing, and shifting to meet the needs of the increasing global population (Godfray et al. 2010; UN 2019).

Ideally, society can transparently monitor and forecast the condition and productivity of agricultural areas in real time. Detailing the supply of commodities can allow for efficient allocation and ultimately improved food security (See et al. 2015). This is particularly important during times of widespread weather anomalies or civil unrest which often dramatically reduce the food supply in a region. Furthermore, given the large and dynamic footprint of agriculture, it is also important to track because of the profound influences on surrounding ecosystems and the sustainability of the broader environment globally (Ramanakutty et al. 2008).

Mapping and monitoring of short- and long-term trends in agriculture are difficult due to the wide geographies and ephemeral seasonalities. This was recognized over a half century ago and the initial design of Landsat was in many aspects

tailored to observing agriculture over broad regions down to the field-level several times a season. Upon the initial Landsat launches in the early 1970s, two large agriculture-specific research field campaigns, coined the Large Area Crop Inventory Experiment (LACIE) and the Agricultural and Resources Inventory Surveys Through Aerospace Remote Sensing (AgRISTARS) (MacDonald et al. 1975; Caudill and McArdle 1979), were established from the onset with goals of leveraging the Landsat imagery to objectively identify crop types and estimate harvest production. The success of these campaigns fostered decades worth of follow-on research and applications developments, both in the public and private sectors (MacDonald 1980; Doraiswamy et al. 2004; Gitelson et al. 2012; Gao et al. 2017; Thenkabail et al. 2017). Earth observation satellites with additional capabilities have been developed since, but the Landsat series has continued to remain a core data source for crop and rangelands monitoring systems (Figure 2).

Earth system science questions regarding the impact of agriculture on the environment have come to the forefront more recently (Crist et al. 2017; Vijay and Armsworth 2021). This is of major concern because of the continued expansion and pressuring of agriculture into surrounding ecosystems – many of which are vastly shrinking and threatened (Foley et al. 2005; Potapov et al. 2022). In particular, South America’s Amazon Basin has undergone remarkable change and is being heavily monitored (Gibbs et al. 2010; Song et al. 2021; Zalles et al. 2021). Intensification of croplands has also increased, creating pressures on the ability for food production systems to maintain sustainability (Tilman et al. 2011; Zabel et al. 2019). Finally, climate changes are impacting, and being impacted by, agriculture through the feedbacks within the system complex (Wolf et al. 2015).

The 50-year Landsat archive has provided unparalleled and objective documentation of these changes across agricultural landscapes around the globe over a time when the population

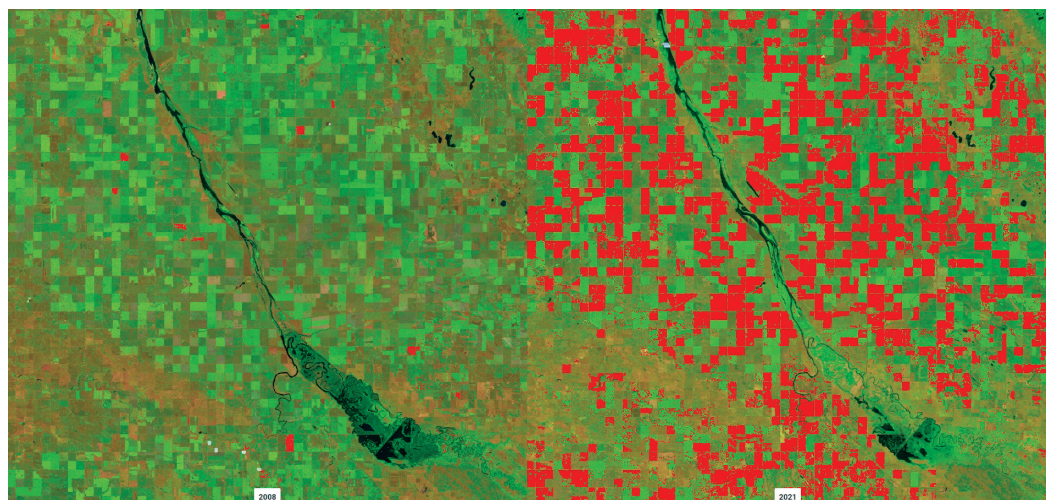


Figure 2. Landsat data help the USDA document the dramatic increase of soybean plantings north-east of Minot, North Dakota occurring in recent years. The left image is from Landsat 5 mid-summer 2008 and the right from Landsat 8 mid-summer 2021. Areas in red were identified from the imagery as soybean fields.

has doubled. Landsat will continue to be an imperative tool for monitoring agriculture and understanding the interactions with Earth's natural resources into the next half century.

Forestry and Forest Ecology

Access to Landsat data has had a profound impact upon forestry and forest ecology, using scientific underpinnings to improve forest management and the understanding of forest ecosystems and how they function. Early investigations using Landsat typically focused upon single images to provide land cover information on the location of forests. Demonstrated soon after was the ability to difference images to capture forest change (Nelson 1983; Goward et al. 2017) ultimately enabling categorization of change type, such as wildfire, harvesting, or land use conversion (Cohen et al. 2010). The ability to detect change in forest ecosystems is highly valued from both economic and ecological points of view (Kennedy et al. 2014). Forest management is informed by up-to-date knowledge of where and when harvesting has occurred, as well as the subsequent regeneration of trees (White et al. 2022). Landsat has enabled detailed mapping of global forest dynamics (Masek et al. 2008; Hansen et al. 2013), exposing illegally cleared forests along the way (Kuemmerle et al. 2009). Landsat has been used to identify locations reported as protected parks, that in reality, are suffering from human-induced degradation (Liu et al. 2001).

Forest removals impact how land functions in relation to both the terrestrial ecosystem and the atmosphere. Forest biomass has a known relationship to carbon (Houghton et al. 2009). Through a knowledge of photosynthesis, scientists can determine the nature of exchange of atmospheric carbon with conversion to long-term storage in trees (Goward and Williams 1997). Losses of long-term tree-based carbon storage can be calculated using Landsat-derived maps of forest change, and further refined when combined with lidar measurements (Goward and Williams 1997; Coops et al. 2021; Harris et al. 2021). The long Landsat data record enables cause of forest loss to be determined, and long-term carbon stock implications realized (Wulder et al. 2020).

The 50-year history of Landsat's borderless observations provides a reliable global baseline as well as the capacity to derive trends using time-series approaches. Using Landsat, national (Figure 3) and international agencies can define measurements and monitoring criteria to underpin agreements with robust and actionable information (Wulder et al. 2022-In review). The for-

ward-going commitment to data continuity, as demonstrated by Landsat 9 and forthcoming Landsat Next (Masek et al. 2020), provides the required assurance to build programs around Landsat. Landsat time series data show the rate, magnitude, and persistence of forest change (Kennedy et al. 2010) and provide ecological insights into the causes and effects of these changes (Cohen et al. 2016). Both within- and between-year Landsat time-series analyses enable the capture of vegetation phenology (Bolton et al. 2020), exposing impacts of climate change. The understanding that humanity has of Earth's forested ecosystems status and function has been unreservedly enriched by Landsat observations.

Water Management and Hydrology

Evapotranspiration (ET) is a key component of the hydrologic cycle, representing the amount of water consumed by crops and natural vegetation in the process of growth. The ability to accurately quantify ET over landscapes is critical for planning toward a sustainable water supply supporting agriculture, urban use, and natural ecosystem services. Deficits in ET relative to long-term norms may signal incipient vegetative stress due to soil moisture depletion, disease, or disturbance (Yang et al. 2020; Yang et al. 2021a; Yang et al. 2021b).

Landsat has provided a unique opportunity to measure ET at the scale of human influence in the water cycle (Anderson et al. 2012). The thermal infrared bands, available since Landsat 4, enable retrieval of ET through energy balance modeling, which considers impacts of evaporative cooling on the land-surface temperature. Landsat surface reflectance bands additionally allow quantification of albedo, landcover type,

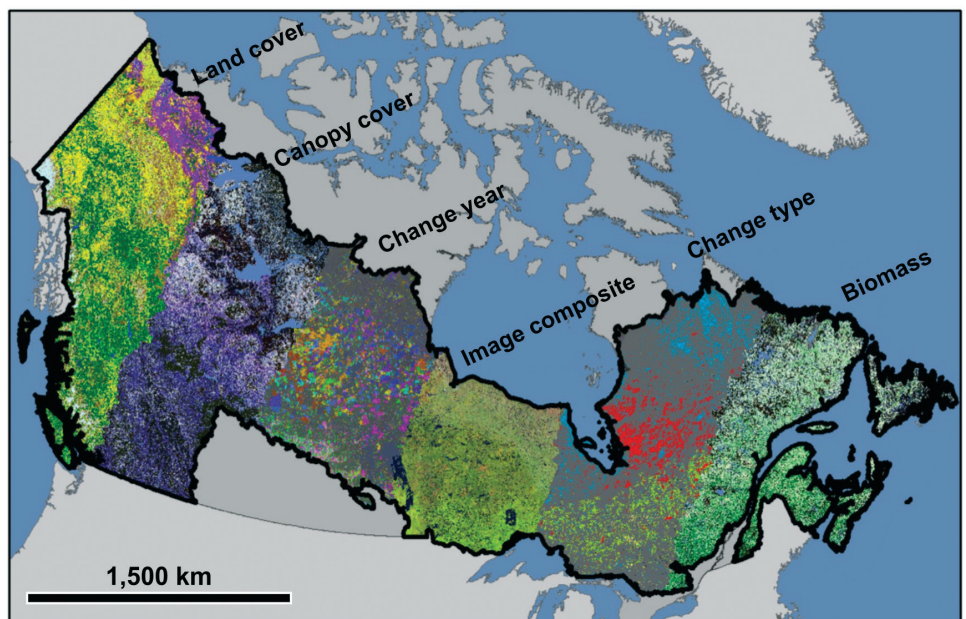


Figure 3. Landsat data underpins national and international forest monitoring and reporting programs. Both status and change in important forest attributes can be mapped and monitored, including land cover, change location, type, and timing, as well as forest structural attributes such as biomass and canopy cover. These attributes can be relayed as maps or as temporal trends to inform forest management or ecological studies, such as detailed information on rates of change by disturbance type by jurisdiction or ecologically meaningful unit (Hermosilla et al. 2016).

and fractional vegetation cover—also important in governing water and energy partitioning. Unlike moderate resolution sensors like AVHRR, MODIS, and VIIRS, the 30-120-m resolution of Landsat allows discrimination of water use by individual fields and crop types, and therefore Landsat has become increasingly used for decision-making and water use accounting at field to basin scales.

The need for accurate water-use information at the critical Landsat scale continues to grow with increasing population, agricultural needs, drought, and atmospheric thirst for water in the U.S. and globally (Quinteiro et al. 2018; Hoffmann et al. 2021; Albano et al. 2022; Schumacher et al. 2022). For example, water rights compliance assessment in some western states has evolved from costly and inaccurate methods involving site visits or analyses of pumping electricity bills to quantitative assessment via Landsat ET map timeseries (Kramber et al. 2010). The ability to quantify seasonal water use by land-use or crop-type enables development of long-term groundwater and water demand plans accommodating projected changes in land-use (Morse et al. 2003; Anderson et al. 2018). Landsat-based irrigation withdrawals are planned to be used for the U.S. National Water Census and next generation national hydrology modeling initiatives as part of the SECURE Water Act (Evenson et al. 2018; Marston et al., 2022). The Landsat archive has also greatly advanced our ability to monitor and understand how groundwater-dependent ecosystems, which serve as critical climate refugia for many sensitive species (Cartwright et al. 2020), are responding to changes in climate and water and rangeland management (Huntington et al. 2016; Fesenmyer et al. 2018; Meyers et al. 2021). Having the unmatched combination of a 50-year history, continuity, and optimal spatial scale – Landsat 9 and Landsat Next will allow for the kind of next generation research and applications required to help address the growing water challenges in the coming decades.

With the advancements in Landsat ET retrieval made over the past decades, there remains the challenge of operationally generating information over large areas and getting these satellite-based water use data into the hands of decision makers to help inform water resource management. With the advent of cloud computing (Huntington et al. 2017) and distribution of higher-level Landsat land-surface temperature and surface reflectance products, routine wall-to-wall mapping and delivery of robust ET information is becoming a

reality. Under the OpenET project, for example, an ensemble of ET modeling systems runs in near-real-time, supplying daily to seasonal 30-m resolution ET data over the western United States (Figure 4), with plans for expansion to full CONUS and global coverage (Melton et al. 2021). Free and open access to a shared set of trusted Landsat ET data can provide a critical baseline in consensus planning for sustainable water futures.

Landsat’s long archive has also been harnessed to create global maps at 30 m resolution tracing how the location and persistence of surface water bodies have shifted over the past four decades. These maps give us a salient perspective on the scope of climate change and human activities on fresh water supplies, while providing valuable information for water and ecosystem managers (Pekel et al. 2016). Landsat measurements have also been used together with data from Aqua, Terra, and ESA’s Copernicus Sentinel-2 and -3 satellites to detect harmful algal blooms that can have profound impacts on human health and safety. Knowledge gleaned from these studies has informed sensor specifications for Landsat Next which will expand this capability (Pahlevan et al. 2019).

Conclusion

The discussion above touches on several common themes across the four key areas of study. Fifty years ago, the analyses and applications of Landsat data began with the use of single scenes to provide maps and information across large, circa 180 km square regions at the scale of human impact. Each scene provided a snapshot of time. At that time and until the mid-1980’s, the Landsat satellites provided the only source of such data from space. As the acquisition of Landsat data began to repeat, pairwise comparisons of scenes collected

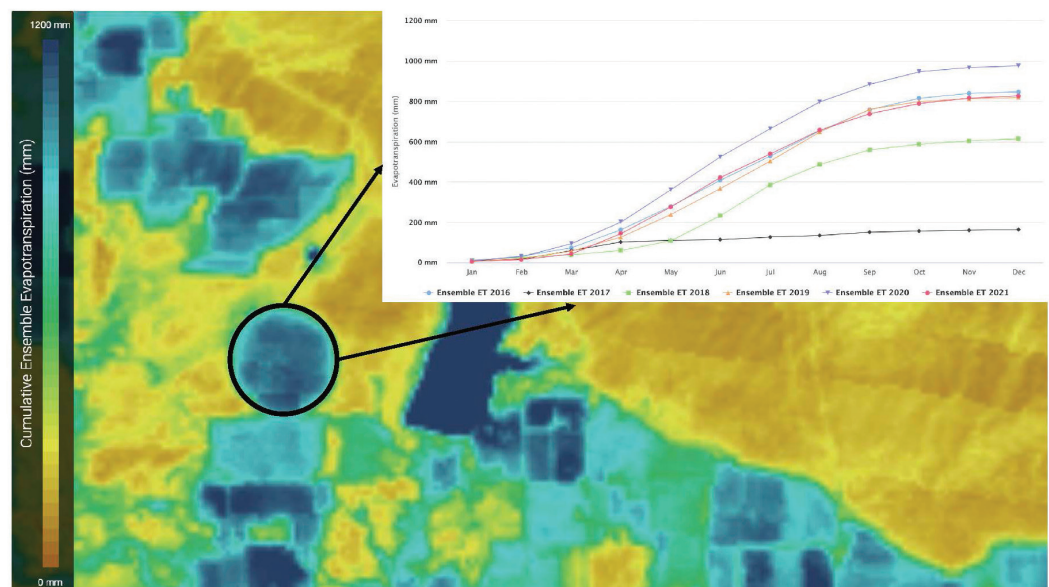


Figure 4. Spatial distribution of ensemble-average annual ET for 2021 from OpenET for an agricultural area near Grand Valley, Colorado, within the Upper Colorado River Basin (UCRB), as well as cumulative monthly ET time series for 2016 through 2021 for a selected field. The highlighted field participated in a water conservation study in 2017 and 2018 with full and partial irrigation forbearance, respectively. Cumulative time series of ET for each year clearly show the ET response due to reduced irrigation and can serve as the basis for estimating conserved consumptive water use for potential water conservation programs within the UCRB and other areas in the Western U.S.

over the same area were performed to observe change between two points of time. As more time passed, technical capabilities evolved to allow mosaics of Landsat scenes covering increasing areas to the continental and global extent. In parallel, the repeated capture of Landsat data with increasing frequency of global coverage facilitated the development of time series analyses both within years and across years. These advancements towards the use of large volumes of Landsat data over space and time were made possible by the evolution of computing technologies, by careful attention to sensor calibration, and, perhaps most importantly, by the 2008 decision by the USGS to distribute Landsat data at no cost to requestors. After 2008, researchers and resource managers could use all the Landsat data they needed, and not just the data they could afford. Further, as other satellite systems were launched, Landsat data are increasingly used in conjunction with data from other national government, international, and commercial sources of data. These common themes apply to many other realms of Landsat data analyses and applications such as glaciology and cryospheric science, the changing state of coral reefs, the annual snowpack, urban development, and a host of other Earth science and application topics.

What do we know about the Earth that we did not know fifty years ago thanks to Landsat? We know where and when land cover and land use are changing. We know which crops are being grown where on an annual basis and that knowledge supports commodity investments and food security. We know the extent of global forest disturbance and the impact on ecosystems. We know where and how much water is used for irrigation to increase food production with improved management of that invaluable resource. The continuous improvement of the Landsat data stream, from single-scene observations through to analysis ready data products (Dwyer et al. 2018) for time series analyses, has enabled continuing advancements in application development and science investigations. We look forward to a future with further advancements in Earth observations buttressed by the continuing progress of the Landsat program.

References

- Albano, C. M., J. T. Abatzoglou, D. J. McEvoy, J. L. Huntington, C. G. Morton, M. D. Dettinger, and T. J. Ott. 2022. A Multidataset Assessment of Climatic Drivers and Uncertainties of Recent Trends in Evaporative Demand across the Continental United States. *Journal of Hydrometeorology* 23(4): 505-519.
- Anderson, M. C., R. G. Allen, A. Morse, and W. P. Kustas. 2012. Use of Landsat thermal imagery in monitoring evapotranspiration and managing water resources. *Remote Sensing of Environment* 122: 50-65.
- Anderson, M. C., F. Gao, K. Knipper, C. Hain, W. Dulaney, D. D. Baldocchi, E. Eichelmann, K. S. Hemes, Y. Yang, J. Medellín-Azuara, and W. P. Kustas. 2018. Field-scale assessment of land and water use change over the California Delta using remote sensing. *Remote Sensing* 10(6): 889.
- Arino, O., D. Gross, F. Ranera, M. Leroy, P. Bicheron, C. Brockman, P. Defourny, C. Vancutsem, F. Achard, L. Durieux, L. Bourg, J. Latham, A. Di Gregorio, R. Witt, M. Herold, J. Sambale, S. Plummer, and J. L. Weber. 2007. GlobCover: ESA service for global land cover from MERIS. *IEEE International Geoscience and Remote Sensing Symposium*, 23-28 July 2007 pp. 2412-2415.
- Bolton, D. K., J. M. Gray, E. K. Melaas, M. Moon, L. Eklundh, M. A. Friedl. 2020. Continental-scale land surface phenology from harmonized Landsat 8 and Sentinel-2 imagery. *Remote Sensing of Environment* 240:111685.
- Brown, J. F., H. J. Tollerud, C. P. Barber, Q. Zhou, J. L. Dwyer, J. E. Vogelmann, T. R. Loveland, C. E. Woodcock, S. V. Stehman, Z. Zhu, B. W. Pengra, K. Smith, J. A. Horton, G. Xian, R. F. Auch, T. L. Sohl, K. L. Sayler, A. L. Gallant, D. Zelenak, R. R. Reker, and J. Rover. 2020. Lessons learned implementing an operational continuous United States national land change monitoring capability: The Land Change Monitoring, Assessment, and Projection (LCMAP) approach. *Remote Sensing of Environment* 238:111356.
- Cartwright, J. M., K. A. Dwire, Z. Freed, S. J. Hammer, B. McLaughlin, L. W. Misztal, E. R. Schenk, J. R. Spence, A. E. Springer, and L. E. Stevens. 2020. Oases of the future? Springs as potential hydrologic refugia in drying climates. *Frontiers in Ecology and the Environment* 18(5): 245-253.
- Caudill, C. E. and R.C. McArdle. 1979. Research evaluation considerations for AgRISTARS. Washington, D.C., U.S. Department of Agriculture, Economics, Statistics, and Cooperatives Service.
- Chen, J., X. Zhu, J. E. Vogelmann, F. Gao, and S. Jin. 2011. A simple and effective method for filling gaps in Landsat ETM+ SLC-off images. *Remote Sensing of Environment* 115 (4):1053-1064.
- Cohen, W. B., Z. Yang, R. Kennedy. 2010. Detecting trends in forest disturbance and recovery using yearly Landsat time series: 2. TimeSync — Tools for calibration and validation. *Remote Sensing of Environment* 114(12): 2911-2924.
- Cohen, W. B., Z. Yang, S. V. Stehman, T. A. Schroeder, D. M. Bell, J. G. Masek, C. Huang, G. W. Meigs. 2016. Forest disturbance across the conterminous United States from 1985-2012: The emerging dominance of forest decline. *Forest Ecology Management* 360: 242-252.
- Coops, N. C., P. Tompalski, T.R.H. Goodbody, M. Queinnec, J. E. Luther, D. K. Bolton, J. C. White, M. A. Wulder, O. R. van Lier, T. Hermosilla. 2021. Modelling lidar-derived estimates of forest attributes over space and time: A review of approaches and future trends. *Remote Sensing of Environment* 260, 112477.
- Crist, E., C. Mora, R. Engelman. 2017. The interaction of human population, food production, and biodiversity protection. *Science* 356 (6335): 260-264.
- de Sousa, C., L. Fatoyinbo, C. Neigh, F. Boucka, V. Angoue, T. Larsen. 2020. Cloud-computing and machine learning in support of country-level land cover and ecosystem extent mapping in Liberia and Gabon. *PLOS ONE* 15 (1): e0227438.
- Doraiswamy, P. C., J. L. Hatfield, T. J. Jackson, B. Akhmedov, J. Prueger, A. Stern. 2004. Crop condition and yield simulations using Landsat and MODIS. *Remote Sensing of Environment* 92 (4): 548-559.

- Dwyer, J. L., D. P. Roy, B. Sauer, C. B. Jenkerson, H. K. Zhang, L. Lyburner. 2018. Analysis ready data: Enabling analysis of the landsat archive. *Remote Sensing* 10 (9):1363.
- Evenson, E. J., S. A. Jones, N. L. Barber, P. J. Barlow, D. L. Blodgett, B. W. Bruce, K. Douglas-Mankin, W. H. Farmer, J. M. Fischer, W. B. Hughes, J. G. Kennen, J. E. Kiang, M. A. Maupin, H. W. Reeves, G. Senay, J. S. Stanton, C. R. Wagner, J. T. Wilson. 2018. Continuing progress toward a national assessment of water availability and use. *U.S. Geological Survey Circular 1440*. Reston, Va.
- Fairfax, E., and A. Whittle. 2020. Smokey the Beaver: beaver-dammed riparian corridors stay green during wildfire throughout the western United States. *Ecological Applications* 30(8): e02225.
- Fesenmyer, K. A., D. C. Dauwalter, C. Evans, T. Allai. 2018. Livestock management, beaver, and climate influences on riparian vegetation in a semiarid landscape. *PloS one* 13 (12):e0208928.
- Foley, J. A., R. DeFries, G. P. Asner, C. Barford, G. Bonan, S. R. Carpenter, F. S. Chapin, M. T. Coe, G. C. Daily, H. K. Gibbs, J. H. Helkowski, T. Holloway, E. A. Howard, C. J. Kucharik, C. Monfreda, J. A. Patz, I. C. Prentice, N. Ramankutty, P. K. Snyder. 2005. Global consequences of land use. *Science* 309 (5734): 570-574.
- Food and Agriculture Organization. 2020. FAOSTAT Land Use Domain. <<http://www.fao.org/faostat/en/#data/RL>> Accessed 30 May 2022.
- Gao, F., M. C. Anderson, X. Zhang, Z. Yang, J. G. Alfieri, W. P. Kustas, R. Mueller, D. M. Johnson, J. H. Prueger. 2017. Toward mapping crop progress at field scales through fusion of Landsat and MODIS imagery. *Remote Sensing of Environment* 188: 9–25.
- Gibbs, H. K., A. S. Ruesch, F. Achard, M. K. Clayton, P. Holmgren, N. Ramankutty, and J. A. Foley. 2010. Tropical forests were the primary sources of new agricultural land in the 1980s and 1990s. *Proceedings of the National Academy of Sciences* 107 (38):16732-16737.
- Gitelson, A.A., Y. Peng, J. G. Masek, D. C. Rundquist, S. Verma, A. Suyker, J. M. Baker, J. T. Hatfield, T. Meyers. 2012. Remote estimation of crop gross primary production with Landsat data. *Remote Sensing of Environment* 121: 404–414.
- Godfray, H.C.J., J. R. Beddington, I. R. Crute, L. Haddad, D. Lawrence, J. F. Muir, J. Pretty, S. Robinson, S. M. Thomas, C. Toulmin. 2010. Food Security: The Challenge of Feeding 9 Billion People. *Science* 327 (5967):812-818.
- Gong, P., J. Wang, L. Yu, Y. Zhao, Y. Zhao, L. Liang, Z. Niu, X. Huang, H. Fu, S. Liu, C. Li, X. Li, W. Fu, C. Liu, Y. Xu, X. Wang, Q. Cheng, L. Hu, W. Yao, H. Zhang, P. Zhu, Z. Zhao, H. Zhang, Y. Zheng, L. Ji, Y. Zhang, H. Chen, A. Yan, J. Guo, L. Yu, L. Wang, X. Liu, T. Shi, M. Zhu, Y. Chen, G. Yang, P. Tang, B. Xu, C. Giri, N. Clinton, Z. Zhu, J. Chen, and J. Chen. 2013. Finer resolution observation and monitoring of global land cover: first mapping results with Landsat TM and ETM+ data. *International Journal of Remote Sensing* 34 (7): 2607-2654.
- Goward, S. and D. Williams. 1997. Landsat and Earth systems science: development of terrestrial monitoring. *Photogrammetric Engineering and Remote Sensing* 63(7): 887–900.
- Goward, S. N., D. L. Williams, T. Arvidson, L.E.P. Rocchio, J. R. Irons, C. A. Russell. S. S. Johnston. 2017. *Landsat's Enduring Legacy: Pioneering Global Land Observations from Space*. Bethesda, Md.: American Society for Photogrammetry and Remote Sensing.
- Hansen, M. C., P. V. Potapov, R. Moore, M. Hancher, S. A. Turubanova, A. Tyukavina, D. Thau, S. V. Stehman, S. J. Goetz, T. R. Loveland, A. Kommareddy, A. Egorov, L. Chini, C. O. Justice, and J. R. G. Townshend. 2013. High-Resolution Global Maps of 21st-Century Forest Cover Change. *Science* 342 (6160): 850-853.
- Harris, N. L., D. A. Gibbs, A. Baccini, R. A. Birdsey, S. de Bruin, M. Farina, L. Fatoyinbo, M. C. Hansen, M. Herold, R. A. Houghton, P. V. Potapov, D. R. Suarez, R. M. Roman-Cuesta, S. S. Saatchi, C. M. Slay, S. A. Turubanova, A. Tyukavina. 2021. Global maps of twenty-first century forest carbon fluxes. *Nature Climate Change* 11 (3): 234-240.
- Hermosilla, T., Wulder, M.A., White, J.C., Coops, N.C., Hobart, G.W., Campbell, L.B., 2016. Mass data processing of time series Landsat imagery: pixels to data products for forest monitoring. *International Journal of Digital Earth* 9, 1035–1054. <https://doi.org/10.1080/17538947.2016.1187673>.
- Hoffmann, D., A.J.E. Gallant, M. Hobbins. 2021. Flash Drought in CMIP5 Models. *Journal of Hydrometeorology* 22 (6): 1439-1454.
- Houghton, R. A., F. Hall, S. J. Goetz. 2009. Importance of biomass in the global carbon cycle. *Journal of Geophysical Research Biogeosciences* 114(G2): 1–13.
- Huntington, J. L., K. C. Hegewisch, B. Daudert, C. G. Morton, J. T. Abatzoglou, D. J. McEvoy, T. Erickson, T. 2017. Climate engine: Cloud computing and visualization of climate and remote sensing data for advanced natural resource monitoring and process understanding. *Bulletin of the American Meteorological Society* 98: 2397-2409
- Huntington, J., K. McGwire, C. Morton, K. Snyder, S. Peterson, T. Erickson, R. Niswonger, R. Carroll, G. Smith, R.A. Allen. 2016. Assessing the role of climate and resource management on groundwater dependent ecosystem changes in arid environments with the Landsat archive. *Remote Sensing of Environment* 185: 186-197.
- Karra, K., C. Kontgis, Z. Statman-Weil, J. C. Mazzariello, M. Mathis, and S. P. Brumby. 2021. Global land use / land cover with Sentinel 2 and deep learning. 2021 *IEEE International Geoscience and Remote Sensing Symposium IGARSS*, 11-16 July 2021.
- Kennedy, R.E., S. Andréfouët, W. B. Cohen, C. Gómez, P. Griffiths, M. Hais, S.P. Healey, E.H. Helmer, P. Hostert, M. B. Lyons, G.W Meigs, D. Pflugmacher, S.R. Phinn, S. L. Powell, P. Scarth, S. Sen, T. A. Schroeder, A. Schneider, R. Sonnenschein, J. E. Vogelmann, M. A. Wulder, Z. Zhu. 2014. Bringing an ecological view of change to landsat-based remote sensing. *Frontiers in Ecology and the Environment* 12 (6): 339-346.
- Kennedy, R. E., Z. Yang, W. B. Cohen. 2010. Detecting trends in forest disturbance and recovery using yearly Landsat time series: 1. LandTrendr — Temporal segmentation algorithms.

- Remote Sensing of Environment* 114 (12): 2897-2910.
- Kramber, W. J., A. Morse, R. Allen. 2010. Mapping evapotranspiration: A remote sensing innovation. *Photogrammetric Engineering and Remote Sensing* 76:6-10.
- Kuemmerle, T., O. Chaskovskyy, J. Knorn, V. C. Radeloff, I. Krulov, W. S. Keeton, P. Hostert. 2009. Forest cover change and illegal logging in the Ukrainian Carpathians in the transition period from 1988 to 2007. *Remote Sensing of Environment* 113 (6): 1194-1207.
- Liu, J., M. Linderman, Z. Ouyang, L. An, J. Yang, H. Zhang. 2001. Ecological degradation in protected areas: The case of Wolong nature reserve for giant pandas. *Science* 292 (5514): 98-101.
- MacDonald, R. B., F. G. Hall, R. B. Erb. 1975. The use of Landsat data in a Large Area Crop Inventory Experiment (LACIE). *LARS Symposia*, paper 46. <http://docs.lib.purdue.edu/lars_symp/46> Accessed 30 May 2022.
- MacDonald, R.B. and F.G. Hall. 1980. Global crop forecasting. *Science* 208 (4445): 670-679.
- Marston, L.T., A.M. Abdallah, K.J. Bagstad, K. Dickson, P. Glynn, S.G. Larsen, F.S. Melton, K. Onda, J.A. Painter, J. Prairie, B.L. Ruddell, R.R. Rushforth, G.B. Senay, and K. Shaffer. 2022. Water-use data in the United States: Challenges and future directions. *Journal of the American Water Resources Association* JAWR-21-0080-C.
- Masek, Jeffrey G., C. Huang, R. Wolfe, W. Cohen, F. Hall, J. Kutler, and P. Nelson. 2008. North American forest disturbance mapped from a decadal Landsat record. *Remote Sensing of Environment* 112 (6): 2914-2926.
- Masek, J. G., M. A. Wulder, B. Markham, J. McCorkel, C. J. Crawford, J. Storey, D. T. Jenstrom. 2020. Landsat 9: Empowering open science and applications through continuity. *Remote Sensing of Environment* 248: 111968.
- Melton, F.S., J. Huntington, R. Grimm, J. Herring, M. Hall, D. Rollison, T. Erickson, R. Allen, M. Anderson, J. B. Fisher, A. Kilic, G. B. Senay, J. Volk, C. Hain, L. Johnson, A. Ruhoff, P. Blankenau, M. Bromley, W. Carrara, B. Daudert, C. Doherty, C. Dunkerly, M. Friedrichs, A. Guzman, G. Halverson, J. Hansen, J. Harding, Y. Kang, D. Ketchum, B. Minor, C. Morton, S. Ortega-Salazar, T. Ott, M. Ozdogan, P. M. ReVelle, M. Schull, C. Wang, Y. Yang, R. G. Anderson. 2021. OpenET: Filling a critical data gap in water management for the Western United States. *Journal of the American Water Resources Association* JAWR-20-0084-P.
- Meyers, Z. P., M. D. Frisbee, L. K. Rademacher, N. S. Stewart-Maddox. 2021. Old groundwater buffers the effects of a major drought in groundwater-dependent ecosystems of the eastern Sierra Nevada (CA). *Environmental Research Letters* 16 (4): 044044.
- Morse, A., W. J. Kramber, M. Wilkins, R. G. Allen. 2003. Preliminary computation evapotranspiration by land cover type using TM data and SEBAL. Pages 2956-2958 in *Proceedings of the International Geoscience and Remote Sensing Symposium* held in Toulouse, France, August 2003.
- Nelson, R.F. 1983. Detecting forest canopy change due to insect activity using Landsat MSS. *Photogrammetric Engineering and Remote Sensing* 49(9): 1303-1314.
- Pahlevan, N., S. K. Chittimalli, S. V. Balasubramanian, V. Vellucci. 2019. Sentinel-2/Landsat-8 product consistency and implications for monitoring aquatic systems. *Remote Sensing of Environment* 220: 19-29.
- Pekel, J. F., A. Cottam, N. Gorelick, A. S. Belward. 2016. High-resolution mapping of global surface water and its long-term changes. *Nature* 540 (7633): 418-422.
- Potapov, P., S. Turubanova, M. C. Hansen, A. Tyukavina, V. Zalles, A. Khan, X. P. Song, A. Pickens, Q. Shen, J. Cortez. 2022. Global maps of cropland extent and change show accelerated cropland expansion in the twenty-first century. *Nature Food* 3 (1): 19-28.
- Quinteiro, P., B.G. Ridoutt, L. Arroja, and A. C. Dias. 2018. Identification of methodological challenges remaining in the assessment of a water scarcity footprint: a review. *The International Journal of Life Cycle Assessment* 23 (1): 164-180.
- Ramankutty, N., A. T. Evan, C. Monfreda, J. A. Foley. 2008. Farming the planet: 1. Geographic distribution of global agricultural lands in the year 2000. *Global Biogeochemical Cycles* 22 (1): GB1003.
- Ryan, B. J. and M. H. Freilich. 2008. Landsat Data Distribution Policy. <<https://www.usgs.gov/media/files/landsat-data-distribution-policy-2008>> Accessed 30 May 2022.
- Schumacher, B. L., M. A. Yost, E. K. Burchfield, N. Allen. 2022. Water in the West: Trends, production efficiency, and a call for open data. *Journal of Environmental Management* 306: 114330.
- See, L., S. Fritz, L. You, N. Ramankutty, M. Herrero, C. Justice, I. Becker-Reshef, P. Thornton, K. Erb, P. Gong, H. Tang, M. van der Velde, P. Ericksen, I. McCallum, F. Kraxner, M. Obersteiner. 2015. Improved global cropland data as an essential ingredient for food security. *Global Food Security* 4: 37-45.
- Song, X. P., M. C. Hansen, P. Potapov, B. Adusei, J. Pickering, M. Adami, A. Lima, V. Zalles, S. V. Stehman, C. M. di Bella, M. C. Conde, E. J. Copati, L. B. Fernandes, A. Hernandez-Serna, S. M. Jantz, A. H. Pickens, S. Turubanova, A. Tyukavina. 2021. Massive soybean expansion in South America since 2000 and implications for conservation. *Nature Sustainability* 4 (9):784-792.
- Thenkabail, P. S., P. G. Teluguntla, J. Xiong, A. Oliphant, R. G. Congalton, M. Ozdogan, M. K. Gumma, J. C. Tilton, C. Giri, C. Milesi, A. Phalke, R. Massey, K. Yadav, T. Sankey, Y. Zhong, I. Aneece, D. Foley. 2021. Global cropland-extent product at 30-m resolution (GCEP30) derived from Landsat satellite time-series data for the year 2015 using multiple machine-learning algorithms on Google Earth Engine cloud. *USGS Professional Paper Report Number 1868*, Reston, Va.
- Tilman, D., C. Balzer, J. Hill, and B. L. Befort. 2011. Global food demand and the sustainable intensification of agriculture. *Proceedings of the National Academy of Sciences* 108 (50):20260-20264.
- United Nations, Department of Economic and Social Affairs, Population Division (2019). *World Population Prospects 2019*, Volume I: Comprehensive Tables (ST/ESA/SER.A/426).
- Vijay, V. and P. R. Armsworth. 2021. Pervasive cropland in protected areas highlight trade-offs between conservation

- and food security. *Proceedings of the National Academy of Sciences* 118 (4):e2010121118.
- Wickham, J., S. V. Stehman, D. G. Sorenson, L. Gass, J. A. Dewitz. 2021. Thematic accuracy assessment of the NLCD 2016 land cover for the conterminous United States. *Remote Sensing of Environment* 257:112357.
- White, J. C., T. Hermosilla, M. A. Wulder, N. C. Coops. 2022. Mapping, validating, and interpreting spatio-temporal trends in post-disturbance forest recovery. *Remote Sensing of Environment* 271:112904.
- Wolf, J., T. O. West, Y. Le Page, G. P. Kyle, X. Zhang, G. J. Collatz, and M. L. Imhoff. 2015. Biogenic carbon fluxes from global agricultural production and consumption. *Global Biogeochemical Cycles* 29 (10): 1617-1639
- Woodcock, C. E., R. Allen, M. Anderson, A. Belward, R. Bind-schadler, W. Cohen, F. Gao, S. N. Goward, D. Helder, E. Helmer, R. Nemani, L. Oreopoulos, J. Schott, P. S. Thenk-abail, E. F. Vermote, J. Vogelmann, M. A. Wulder, and R. Wynne. 2008. Free access to Landsat imagery. *Science* 320 (5879): 1011-1011.
- Wulder, M. A., J. G. Masek, W. B. Cohen, T. R. Loveland, C. E. Woodcock. 2012. Opening the archive: How free data has enabled the science and monitoring promise of Land-sat. *Remote Sensing of Environment* 122:2-10.
- Wulder, M. A., T. Hermosilla, J. C. White, N. C. Coops. 2020. Biomass status and dynamics over Canada's forests: Disentangling disturbed area from associated aboveground biomass consequences. *Environmental Research Letters* 15 (9): 094093.
- Wulder, M.A., D.P. Roy, V.C. Radeloff; T.R. Loveland, M.C. Anderson, D.M. Johnson, S. Healey, Z. Zhu, T.A. Scambos, N. Pahlevan, M. Hansen, N. Gorelick, C.J. Crawford, J.G. Masek, T. Hermosilla, J.C. White, A.S. Belward, C. Schaaf, C. Woodcock, J.L. Huntington, L. Lymburner, P. Hostert, F. Gao, A. Lyapustin, J-F. Pekel, P. Strobl, E. Vermote, and B.C. Cook. (In review). Fifty years of Landsat science and impacts. *Remote Sensing of Environment*. In review.
- Yang, Y., M. Anderson, F. Gao, C. Hain, A. Noormets, G. Sun, R. Wynne, V. Thomas, L. Sun. 2020. Investigating impacts of drought and disturbance on evapotranspiration over a forested landscape in North Carolina, USA using high spatiotemporal resolution remotely sensed data. *Remote Sensing of Environment* 238:111018.
- Yang, Y., M. C. Anderson, F. Gao, D. M. Johnson, Y. Yang, L. Sun, W. Dulaney, C. R. Hain, J. A. Otkin, J. Prueger, T. P. Meyers, C. J. Bernacchi, C. E. Moore. 2021. Phenological corrections to a field-scale, ET-based crop stress indicator: An application to yield forecasting across the U.S. Corn Belt. *Remote Sensing of Environment* 257:112337.
- Yang, Y., M. C. Anderson, F. Gao, J. D. Wood, L. Gu, and C. Hain. 2021. Studying drought-induced forest mortality using high spatiotemporal resolution evapotranspiration data from thermal satellite imaging. *Remote Sensing of Environment* 265: 112640.
- Zabel, F., R. Delzeit, J. M. Schneider, R. Seppelt, W. Mauser, and T. Václavík. 2019. Global impacts of future cropland expansion and intensification on agricultural markets and biodiversity. *Nature Communications* 10 (1): 2844.
- Zalles, V., M.C. Hansen, P. V. Potapov, D. Parker, S. V. Stehman, A. H. Pickens, L. L. Parente, L. G. Ferreira, X. P. Song, A. Hernandez-Serna, I. Kommareddy. 2021. Rapid expansion of human impact on natural land in South America since 1985. *Sci Adv.* 7(14): eabg1620.
- Zhu, Z., M. A. Wulder, D. P. Roy, C. E. Woodcock, M. C. Hansen, V. C. Radeloff, S. P. Healey, C. Schaaf, P. Hostert, P. Strobl, J. Pekel, L. Lymburner, N. Pahlevan, and T. A. Scambos. 2019. Benefits of the free and open Landsat data policy. *Remote Sensing of Environment* 224: 382-385.

Authors

Thomas R. Loveland (posthumous), U.S. Geological Survey Earth Resources Observation and Science (EROS) Center, 47914 252nd Street, Sioux Falls, SD 57198, USA

Martha C. Anderson, martha.anderson@usda.gov, USDA, Agricultural Research Service, Hydrology and Remote Sensing Laboratory, 10300 Baltimore Avenue, Beltsville, MD 20705, USA

Justin L. Huntington, justin.huntington@dri.edu, Desert Research Institute, Reno, NV 89512, USA

James R. Irons, james.r.iron@nasa.gov, NASA Goddard Space Flight Center, 8800 Greenbelt Road, Greenbelt, MD, 20771, USA

David M. Johnson, david.m.johnson@usda.gov, National Agricultural Statistics Service, United States Department of Agriculture, 1400 Independence Avenue, SW, Washington, D.C. 20250, USA

Laura E.P. Rocchio, laura.e.rocchio@nasa.gov, Science Systems & Applications, Inc., NASA Goddard Space Flight Center, 8800 Greenbelt Road, Greenbelt, MD, 20771, USA

Curtis E. Woodcock, curtis@bu.edu, Department of Earth and Environment, Boston University, MA 02215, USA

Michael A. Wulder, mike.wulder@nrcan-rncan.gc.ca, Canadian Forest Service (Pacific Forestry Centre), Natural Resources Canada, 506 West Burnside Road, Victoria, British Columbia V8Z 1M5, Canada

Dedication

We dedicate this article to the memory of Dr. Thomas Loveland who passed away May 13, 2022, after he initiated the development of this manuscript. Tom was an inspirational and accomplished leader in the field of land cover remote sensing during his long career with the USGS Earth Resources Observation and Science (EROS) Center. He was an unwavering advocate for the Landsat Program in his role as co-chair of Landsat Science Teams spanning a duration of 20 years. Tom brought wisdom, vision, and good humor to his leadership of the Teams. He was a friend and valued colleague to all of us and he will be sorely missed.

m with the final value being adjusted with the base at Nyanza, both surveyed by the Katanga-Rhodesia Boundary Commission. The deflection of the vertical was constrained to zero at point "A". The projection adopted for the general map of Katanga was the Lambert Conical Orthomorphic with two standard parallels at $\phi_N = 6^\circ 30' S$ and $\phi_S = 11^\circ 30' S$ and a central meridian, $\lambda_0 = 26^\circ E$.

Thanks to a paper in *Survey Review*, April 1997 by Dare and Mutale, a brief history of geodetic surveys in Zambia were detailed: "Between 1949 and 1964, the Directorate of Colonial Surveys, Federal Surveys, and the Directorate of Overseas Surveys, established 12 triangulation nets and three traverse loops. The main areas of primary control may be grouped as follows: Part of Arc of the 30th Meridian; Fort Jameson (Chipata)/Malawi Network; Isoka Network; Zambia Main Network; Copperbelt Network; Solwezi/Kasama/Mumbwa Loop; Fort Rosebury (Mansa) – Congo (Zaire) link; Livingstone Memorial Area – Mansa Loop; Mwinilunga Loop Traverse; Luwingu series and Mansa loop; Mankoya loop Traverse; Kalomo Livingstone loop Traverse. The network configuration consists of a series of (a) Triangles; (b) Braced quadrilaterals; (c) Centre point polygons; (d) Double centred polygons; (e) Traverse legs. As a rule of thumb, the orientation was controlled by azimuth observations every 10 stations and the allowable misclosure was not to exceed $2''\sqrt{n}$, where n is the number of intervening legs between astronomical stations. The side lengths in primary traverse are approximately 30 km; in other cases the lengths of sides are approximately 60 km. For (a)-(d) a deliberate effort was made to have well conditioned triangles by avoiding angles less than 40 degrees."

The Tshinsenda baseline is located in the Copperbelt Province of Zambia. Since the world market in copper has plummeted, the economy of Zambia has suffered and great efforts are being expended to convert the economy to an agricultural base. The majority of papers on surveying and mapping topics published on Zambia are now addressed to the establishment of a national cadastre for a land registration system. Land tenure through 99-year leases is a current topic thought to be the country's economic salvation. Professor Peter Nsombo published a paper with L. Combrinck of the Hartebeeshoek Radio Astronomy Observatory regarding the establishment of a continuously observing reference station in Lusaka (ZAMB). The transformation parameters expressed in the standard American convention sign for rotations from Arc Datum 1950 to WGS84 Datum for *all* of Zambia are: $\Delta X = -152 \text{ m} \pm 0.4 \text{ m}$, $\Delta Y = -60 \text{ m} \pm 0.4 \text{ m}$, $\Delta Z = -297 \text{ m} \pm 0.4 \text{ m}$, $R_x = -12'' \pm 0.4''$, $R_y = 1'' \pm 0.8''$, $R_z = 8'' \pm 1''$, $\Delta s = -8.328 \pm 1.773 \text{ ppm}$, and this solution was based on 11 observed points. A pilot project was undertaken in an area of Lusaka that developed transformation parameters that were different from the above parameters in *excess of 10 meters per translation component*. As a basis of comparison, NGA lists the 3 parameter transformation from Arc 1950 to WGS 84 as: $\Delta X = -147 \text{ m} \pm 21 \text{ m}$, $\Delta Y = -74 \text{ m} \pm 21 \text{ m}$, $\Delta Z = -283 \text{ m} \pm 21 \text{ m}$, and this solution was based on 5 points.

Thanks to Malcolm A. B. Jones of Perth, Australia for the Katanga data.

Zambia Update

In 2019, Mr. Andrew M. Silwembe, a government employee of Zambia, earned a Master's degree in Engineering in Geodesy and Geo-Informatics by collocating at two networks that comprised points common to the international boundaries between Zambia and Malawi as well as between Zambia and Moçambique with GPS observations. Mr. Silwembe used the Leica Ski software as well as the U.S. National Geodetic Survey's OPUS software for his analysis. The math model employed was the classical Molodensky-Badekas 7-parameter transformation, but with a curious twist.

The classical 7-parameter Molodensky model uses the geocentric coordinates of the classical datum origin as the origin point for the rotation of the classical coordinates (Arc50) to the inertial coordinates (WGS84). Silwembe instead chose the geometric center of the Arc50 Datum of Malawi and the geometric center of the Tete 1960 Datum of Moçambique! I think this is a non-sensical approach, since using a rotation origin inside of the network of points used will have a negligible affect to the transformation scalar and to the magnitude of the translation components. Decades ago, when I was developing the relation among the classical datums of Trinidad and of Venezuela, the datum origins were within the population samples of the datums affected, so I used a simple 7-parameter Bursa Wolf transformation model. Conversely, when I developed the relation of the classical datum of Guayaquil, Ecuador and of the PSAD56 datum, I used the full 7-parameter Molodensky transformation model to significantly decrease the magnitude of the translation parameters by using a larger scalar. Nevertheless, Silwembe's transformation parameters along with his rotation origin (in Malawi) are as follows for Zambia-Malawi to WGS84: $X_0 = 5,209,545.197 \text{ m}$, $Y_0 = 3,385,668.285 \text{ m}$, $Z_0 = -1,441,109.365 \text{ m}$, $\Delta X = 166.705 \text{ m} \pm 0.103 \text{ m}$, $\Delta Y = 75.034 \text{ m} \pm 0.103 \text{ m}$, $\Delta Z = 307.072 \text{ m} \pm 0.103 \text{ m}$, $R_x = -11.267585'' \pm 0.3862''$, $R_y = -3.557593'' \pm 0.5159''$, $R_z = 2.429121'' \pm 0.9193''$, $\Delta s = 2.429121 \text{ ppm} \pm 1.8187 \text{ ppm}$. Note that the σ *a posteriori* is $\pm 0.3560 \text{ m}$, based on 12 collocated points.

Silwembe's transformation parameters along with his rotation origin (in Moçambique) are as follows for Zambia-Moçambique to WGS84: $X_0 = 5,260,391.453 \text{ m}$, $Y_0 = 3,239,199.932 \text{ m}$, $Z_0 = -1,580,682.477 \text{ m}$, $\Delta X = 161.159 \text{ m} \pm 0.081 \text{ m}$, $\Delta Y = 82.201 \text{ m} \pm 0.081 \text{ m}$, $\Delta Z = 298.851 \text{ m} \pm 0.081 \text{ m}$, $R_x = -11.2863'' \pm 0.8161''$, $R_y = -2.0981'' \pm 1.5582''$, $R_z = 5.8898'' \pm 0.5399''$, $\Delta s = -5.3155 \text{ ppm} \pm 0.8584 \text{ ppm}$. Note that the σ *a posteriori* is $\pm 0.2724 \text{ m}$, based on 13 collocated points.

Finally, note that the sense of the SKI rotations are opposite standard American/Australian convention.

The contents of this column reflect the views of the author, who is responsible for the facts and accuracy of the data presented herein. The contents do not necessarily reflect the official views or policies of the American Society for Photogrammetry and Remote Sensing and/or the Louisiana State University Center for GeoInformatics (C⁴G).

This column was previously published in *PE&RS*.

JOURNAL STAFF

Editor-In-Chief

Alper Yilmaz, Ph.D., PERSeditor@asprs.org

Associate Editors

Rongjun Qin, Ph.D., qin.324@osu.edu
Michael Yang, Ph.D., michael.yang@utwente.nl
Petra Helmholtz, Ph.D., Petra.Helmholz@curtin.edu.au
Bo Wu, Ph.D., bo.wu@polyu.edu.hk
Clement Mallet, Ph.D., clemallet@gmail.com
Prasad Thenkabail, Ph.D., pthenkabail@usgs.gov
Ruisheng Wang, Ph.D., ruisheng@ucalgary.ca
Desheng Liu, Ph.D., liu.738@osu.edu
Valérie Gouet-Brunet, Ph.D., valerie.gouet@ign.fr
Dorota Iwaszczuk, Ph.D., dorota.iwaszczuk@tum.de
Qunming Wang, Ph.D., wqm11111@126.com
Filiz Sunar, Ph.D., fsunar@itu.edu.tr
Norbert Pfeifer, np@ipf.tuwien.ac.at
Jan Dirk Wegner, jan.wegner@geod.baug.ethz.ch
Hongyan Zhang, zhanghongyan@whu.edu.cn
Dongdong Wang, Ph.D., ddwang@umd.edu
Zhenfeng Shao, Ph.D., shaozhenfeng@whu.edu.cn
Ribana Roscher, Ph.D., ribana.roscher@uni-bonn.de
Sidike Paheding, Ph.D., spahedin@mtu.edu

Contributing Editors

Highlight Editor

Jie Shan, Ph.D., jshan@ecn.purdue.edu

Feature Articles

Michael Joos, CP, GISP, featureeditor@asprs.org

Grids & Datums Column

Clifford J. Mugnier, C.P., C.M.S., cjmce@lsu.edu

Book Reviews

Sagar Deshpande, Ph.D., bookreview@asprs.org

Mapping Matters Column

Qassim Abdullah, Ph.D., Mapping_Matters@asprs.org

GIS Tips & Tricks

Alvan Karlin, Ph.D., CMS-L, GISP akarlin@Dewberry.com

ASPRS Staff

Assistant Director — Publications

Rae Kelley, rkelly@asprs.org

Electronic Publications Manager/Graphic Artist

Matthew Austin, maustin@asprs.org

Advertising Sales Representative

Bill Spilman, bill@innovativemediasolutions.com

Landsat's Enduring Legacy — Pioneering Global Land Observations from Space is Now Open Access in Available PDF Format

After more than 15 years of research and writing, the Landsat Legacy Project Team, in collaboration with the American Society for Photogrammetry and Remote Sensing (ASPRS), published an account of monitoring the Earth's lands for a half-century with Landsat. Born of technologies that evolved from the Second World War, Landsat not only pioneered global land monitoring but, in the process, drove innovation in digital imaging technologies and encouraged the development of global imagery archives. Access to this imagery led to early breakthroughs in natural resources assessments, particularly for agriculture, forestry, and geology. The technical Landsat remote sensing revolution was not simple or straightforward. Early conflicts between civilian and defense satellite remote sensing users gave way to disagreements over whether the Landsat system should be a public service or a private enterprise. The failed attempts to privatize Landsat nearly led to its demise. Only the combined engagement of civilian and defense organizations ultimately saved the Landsat program from the brink of collapse. With the emergence of 21st century Earth system science research, the full value of the Landsat concept and its continuous 50-year global archive has been recognized and embraced. Discussion of Landsat's future continues but its heritage will not be forgotten. This innovative satellite system's vital history is captured in this notable volume on *Landsat's Enduring Legacy*.

Download the open access PDF from ASPRS at <https://my.asprs.org/landsat>.

The hardcover version can be purchased directly from ASPRS by visiting www.asprs.org/landsat

NEW ASPRS MEMBERS

ASPRS would like to welcome the following new members!

Ian James Anderson	Justin Heitman
A. F. M. Fakhrol Azam	Jennifer Looper
Andrew Babian	William Lyons
Patrick Bassham	Omolola Akinola Ologunorisa, PhD
Philippa Rose Burgess	Audrey Rager, PhD
Eric Carlson	Randall Thompson
John Clinton Cothrun	Christopher Michael Trevino
Diana Botchway Frimpong	Brandon Zinsious

FOR MORE INFORMATION ON ASPRS MEMBERSHIP, VISIT
[HTTP://WWW.ASPRS.ORG/JOIN-NOW](http://www.asprs.org/join-now)

Hydrological Topography Data Set (HTD)— The Data Set for High Resolution 2D Urban Flood Modeling

Che-Hao Chang, Chih-Hung Hsu, Chih-Tsung Hsu, Shiang-Jen Wu, and Po-Hsien Chung

Abstract

This study investigated the demand of data for better high resolution two-dimensional (2D) hydraulic modeling and proposes a data set named “Hydrological Topography Data Set” (HTD for short) for this purpose. Derived from airborne lidar point cloud, the HTD comprises three parts: (1) High Resolution Hydraulic Three-Dimensional Features: high resolution three-dimensional vector data that preserves the locations and elevations of topography breaklines, (2) Hydraulic Digital Elevation Model: high resolution (1×1 m) DEM enhanced by the terrain breaklines to preserve the landscape characteristics, and (3) Hydraulic Digital Surface Model: high resolution (1×1 m) DSM conditioned by removing the height of vegetation and temporary objects. With HTD, hydraulic features such as drainages with 10 m of width can be identified and properly set up in numerical models, thus can help simulating and accessing the flood in urban area more in detail. Through case studies we demonstrate how HTD can affect the results of hydraulic modeling. The results show that HTD can help modelers to construct proper mesh (or computational grids) for 2D hydraulic modeling, and preserve topography characteristics (i.e., shape and elevation), which improves the modeling results in terms of spatial resolution and physical rationality, while still keeping the computation efficient.

Introduction

The Need of Data for High Resolution Modeling

According to the records of the past 100 years, Taiwan suffers from 3–4 typhoons every year, and the accompanying flooding is always a huge threat. To respond to the climate change and increasing frequency and intensity of rainfall event, Taiwan Water Resources Agency has developed a framework that creates a potential flooding map according to various rainfall scenarios. This framework has become the main basis for current flooding-related disaster prevention and response decision making.

Che-Hao Chang is with the Dept. of Civil Engineering, National Taipei University of Technology, Taiwan 1, Sec. 3, Zhongxiao E. Rd., Taipei City 10608, Taiwan.

Chih-Hung Hsu is with the G T International Engineering Consultants, Ltd., Taiwan 2F., No.215, Sec.3, Nanjing E. Road, Taipei City 104, Taiwan (aaronhsu219@gmail.com).

Chih-Tsung Hsu is with the National Applied Research Laboratories National Center for High-performance Computing, Taiwan No. 7, R&D 6th Rd., Hsinchu Science Park, Hsinchu City, Taiwan.

Shiang-Jen Wu is with the Dept. of Civil and Disaster Prevention Engineering, National United University, Taiwan No.1, Lienda, Miaoli County 360301, Taiwan.

Po-Hsien Chung is with the Water Resources Planning Institute, Water Resources Agency, Ministry of Economic Affairs No.1340, Jhong-jheng Rd., Wu-fong, Taichung City 413, Taiwan.

Contributed by Zhenfeng Shao, November 14, 2020 (sent for review October 8, 2021; reviewed by Cheng Zhong, Hongping Zhang, Nan Yang).

Due to the dense population and urban development in Taiwan, the demand for flood area mapping has gradually increased from the township level to the village level, and even at the community level. With this high-precision requirement, it is necessary to consider the use of higher-resolution spatial data to show the detailed physical characteristics of the flooding process. In particular, the technological advancement in the production of numerical terrain models, using airborne lidar technology, has produced island-wide Digital Elevation Model (DEM) and Digital Surface Model (DSM) with a resolution of $1 \text{ m} \times 1 \text{ m}$ across Taiwan in the past 10 years. If we can make good use of this high-precision spatial information, there will be a great opportunity to improve the results of flooding simulation, especially in the urban areas. However, the current DEM product contains only bare-earth elevation. If the elevation of buildings is not included, the simulation result will not show the effects from the buildings. On the other hand, the DSM contains the elevation of features such as vegetation, buildings, and other man-made structures. In practice, the surface elevation of vegetation, most likely the trees, behave like “blocks” for water flow in hydraulic modeling. Hence, DSM is not applicable for two-dimensional (2D) hydraulic modeling. To overcome the shortcomings of current available data, more information is required for high resolution (HR) modeling.

Review of DEM Data for Hydrologic and Hydraulic Modeling

Delineating desirable watersheds is essential for most of the hydrologic and hydraulic modeling applications. The most well-known watershed-delineation algorithm is the D8 algorithm, which is introduced by O’Callaghan and Mark (1987). The D8 algorithm is commonly used due to its simplicity; however, to perform the D8 algorithm, the raw DEM has to be modified by filling the sinks and sometimes needs to be reconditioned by burn-in the stream into the original DEM. The “sink filling” and “stream burning” approaches altered the raw DEM and may not be suitable in some applications. Studies have come up with different algorithms to avoid the alteration of raw DEM, such as Zhang et al. (2020) and Kenny et al. (2008). In some cases, the delineated watershed may not align with real topography. Kenny and Matthews (2005) develop an algorithm that take not only the channel network vector, but also the waterbody polygon into account, to delineate a more accurate and desirable watershed.

In the current flood simulation applications, there have been many cases of applying lidar data. Medeiros *et al.* (2011) applied lidar DEM on typhoon-induced huge wave simulation; Kain *et al.* (2019) used lidar DEM on tsunami simulation; Bodoque *et al.* (2016) produced high-precision DEM, combined with river water depth measurement and Triangulated Irregular Network (TIN) data derived from lidar point cloud, and performed a 500-year frequency flood simulation. Al-Suhili *et al.* (2019) discussed the difficulty of integrating flood modeling and high-precision spatial data and proposed a framework for rainfall

Photogrammetric Engineering & Remote Sensing
Vol. 88, No. 7, July 2022, pp. 439–450.

0099-1112/22/439-450

© 2022 American Society for Photogrammetry
and Remote Sensing
doi: 10.14358/PERS.20-00115R2

forecasting and flood early warning system. Luppichini *et al.* (2019) proposed high-precision topographic data, which can show the characteristics of hydraulic structures, and improve the accuracy of flood simulation. Dhungel *et al.* (2019) used lidar-derived digital terrain models (DTMs) in one dimensional (1D) and 2D flood modeling in urban areas. Pinos *et al.* (2019) compared modeling results from multiple 1D river models, along with cross-section data from different sources.

Ding *et al.* (2021) combined Multi-Temporal Interferometric Synthetic Aperture Radar (MT-InSAR), geo-detector, and Long Short-Term Memory (LSTM) for monitoring, analysis, and prediction of surface subsidence in the main urban districts of Wuhan. Shao *et al.* (2021) propose an ecological evaluation standard framework by designing an ecosystem service value monitoring workflow based on the establishment of multi-level grids. Shao *et al.* (2019) analyze multi-temporal Landsat data and run-off data derived from the INFOWORKS model to determine the relations between impervious area ratio and run-off pattern in urban area and discovered that accurate DEM is needed for detailed multi-scale monitoring, especially for flat areas such as most urban areas. Annis *et al.* (2020) compared the DEM with resolution of 10 m, 1 m, and 0.25 m, and applied them to flood modeling. The results show that high-precision DEM provided by UAV is applicable in the case of small catchment and rapid run-off response. The above articles show that applying high-resolution lidar DEM has become a trend in urban flood modeling. However, due to the large size of high-resolution data and the required computing resources, flooding simulation in large areas is still difficult. To perform high-resolution modeling at the community level, small-scale drainage such as drainage with width less than 10 m in urban areas must be considered in the model. However, such small-scale drainage cannot be presented as 2D features when using DEM with resolution of 40 m. Solving this problem requires improvement of the spatial resolution, but this will also significantly increase the amount of calculation resources, which is not available in most of the cases.

High-resolution DEM is not necessary for making high-resolution flood simulation. In fact, using DEM along with line features such as a breakline in hydraulic models has been implemented for a long time. For example, Scarlatos (1989), Liu (2008), Liu and Zhang (2013), and Rutzinger *et al.* (2016) have all verified that combining coarse resolution DEM and three-dimensional (3D) breaklines, the geographic accuracy of spatial features can still be maintained. High-density point cloud of airborne lidar provides pixel-wide breakline acquisition capabilities, such as Brugelmann (2000) and Hingee *et al.* (2019). Yang *et al.* (2016) developed an algorithm to extract Terrain characteristics. Dhungel *et al.* (2019) used airborne lidar data to determine the hydro-flatten area.

Typical DEM excludes the building elevation from the terrain. However, when performing urban flood modeling, the presence of the building will block the water flow, and the simulation needs to be considered. Studies that consider the impact of buildings in flood modeling are as follows. Alivio *et al.* (2017) applied aerial telemetry in hydrodynamic simulation. Li *et al.* (2019) developed high-performance algorithms to evaluate flood extent using DEM and Morphology.

Rong *et al.* (2020) propose a high-precision simulation that combines digital city model and flood simulation under the concept of Building Information Modelling. Shen (2020) discusses the influence of DEM and the roughness on two-dimensional flood modeling in the building treatment method. Sholichin and Qadri (2020) retrieve multiple types of data, such as buildings, DEM, land use, etc. from a hydrology database for constructing models to predict the flow rate and calculate the flood risk. Some studies also have discussed buildings' impact on flood modeling, such as Afifi *et al.* (2019), Kurniyaningrum *et al.* (2019), and Bove *et al.* (2020).

Based on the demand of high-resolution flood modeling in urban areas, spatial features such as small drainage and buildings need to be considered in the digital terrain model production process. With reference to the National Hydrography Dataset (NHD) and NHDPlus HR's data concepts for national channels proposed by United States Geological Survey (USGS), this paper proposes the Hydrologic Topography Dataset (HTD), which includes the Hydraulic Digital Elevation Model (HyDEM), the Hydraulic Digital Surface Model (HyDSM), and High Resolution Hydraulic 3D features.

The HyDEM is used to highlight, but is not limited in the channel details in DEM on the three-dimensional model. Spatial features like waterbody, dikes, and buildings are also considered. To achieve this, the terrain breaklines, which preserve the channel and building characteristics, are used to interpolate into the DEM to create a format of data that allows users to display and measure channel parameters at resolution of 1 m. The High Resolution Hydraulic 3D features aim at the spatial features that need to be emphasized in the hydraulic model, such as drainage channels, buildings, etc., and is created as breaklines on the terrain to preserve its three-dimensional spatial accuracy as much as possible.

HTD as Part of the Taiwan 3D National Basemap (3DNB) Program

In Taiwan, nationwide systemic terrain survey using lidar was conducted after Typhon Morakot in 2009, which was a devastating event that caused the loss of many lives and a loss to the economy. In the beginning, the lidar is used to produce high resolution (1 m × 1 m and 5 m × 5 m) of DEM and DSM for the purposes of monitoring and investigating the change of the landscape to help researchers identify the locations of potential hazards. Since then, more and more applications using the lidar-derived data have emerged from different research areas, such as sociology, forestry, etc.

In 2017, the Taiwan government initiated the 3D National Basemap (3DNB) Program, which aims to build a compressive database of survey products that facilitate the development of infrastructure and many aspects of research. From 2018, the Department of Land Administration (DoLA) begin to cooperate with Water Resources Planning Institute (WRPI) on the topic of HTD, which is one of the subprograms of the 3DNB Program. In the 2018 DoLA-WRPI joint project, "Application of Hydro Digital Elevation Model on High Resolution Inundation Modeling", we proposed a set of survey products for performing higher quality hydraulic modeling. The proposed data sets and their definitions are shown in Table 1.

Table 1. The Hydrological Topography Data Set (HTD) and their descriptions,

Data (Sets)	Definition
High Resolution Hydraulic 3D Features	
(1) Building Layer	3D polygon that preserves the plan view shape and elevation of buildings
(2) Bank Layer	3D vector polygon that stores the bank top paths and their elevation at vertices
(3) Waterbody Layer	3D polygon that stores the waterbody edges and the water surface elevation at edge vertices
(4) Boundary Layer	2D polyline that store the boundary line of the elevation data
(5) Sea-Dike Layer	3D polyline that stores the sea-dike top paths and their elevation at their vertices
Hydraulic DEM (HyDEM)	High resolution (1 m × 1 m) DEM with enhancement by imposing topography breaklines on the raster grids such as Layers (2)–(5).
Hydraulic DSM (HyDSM)	High resolution (1 m × 1 m) DSM in addition to HyDEM with enhancement of the Building Layers at topography breaklines but with conditioning by removing the height of vegetation and temporary objects.

3D = three-dimensional; 2D = two-dimensional; DEM = Digital Elevation Model; DSM = Digital Surface Model.

All the HTD components are derived from the same lidar point cloud with density of at least two points per square meter. The five layers of High Resolution Hydraulic 3D Features, in the format of polygon or polyline, are created by a series of automatic and manual digitizing processes. Extra information such as ortho images are typically used to help identify the object and digitize the data. The HyDEM is created by resampling the point clouds to regular raster grids with $1\text{ m} \times 1\text{ m}$ resolution, then burn-in the elevation value from the above-mentioned Bank Layer and Sea-Dike layer, to keep the elevation at these break-lines correct. The HyDSM is created by the same way as the HyDEM but with an extra burn-in process using building elevation. In terms of data accuracy, the current requirements for HTD data quality assurance and quality control (QA/QC) are as follows: (1) the average difference of field examination on a horizontal control system is lower than 10 cm, and the vertical one is lower than 20 cm; (2) the maximum allowable vertical difference of field examination to result HyDEM is less than 35 cm, for which the root-mean-square error is around 15 cm.

As shown in Figure 1, when the plane position (x, y) of the bankline is identified, then the corresponding elevation z can be obtained from the point cloud, hence the three-dimensional position (x, y, z) of the entire bankline can be defined. Similarly, the three-dimensional breaklines of buildings, waterbody boundaries, and sea-dikes can be obtained. Figure 2 shows an example of HyDEM development. Before the burn-in process, the elevation of the DEM along the bankline is relatively lower. After burn-in of the bankline information, the DEM elevation along the bankline is raised to the correct elevation of the true topography.

Preliminary Concepts of HTD Components and Their Usage

The current Digital Terrain Models (DTMs) provided by LoSA has two types – Digital Elevation Model (DEM) and Digital Surface Model (DSM). The most significant difference between DEM and DSM is that DEM has no information of building elevation; therefore, when using it, the effect of a building could be overlooked. On the other hand, the DSM contains too much information for flood modeling.

For example, the elevation of treetops on the raster could become the obstructions of water, but in the real world only tree trunks affect

the flow but cannot actually “block” the water flow. For high resolution urban flood modeling, we will need data that is different from currently available DTM products. Following are the concepts of HTD components and the purpose of their usage.

The Building Layer

In USGS defined “pure lidar DEM”, there are artifacts at water surface or manmade structures which make the data not suitable for mapping purposes or creation of topographic contours. To resolve this, USGS defines “Hydro-Flattened DEM” and “Enhanced Hydro-Flattened DEM” that use breaklines to derive higher quality surface for waterbodies and manmade structures such as single-line drainage, ridges, bridge crossings, and buildings (USGS, 2020). For modeling floods in an urban area, well-delineated boundaries of buildings are important when we want to simulate how the water is flowing on the streets and between buildings. Hence in the proposed HTD we intend to include the Building Layer, which is defined as polygon layers that depicts the boundary of buildings and preserve the elevation of buildings in their attribute tables.

The Sea-Dike Layer

In 2D flood modeling, the sea-dike elevation is essential information for the coastal area, because in some cases the ocean waves could overtop the sea dike. If the location and elevation of the dike is wrong, the modeling results will be incorrect. In the current DoLA-provided Taiwan e-map, “sea-dike” layers are available with the horizontal location only. Besides, the line is not always at the top of the dike (Figure 3). In the proposed HTD, we include the Sea-Dike Layer as 3D breaklines along the top of the sea dikes and preserve the elevation at the line vertices. Similar to the Building Layer, this Sea-Dike Layer can be used to delineate higher quality DEM, and also enhance the quality and correctness of 2D flood modeling at coastal area.

The Bank Layer

In different DTMs (i.e., DEM, DSM, HyDEM, and HyDSM), the elevation of each raster grid is averaged in some way, hence it becomes harder to preserve the elevation of a specific location as the grid size increases. In 2D hydraulic modeling, the elevation of a channel bank is essential.

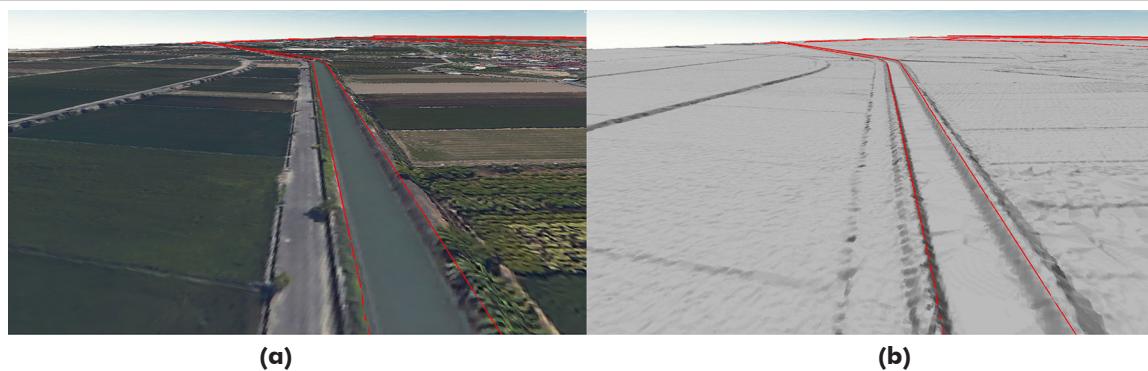


Figure 1. High Resolution Hydraulic Three-Dimensional (3D) feature digitization.

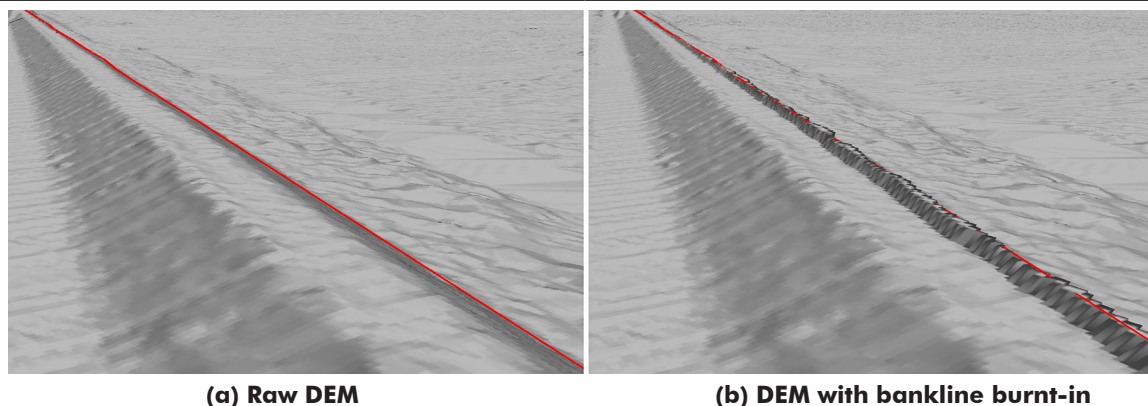


Figure 2. Example of Hydraulic DEM (HyDEM) development. DEM = Digital Elevation Model; DSM = Digital Surface Model.

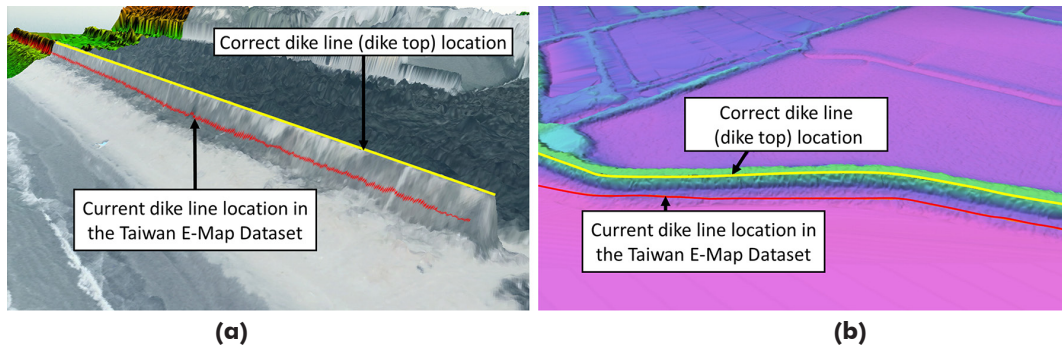


Figure 3. Illustration of current sea dike breakline data and proposed Sea-Dike Layer data.

It affects how the water exchange between the channel within bank lines and the area outside the bank lines.

Figure 4 shows the profiles of a channel cross-section from different resolutions of DEM. We can tell from the figure that the bank elevation decreases as the DEM grid size increases. Moreover, the location (on the “Cross Section Distance” axis) of banktop also shifts when using DEM of different resolutions. Another use of the bankline is to help the modeler to generate adequate mesh for modeling. In many applications of 2D hydraulic modeling, the bankline is used as the boundary for generating computation grid. For example, Figure 5 demonstrates typical 2D flood model computing mesh, which is derived using the bankline to determine the boundary of channels.

The Boundary Layer and Waterbody Layer

In the current DEM provided by LoSA, the sea area is defined as an area outside the data boundary, which means there is no data value stored (no raster grids exist) at the sea area (Figure 6). On the other hand, the rivers and waterbodies inland are inaccurate, because in current data

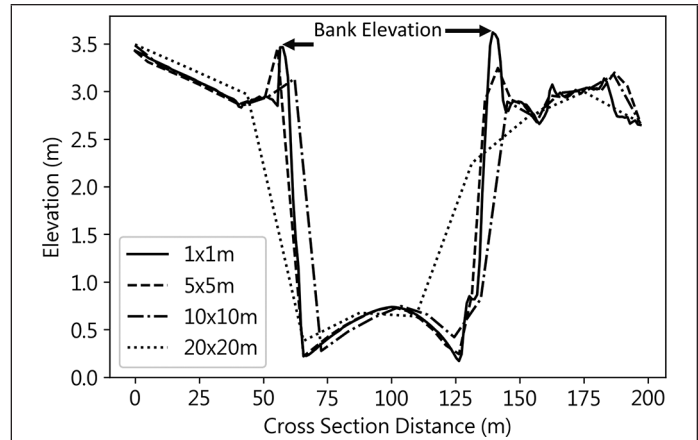
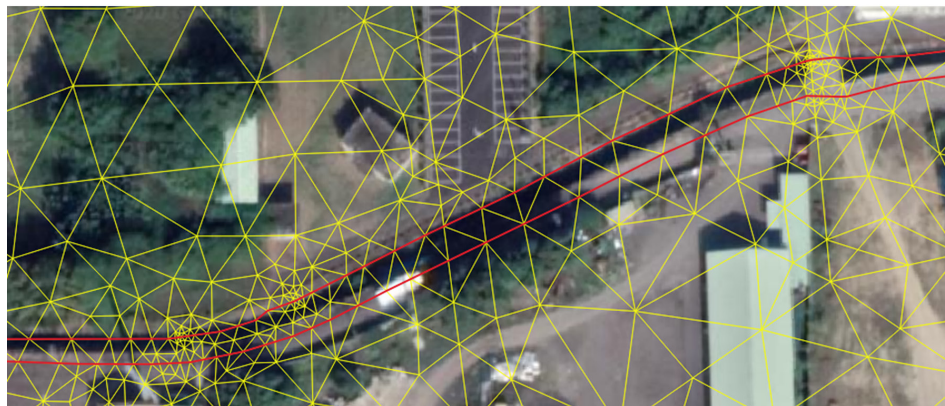


Figure 4. Channel cross-sections derived from DEM of different resolutions.



(a)



(b)

Figure 5. Example of bankline used for two-dimensional (2D) mesh generation.

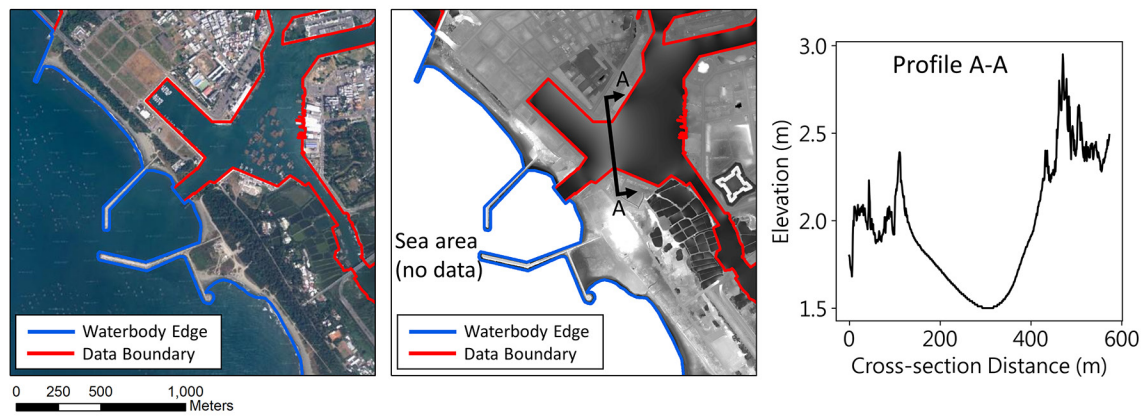


Figure 6. Example of artifacts and missing data in typical digital elevation model (DEM).

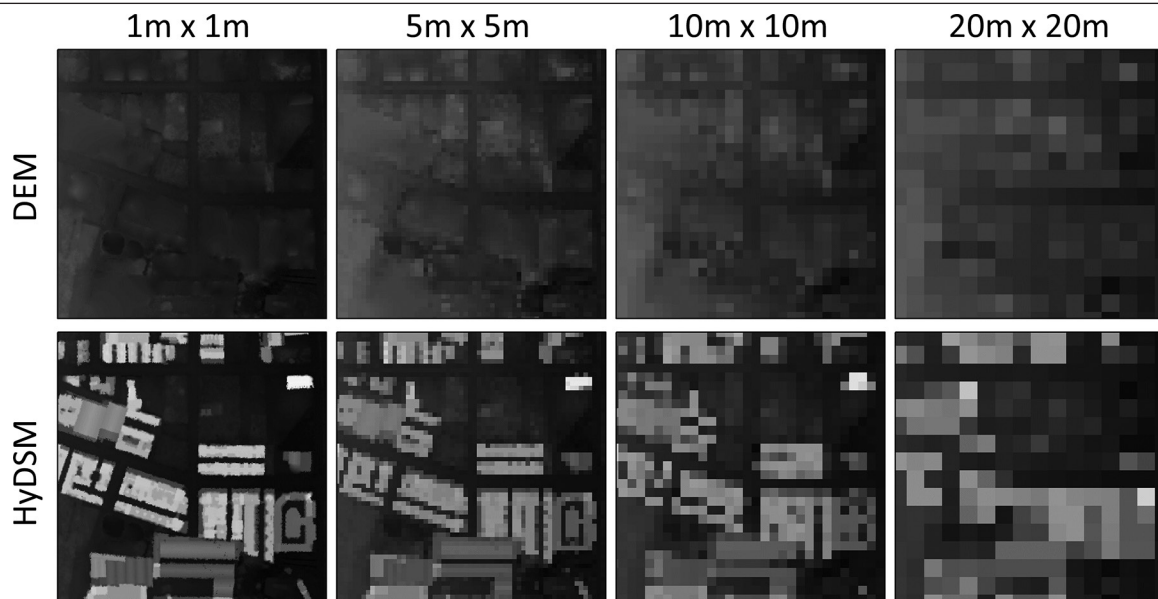


Figure 7. Compare digital terrain models (DTMs) in different resolutions.

processing to the lidar points clouds, inland rivers and waterbodies are removed. In the derived DEM, the elevation at those areas is interpolated from the point cloud nearby, hence often times it has artifacts (Figure 6) and is not suitable for hydraulic modeling. For 2D hydraulic modeling, the two issues mentioned above could pose problems. In such a case, the proposed Boundary Layer and Waterbody Layer can be used for modifying or replacing data within the area with incorrect or missing data.

The HyDEM and HyDSM

We define the HyDEM as “enhanced” $1\text{ m} \times 1\text{ m}$ DEM, which uses the lidar-derived bank lines to delineate the elevation of channel banks. This is to keep the elevation of channel banks, because in some cases the bank elevation in DEM is discontinuous due to the resampling process that averages out the elevation of lidar point cloud within each grid along the bank line. The discontinuity usually occurs when the DEM resolution is coarser than the man-made structure along the bank lines, such as river dikes or thin flood walls. On the other hand, we define the term HyDEM as “conditioned” $1\text{ m} \times 1\text{ m}$ DSM with building elevation, which is the DEM data but with building elevation adding upon it, or it can be seen as the DSM data with vegetation and temporary objects, such as cars, removed.

Conceptually, the building elevation should be considered in the flood modeling because it’s part of the physical world, and it should affect the water flow during flood event. However, most of the current

implementations of hydraulic modeling leave out the information of building elevation, because they use DEM data with resolution of $10 \times 10\text{ m}$ or even coarser resolution, such as 20×20 or $40 \times 40\text{ m}$. The reason of using coarse resolution of DEM is that most of the current model require heavy computation resource to perform the calculation when using high resolution DEM. Another reason for using the DEM without building elevation is when resampling DEM from high resolution (e.g., $1\text{ m} \times 1\text{ m}$) to coarser resolutions (e.g., $5\text{ m} \times 5\text{ m}$ or $10\text{ m} \times 10\text{ m}$), the resample process will aggregate the elevations within each resampled grid, regardless the numerical methods (e.g., bilinear, cubic, etc.) being used. This will result in improper data for hydraulic modeling, because when the elevation of ground and buildings “merged” together, the resampled elevation can neither represent the ground elevation, nor the building elevation. Figure 7 shows the example of resampling $1\text{ m} \times 1\text{ m}$ DEM and HyDEM to $5\text{ m} \times 5\text{ m}$, $10\text{ m} \times 10\text{ m}$, and $20\text{ m} \times 20\text{ m}$. As the grid size increases, the edges of buildings become more blur and it is harder to identify the man-made structures from the data.

Moreover, when conducting urban flood modeling, we often use gauge-measured water elevation to validate modeling results. When using different resolutions of HyDEM, the elevation where water level gauge locates are affected. Figure 8 shows the elevation of the An-Chung water level gauge in the Sanyei catchment in Tainan City. It observed that coarser resolution HyDEM affect the elevation more than high resolution HyDEM. The subfigure 5 and 6 of Figure 8 depicts that

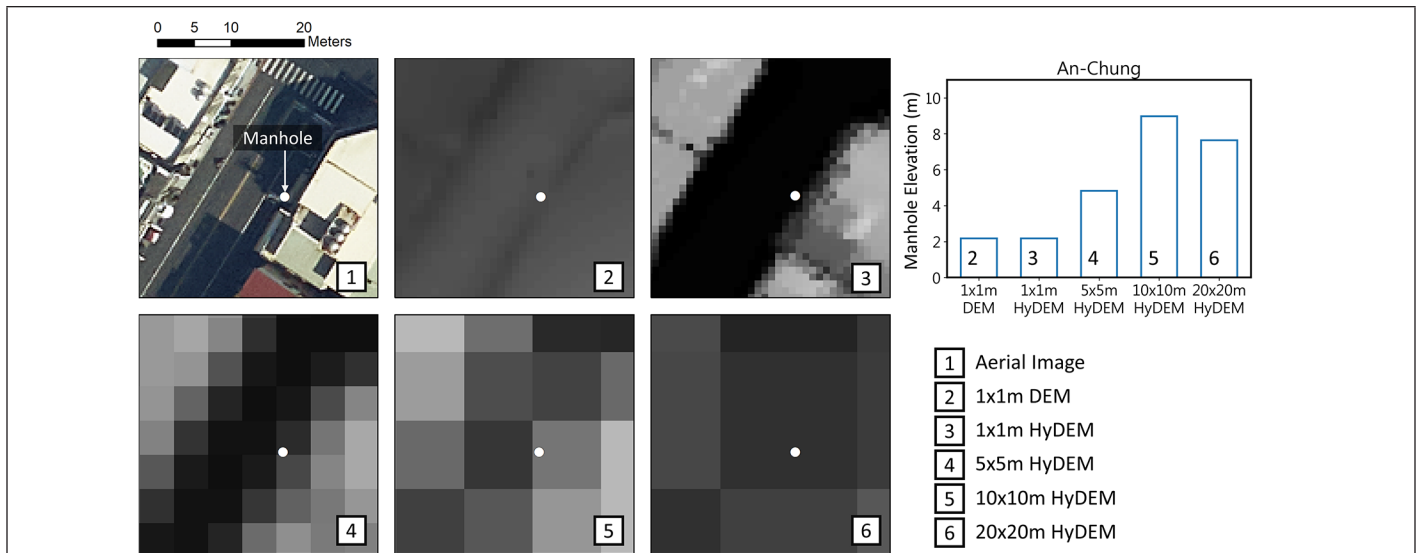


Figure 8. Digital elevation model's (DEM's) resolution effects on elevation at gage location. HyDEM = hydraulic digital elevation model.

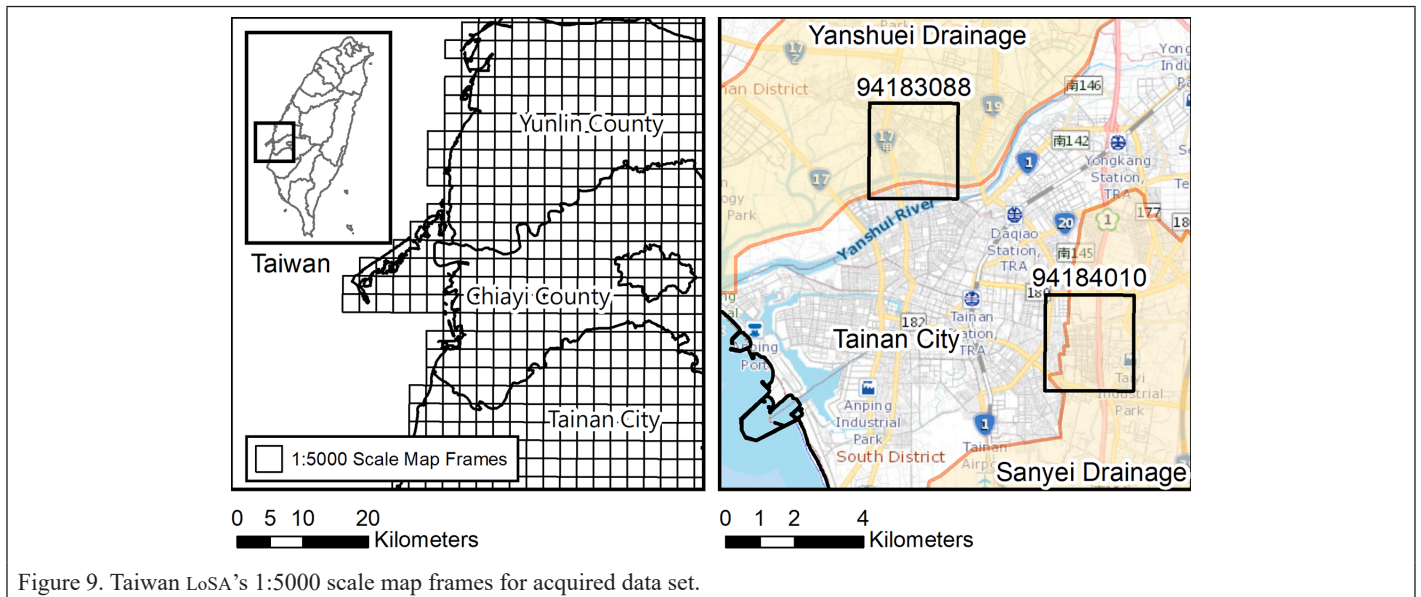


Figure 9. Taiwan LoSA's 1:5000 scale map frames for acquired data set.

when the grid size is $5\text{ m} \times 5\text{ m}$, the road feature is still recognizable, but not when the grid size is $10\text{ m} \times 10\text{ m}$, and $20\text{ m} \times 20\text{ m}$. When the HyDEM grid covers the area that contains roads and buildings, the elevation of the grid becomes unreliable. Hence, to model urban flooding with consideration of buildings' block effect, the $1\text{ m} \times 1\text{ m}$ HyDSM is required.

In summary, if $1\text{ m} \times 1\text{ m}$ resolution of HyDSM can be obtained, and modeling software can handle the size of the data, then high-resolution data is preferred. However, there are cases that modeling software cannot handle high resolution and large size of data; therefore, the HyDEM is needed. When the modeling tool requires coarser resolution of data, the $1\text{ m} \times 1\text{ m}$ HyDEM can be resampled to coarser resolution HyDEM without being affected by the buildings' elevation in the data.

Materials and Methods

Acquired Data Set

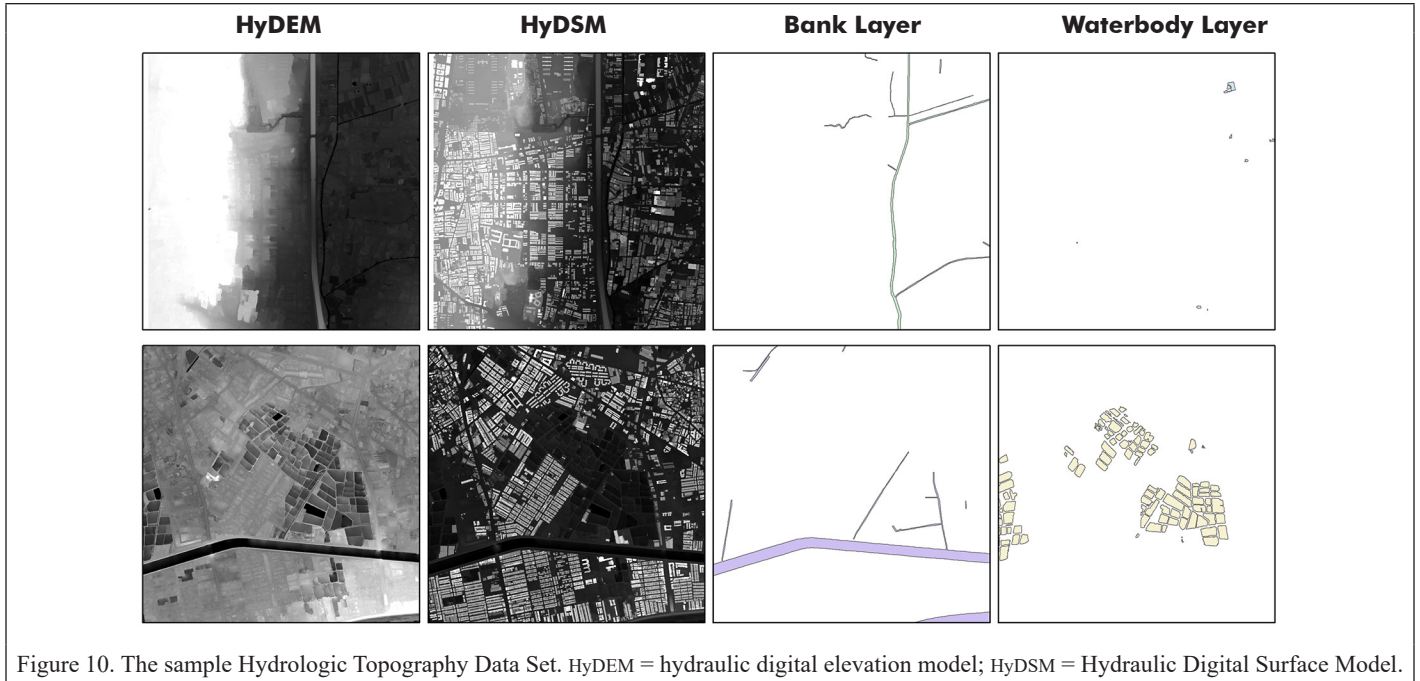
The LoSA provides digital map products of Taiwan by multiple 1:5000 scale map frames, which cover the Taiwan main island and offshore islands. Each frame covers an area of roughly 2.5 km by 2.5 km square and the area covered by these frames are mutually exclusive (Figure

9). For this study, we acquire the Hydro Topography Data Set of frame no. 94184010 and no. 94193088 from LoSA for examination. The proposed Sea-Dike Layer and Land Boundary Layer were not available in the sample data set at the time when this study is conducted; therefore, they are not discussed in this paper. The major part of frame no. 94193088 falls within the Yanshuei Drainage System, whereas the major part of frame no. 94184010 falls in the Sanyei Drainage System. Both frames are inside the Tainan City administration area.

The sample HTD is shown in Figure 10. In the HyDSM data, the building (in white to light gray color) can be clearly distinguished, whereas in HyDEM the buildings are removed. The HTD in both frames contain bank lines. Only a small portion of frame no. 94184010 has a Waterbody Line, whereas in frame no. 94193088, a couple of Waterbody Lines are derived. Most of the Waterbody Lines in frame no. 94193088 are the edge lines of inland fish farms.

The bank elevation in the Bank Layer is preserved at the edge vertices (Figure 11a).

The values of the vertices elevation can be extracted by Geographical Information System (GIS) tool such as QGIS. Figure 11b shows the bank elevation in frame no. 94193088 in well-known text (wkt) representation, which is a common data format used in various GIS software.



Data Examination Approaches

To inspect the acquired data set, the data examination approaches are designed as following modeling scenarios:

1. To examine the HyDEM data, we model a historical flood event in the domain of frame no. 94184010, using DEM and HyDEM and compare the results.
2. To examine the HyDSM data, we assume a designed rainfall-instant 0.5 m of water, drops on a circled area with diameter of 1000 meter within the domain of frame no. 94184010, and modeling the overland flow using DEM and HyDSM.
3. To examine the Bank Line data, we assume a discharge of 2 cm enter the channel at a designed location in the domain of frame no. 94193088, and model the overbank flow using different quad-tree grid specifications in 3Di model and compare the results.
4. To examine the Waterbody Line data, we compare the waterline data set of frame no. 94193088 with the satellite image, to check whether the edge of waterbody is appropriately derived from the lidar point cloud.

The hydraulic model used for data examination is 3Di, which is developed by the 3Di consortium consisting of Deltares, the Delft University of Technology, Nelen & Schuurmans consultancy, and regional water authorities, and now a commercial software owned and maintained by Nelen & Schuurmans consultancy. The flowchart of the data examination approach is shown in Figure 12.

3Di as the Modeling Tool

The 3Di model was developed by Professor Stelling from TU Delft, Netherlands in 2010 (Dahm *et al.* 2014). The 3Di model combines four numerical methods, including (1) subgrid method, (2) bottom friction based on the concepts of roughness depth, (3) staggered-grid finite-volume method for shallow water equations with rapidly varying flows, and (4) quad-tree technique (Stelling 2012). Among these numerical methods, the subgrid and quad-tree methods are designed for handling a large number of computational grids with high resolution topographic data (Meesuk 2017). 3Di's numerical model is based on finite volume scheme, which works by solving the 2D shallow water equations. By using the quad-tree method, 3Di can increase the density of computational cells in important areas where the topography is complicated and the detail of water flow process is of interest, such as urban areas, levees, and roads. A properly designed quad-tree structure in the model can ensure that the flow field to perform smoothly and reduces errors affected by the terrains.

The quad-tree method increases the flexibility of simulation cells and is efficient in terms of grid generation. By assigning breaklines of

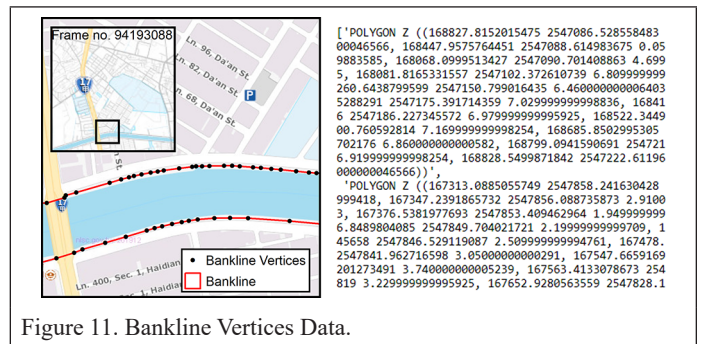


Figure 11. Bankline Vertices Data.

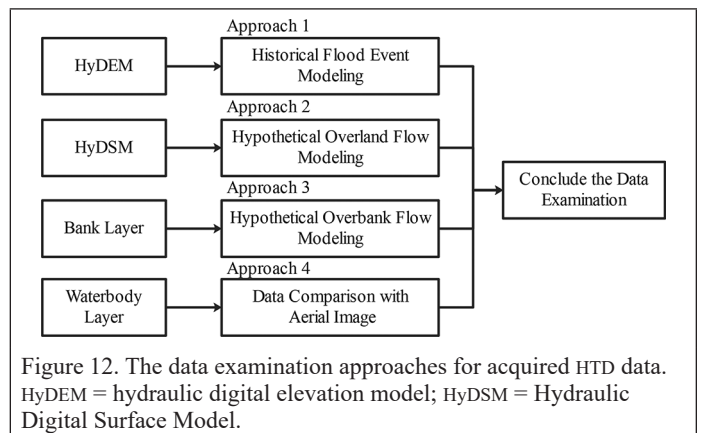
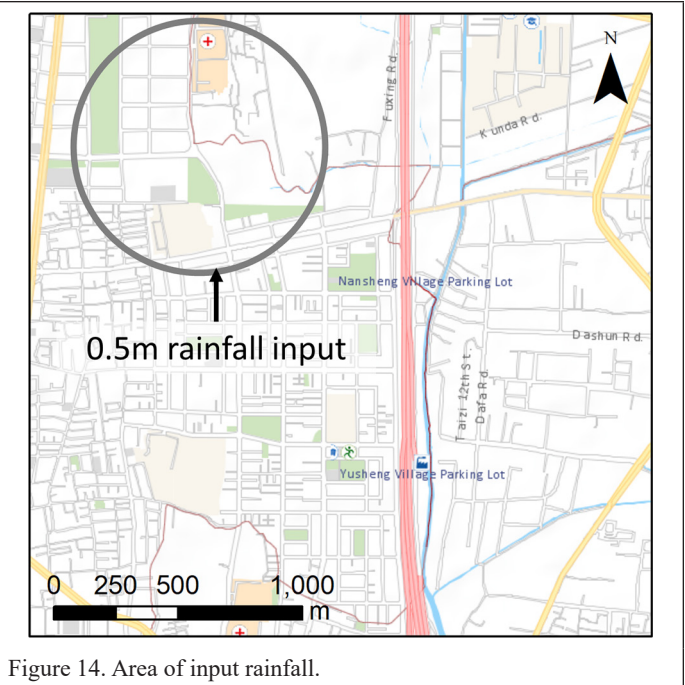
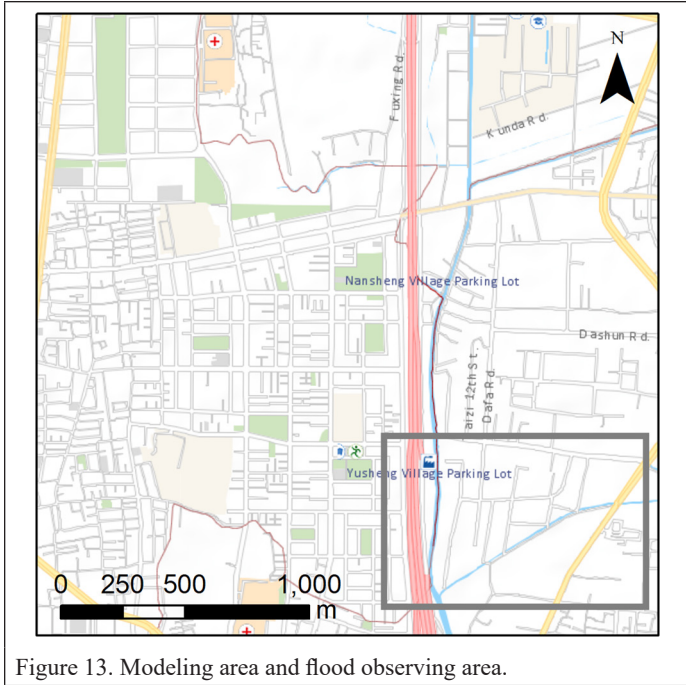


Figure 12. The data examination approaches for acquired HTD data. HyDEM = hydraulic digital elevation model; HyDSM = Hydraulic Digital Surface Model.

the terrain and associated refinement level, the simulation cells can be automatically generated for various types of terrain. On the other hand, the subgrid method generates a series of temporary tables which contain the water volume–level relationship of each simulation cell before the simulation starts. Then during the simulation, these tables serve as the link between water volume and solved water level. Thus, we can determine the change of water volume between two adjacent cells in a very computational efficient way.

Approach 1: Historical Flood Event Modeling

To investigate the utilities of HyDEM, we use a historical rainfall event at location within frame no. 94184010, and observe the resulting flooding around the marked rectangle as shown in Figure 13.



Approach 2: Hypothetical Overland Flow Modeling

To investigate the utilities of HyDSM, the overland flow modeling is implemented on the HyDSM and DEM of frame no. 94184010, to compare the difference of modeling results between HyDSM and DEM. The designed rainfall has depth of 0.5 m and diameter of 1000 m with the center located at top center of frame no. 94184010 (see Figure 14). The amount of water enters the system immediately at the beginning of the simulation, and last for 60 minutes.

Approach 3: Hypothetical Overbank Flow Modeling

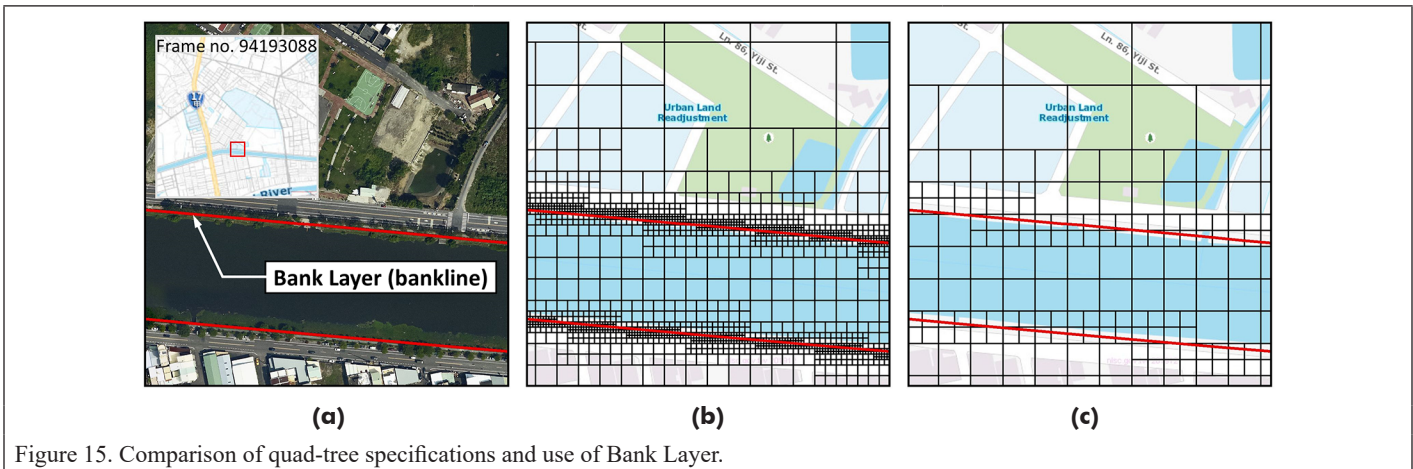
To investigate the utilities of the Bank Layer, the overbank flow modeling is implemented on the HyDEM along with the Bank Layer data in frame no. 94193088. In the simulation, the Bank Layer is used for two purposes: (1) as the Grid Refinement Line; (2) as the Levee Line, in a 3Di model. The “Grid Refinement Line” and “Levee Line” are the terminologies used in 3Di. In 3Di, the “Grid Refinement Line” is used for local quad-tree grid refinement. The quad-tree grid refinement technique allows the model to generate finer 2D quad-tree grids to calculate water flow in one area with more detail while maintaining larger quad-tree grids in other areas. The “Levee Line” is used to model the levee effect by preserving the levee (or bank) elevation in the Levee Line attributes, which is one of the 3Di model settings.

In the 3Di subgrid technique, the mechanism of flow from one quad-tree grid to the next is determined on the edge of each cell and

depends on the raster grid values along the edge. In the case that a levee with a width smaller than a quad-tree, chances are that the highest raster grid values of the levee does not align with the edge of the calculation cell; therefore, they affect the modeling results. Although the quad-tree grid refinement technique can create fine grids that improve the detail in areas where high variability of topography elevation is expected, more quad-tree grids will need more calculation resources to simulate. In this scenario, we will discuss different modeling approaches that facilitate the Refinement Line and Levee Line, to generate different resolutions of quad-tree grid, and compare the effects of grid settings on the simulation results.

- The designed modeling cases are as follows:
- Case (1): **Fine** quad-tree grids along the bankline **without** levee elevation value in the Levee Line.
 - Case (2): **Coarse** quad-tree grids along the bankline **without** levee elevation value in the Levee Line.
 - Case (3): **Coarse** quad-tree grids along the bankline **with** levee elevation value in the Levee Line.

The use of different quad-tree grids specification, and bankline elevation adjustment are illustrated in Figure 15. In Figure 15b, the Bank Layer is used as the Refinement Line for generating fine grids along the levee. The size of the finest grid is set to 2 m to ensure the elevation of bankline raster grids contains some quad-tree grids. On the



other hand, in Figure 15c, the Bank Layer is used as the Levee Line, which the bank elevation is adjusted by the z values of the vertices in the Bank Layer, for the quad-tree grids along the levee to pick up the correct height of the bank.

The location of the designed inflow is shown in Figure 16. In this modeling scenario, the discharge of 2 cm enters the system immediately at the beginning of the simulation, and last for 60 minutes.

Approach 4: Data Comparison with Aerial Images

The Waterbody Layer is inspected by comparing the aerial image of the data set in frame no. 94193088, with focus on the inland fish farms. The aerial image is taken at the same time as the lidar points is taken, therefore the accuracy of the delineated waterbody edgeline can be examined by comparing aerial photo and the vector data side by side.

Results

The HyDEM

The results of examination Approach 1 are shown in Figure 17 and Figure 18. It's seen that in Figure 17 that part of the channel is not well delineated, so that the water seems to "overflow" the channel at top-right corner in the figure. On the other hand, in Figure 18 the channel is well delineated, and the boundary between channel and land surface can be clearly distinguished, therefore during the simulation, the water is confined in the channel instead overflow the channel.

The HyDSM

The results of examination Approach 2 are shown in Figure 19 and Figure 20, which are the snapshot at 60 minutes since the beginning of the simulation. In Figure 19, it's observed that for both data sets (DEM and HyDEM), part of the water flow to the upper left of the domain, whereas part of the water flow to the east of the domain. However, for the result using DEM, the east side of the water concentrated at bottom right of the domain, whereas for the result using HyDEM, the east side of the water concentrate at upper right of the domain. A more detailed comparison is shown in Figure 20. It's observed that the inundation area is on the streets, instead of scattering around the surface. The comparison shows that the use of DEM and HyDEM leads to significantly different results, which means for 2D inundation modeling at resolution of $1\text{ m} \times 1\text{ m}$, the existence of building elevation plays an

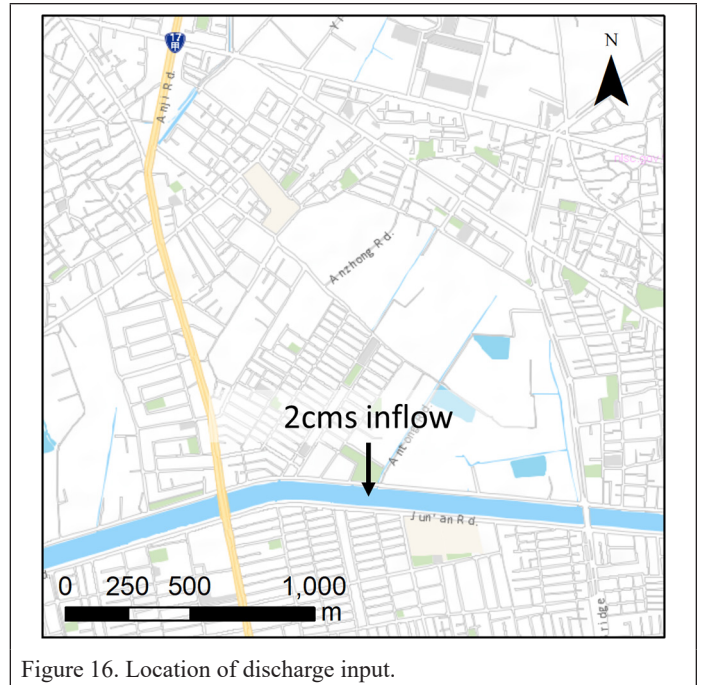


Figure 16. Location of discharge input.

important role. From physical perspective of view, DEM with elevation of buildings is a better representation of the real world. From the data examination, we can conclude that when conducting 2D urban flood modeling at resolution of $1\text{ m} \times 1\text{ m}$, HyDEM is more suitable than traditional DEM.

The Bank Layer

The results from examination Approach 3 are shown in Figure 21, which shows the snapshot of the results at 32 minutes since beginning of the simulation for the three cases that defined the "Materials and Methods" section. It's observed that the flow pattern of Case (2) is significantly different than the other two cases. In Case (2), much of the water overflow is on the south side levee and inundates almost half of the streets at south side of the domain. On the other hand, in Case (1)

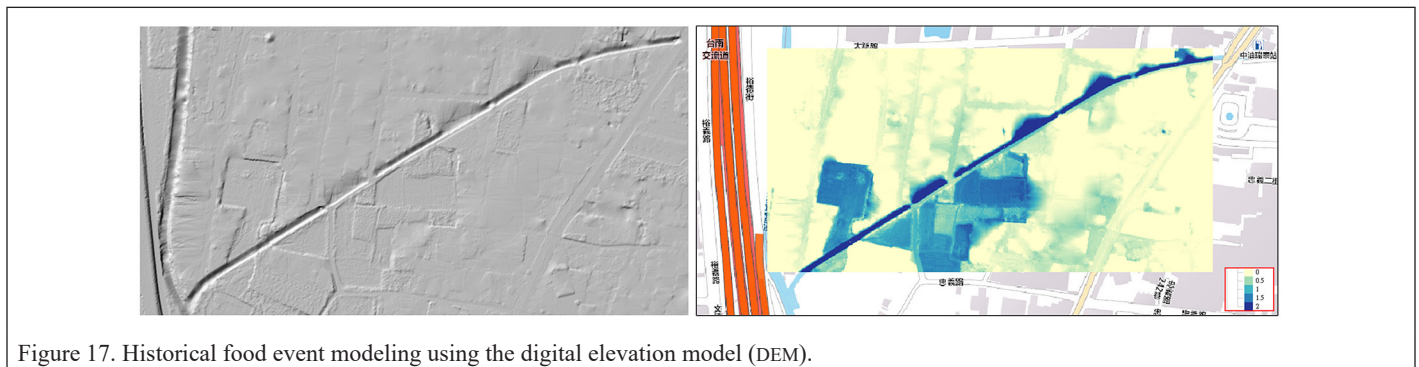


Figure 17. Historical flood event modeling using the digital elevation model (DEM).

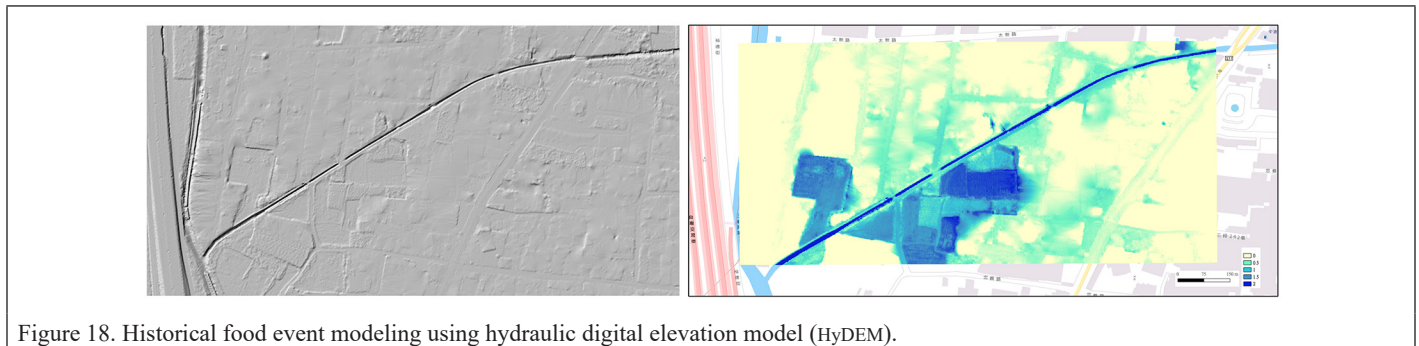


Figure 18. Historical flood event modeling using hydraulic digital elevation model (HyDEM).

201801010100

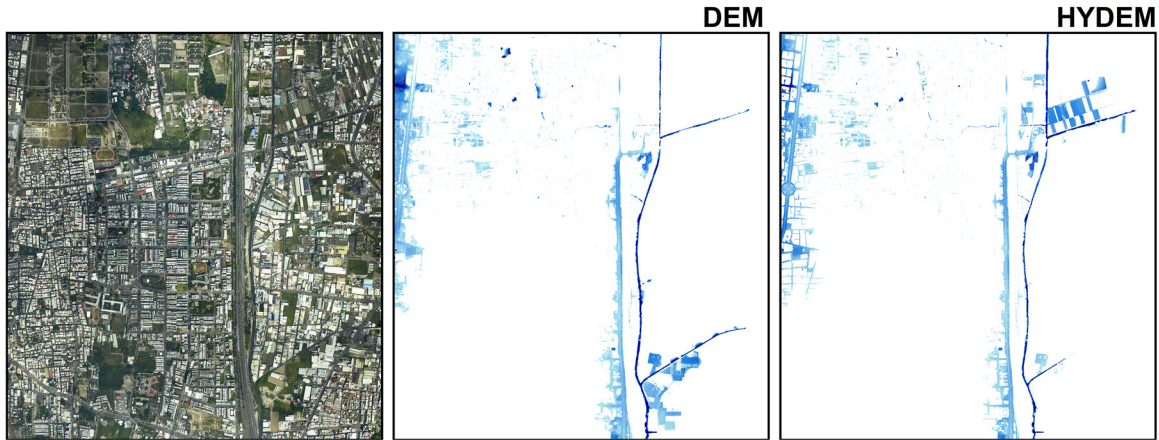


Figure 19. Comparison of the digital elevation model (DEM) and hydraulic digital elevation model (HyDEM) modeling results—large scale.

201801010100

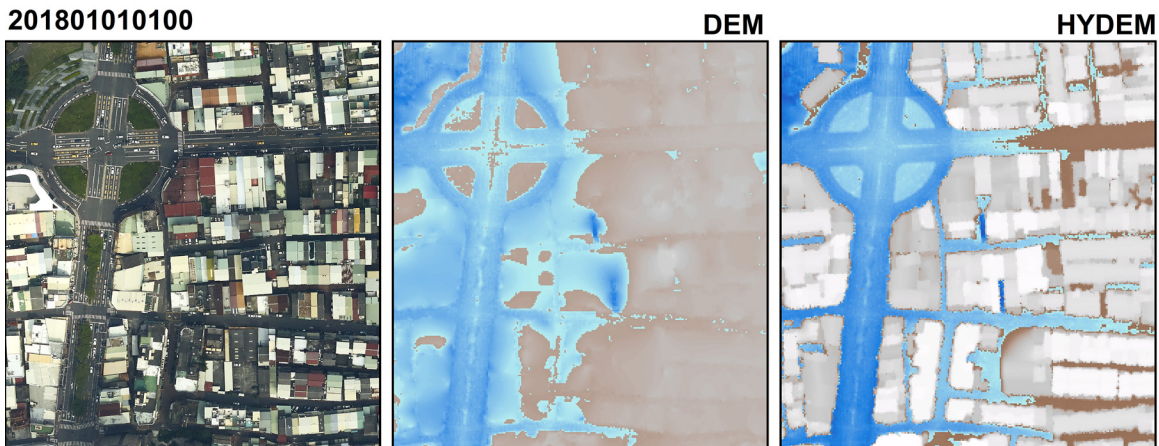
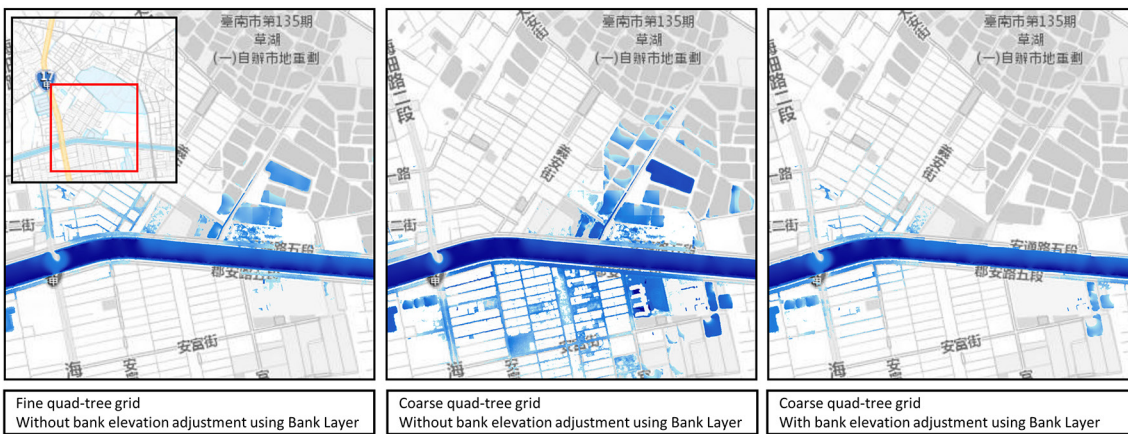


Figure 20. Comparison of the digital elevation model (DEM) and hydraulic digital elevation model (HyDEM) modeling results—small scale.

0 250 500 1,000
Meters



Case (1)

Case (2)

Case (3)

Figure 21. Comparison of modeling results from different quad-tree configurations and the digital elevation model (DEM).

and Case (3), water overflow on the south side levee at west and east side of the domain, while in Case (1), water overflow the north side levee at location near the middle section of the channel, but in Case (2) not much water overflow is at the same location.

The comparison of the flow pattern of the three cases shows that flow patterns in Case (1) and Case (3) are similar. The waterflow pattern in Case (2) is different than the others because using coarse grids

without adjustment of levee elevation makes the model fail to simulate the effect of obstacle for water flow. Another difference of the three cases is the calculation time. As illustrated in Figure 15, to match the scale of the levee width, the quad-tree grid size is set to 2 m, which significantly increases the number of grids; hence it requires more time for calculation. For the three cases, the number of calculation cells is 21 593, 2949, and 2949, respectively, and the corresponding

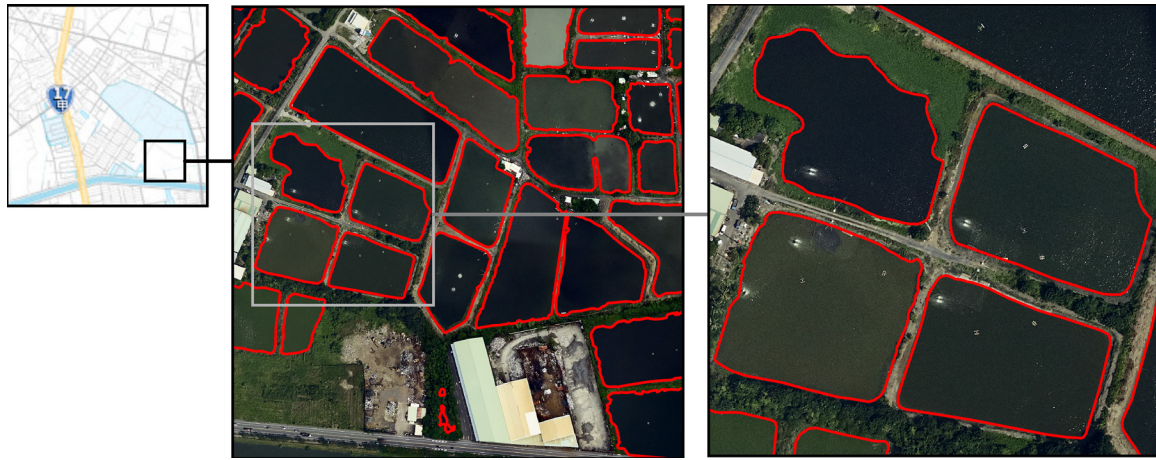


Figure 22. Waterbody Edgeline examples.

computation time using a PC with six core CPU and 32 GB ram, are approximately 4 minutes 30 seconds, 30 seconds, and 30 seconds, respectively (see Table 2). The ratio of computation time for fine grids and coarse grids are approximate 9:1. From the data examination we can conclude that the use of 3D bankline can enhance the quality of 2D flood modeling, as it can be used to create fine quad-tree grids at locations with high elevation variation. Moreover, the elevation of vertices in the 3D Bankline allows the model to simulation the effect of obstacles even using coarse quad-tree grids.

The Waterbody Layer

The results from examination Approach 4 are shown in Figure 22. The comparison of aerial image and the acquired Waterbody Edgeline data shows that the Waterbody Edgeline aligns with the edge of waterbody with high accuracy. With the high accuracy, the Waterline data set is suitable for defining the area of waterbody and used for DEM replacement when the elevation in the original data set is not correct.

Discussion

Based on the preliminary discussion, a sample of HTD is created and provided by LoSA upon request. For each of the data in the HTD, we apply different modeling scenarios to examine the utilities of the proposed HTD. The examination results show that the three data sets provide their functionalities to improve the quality of 2D flood modeling. In the overland flow scenario, water flow is limited on the streets instead of scattering around a land surface without being obstructed, which is not physically realistic, since buildings do exit and affect the flow of water. In the overbank scenario, the Bank Layer serves for two purposes: as a “Refinement Line” or a “Levee Line”. The Refinement Line is for the model to generate fine mesh grids along the levee, whereas the Levee Line is for the model to preserve the elevation of the dike during modeling when the quad-tree grids are larger than the width of a levee.

In the data comparison scenario, the acquired Waterbody Layer is compared with aerial images and the result indicates the waterbody edges in the aerial image align well with the Waterbody Edgeline data. It can be argued that in data examination Approach 2, there are still difference between Case (1) and Case (2). Although the approaches of using finer quad-tree grids and using the Bank Layer as the Levee Line both seek to preserve the elevation of the levee in the simulation, the differences are due to that they are different numerical representations. The grid refinement approach creates fine quad-tree grids along the levee. As long as the quad-tree grid size is smaller than the raster size of the levee, the elevation of the levee can be catch by the grid. On the other hand, the in the Levee Line approach, only a value represents the elevation of a levee segment between two vertices. In other words, one levee segment can only have one elevation value. This is usually not correct when a levee segment is much longer than the DEM grid size, and the elevation of the DEM varies along the levee.

Table 2. Tabulated modeling results based on different quad-tree configurations.

Case No.	Model Configuration	No. of Quad-Tree Grids	Computation Time
Case (1)	Fine quad-tree grids	21 593	4 min 30 sec
	Without bank elevation adjustment using Bank Layer		
Case (2)	Coarse quad-tree grids	2949	30 sec
	Without bank elevation adjustment using Bank Layer		
Case (3)	Coarse quad-tree grids With bank elevation adjustment using Bank Layer	2949	30 sec

If the correctness of numerical representation in the model is considered, the quad-tree grid refinement approach is the best approach for model setting. However, if the computation time is the concern, the Levee Line approach is the better choice.

The error caused by the Levee Line can be adjusted by creating Bank Layer with more vertices distributed on the edge. This study aims to investigate the need and the format of the HTD as specific data set for high resolution 2D urban flood modeling. However, the discussion, based on designed data examination approaches, are limited because of the following reasons: (1) Due to the data availability, this study uses data sets within the 1:5000 scale, 2.5 km × 2.5 km map frame, instead of a complete drainage area; (2) The models are not calibrated and validated by real event data; (3) The data examination processes only use one software package for modeling, which is lack of variability; (4) In this study, we only use pure 2D modeling for data examination. However, 1D–2D coupling modeling is also commonly implemented in modern applications. (5) The proposed Sea-Dike Layer and Land Boundary Layer were not available in the sample data set when we acquired the data; therefore, their usability cannot be investigated within this paper. For further investigation and more complete discussions on the use and format of HTD. We suggest using complete HTD data set and modeling a complete drainage area and use real events data for model calibration and validation. Furthermore, conducting modeling using different software packages and considering 1D–2D coupling can also help us understand the pros and cons of the proposed data format.

Conclusion

The purpose of this paper is to discuss and investigate the Hydrological Topography Data Set (HTD) for high resolution urban flood modeling. The HTD comprises three types of data: (1) High Resolution Hydraulic 3D Features; (2) Hydraulic DEM (HyDEM); and (3) Hydraulic DSM (HyDSM). High Resolution Hydraulic 3D Features are high resolution,

three-dimensional vector data that preserve the locations and elevations of topography breaklines. HyDEM is high resolution (1 m × 1 m) DEM enhanced by the topography breaklines to preserve the landscape characteristics, and HyDSM is high resolution (1 m × 1 m) DSM conditioned by removing the height of vegetation and temporary objects, also enhanced by the topography breaklines to preserve the landscape characteristics.

From the data examination results we conclude that:

- (1) HyDEM performs better than DEM in 2D flood modeling when using HyDEM topography breaklines to enhance the raster grid, which preserves the shape and elevation of some landscape characteristics such as channel bank elevation.
- (2) HyDSM is a better representation of the topography for 2D modeling at resolution of 1 m × 1 m, because in such resolution the phenomenon of water flow being blocked by buildings during a flood event can be modeled.
- (3) Bank Layer provides spatial information (i.e., the 2D location and elevation at vertices of a riverbank) for the model to generate fine calculation cells along the levee, or to preserve the levee elevation when using coarse calculation cell for simulation. The two approaches both intend to model the effect of the levee on water flow; however, in the latter case, the computation time can be significantly reduced.
- (4) The Waterbody Layer can be used to replace elevation data within the area of a waterbody, which is useful when the elevation in a waterbody is not correct or when data is missing.

For further investigation of the HTD, we suggest: (1) testing all the proposed HTD data in hydraulic modeling; (2) using a complete drainage area for modeling; (3) using a more complicated model such as 1D–2D coupling models; and (4) using different numerical models to explore the data set's performance in different implementations.

References

- Afiñ, Z., H.-J. Chu, Y.-L. Kuo, Y.-C. Hsu, H.-K. Wong and M. Zeeshan Ali. 2019. Residential flood loss assessment and risk mapping from high-resolution simulation. *Water* 11(4):751.
- Alivio, M.B.T., G. R. Puno and B.A.M. Talisay. 2017. Flood hazard zones using 2D hydrodynamic modeling and remote sensing approaches. *Global Journal of Environmental Science and Management*. <https://doi.org/10.22034/gjesm.2019.01.01>.
- Al-Suhili, R., C. Cullen and R. Khanbilvardi. 2019. An urban flash flood alert tool for megacities—Application for Manhattan, New York City, USA. *Hydrology* 6(2):56.
- Annis, A., F. Nardi, A. Petroselli, C. Apollonio, E. Arcangeletti, F. Tauro, C. Belli, R. Bianconi and S. Grimaldi. 2020. UAV-DEMs for small-scale flood hazard mapping. *Water* 12:1717.
- Bodoque, J., C. Guardiola-Albert, E. Aroca-Jiménez, M. Eguibar and M. Martínez-Chenoll. 2016. Flood damage analysis: First floor elevation uncertainty resulting from LiDAR-derived digital surface models. *Remote Sensing* 8(7):604.
- Bove, G., A. Becker, B. Sweeney, M. Voudoukas and S. Kulp. 2020. A method for regional estimation of climate change exposure of coastal infrastructure: Case of USVI and the influence of digital elevation models on assessments. *Science of the Total Environment* 710:136162.
- Brugelmann, R. 2000. Automatic breakline detection from airborne laser range data. *International Archives of Photogrammetry and Remote Sensing XXXIII(B3):109–116*.
- Dahm, R., C.-T. Hsu, H.-C. Lien, C.-H. Chang and G. Prinsen. 2014. Next generation flood modelling using 3Di: A case study in Taiwan. *Proceedings DSD International Conference*, held in Hong Kong, China, Nov. 2014.
- Dhungel, S., M. E. Barber and R. L. Mahler. 2019. Comparison of one- and two-dimensional flood modeling in urban environments. *International Journal of Sustainable Development and Planning* 14:356–366.
- Ding, Q., Z. Shao, X. Huang, O. Altan and B. Hu. 2021. Monitoring, analyzing and predicting urban surface subsidence: A case study of Wuhan City, China. *International Journal of Applied Earth Observation and Geoinformation* 102(6).
- Hingee, K. L., P. Caccetta and L. Caccetta. 2019. Modelling discontinuous terrain from DSMs using segment labelling, outlier removal and thin-plate splines. *ISPRS Journal of Photogrammetry and Remote Sensing* 155:159–171.
- Kain, C. L., B. Lewarn, E. H. Rigby and C. Mazengarb. 2019. Tsunami inundation and maritime hazard modelling for a maximum credible tsunami scenario in southeast Tasmania, Australia. *Pure and Applied Geophysics* 177:1549–1568.
- Kenny, F. and B. Matthews. 2005. A methodology for aligning raster flow direction data with photogrammetrically mapped hydrology. *Computers and Geosciences* 31:768–779.
- Kenny, F., B. Matthews and K. Todd. 2008. Routing overland flow through sinks and flats in interpolated raster terrain surfaces. *Computers and Geosciences* 34:1417–1430.
- Kurniyaningrum, E., L. M. Limantara, E. Suhartanto and D. Sisinggih. 2019. Sensitivity of flow depth inundation based on the micro-scale topography in Krukut River, Jakarta, Indonesia. *International Journal of Civil Engineering and Technology* 10(1):697–706.
- Li, J., K. K. Lai and P. Safonov. 2019. Estimation method of inundation extent based on mathematical morphology. *Mathematical Problems in Engineering* 2019:1–10.
- Liu, X. 2008. Airborne LiDAR for DEM generation: Some critical issues. *Progress in Physical Geography: Earth and Environment* 32:31–49.
- Liu, X. and Z. Zhang. 2013. Effects of LiDAR data reduction and breaklines on the accuracy of digital elevation model. *Survey Review* 43:614–628.
- Luppichini, M., M. Favalli, I. Isola, L. Nannipieri, R. Giannecchini and M. Bini. 2019. Influence of topographic resolution and accuracy on hydraulic channel flow simulations: Case study of the Versilia River (Italy). *Remote Sensing* 11.
- Medeiros, S. C., T. Ali, S. C. Hagen and J. P. Raiford. 2011. Development of a seamless topographic/bathymetric digital terrain model for Tampa Bay, Florida. *Photogrammetric Engineering and Remote Sensing* 77(2011):1249–1256.
- Meesuk, V. 2017. *Point Cloud Data Fusion for Enhancing 2D Urban Flood Modelling*. London: CRC Press, 270p.
- O'Callaghan, J. F. and D. M. Mark. 1987. The extraction of drainage networks from digital elevation data. *Computer Vision, Graphics, and Image Processing* 28:323–344.
- Pinos, J., L. Timbe and E. Timbe. 2019. Evaluation of 1D hydraulic models for the simulation of mountain fluvial floods. *Water Practice and Technology* 14:341–354.
- Rong, Y., T. Zhang, Y. Zheng, C. Hu, L. Peng and P. Feng. 2020. Three-dimensional urban flood inundation simulation based on digital aerial photogrammetry. *Journal of Hydrology* 584.
- Rutzinger, M., B. Höfle and K. Kringer. 2016. Accuracy of automatically extracted geomorphological breaklines from airborne lidar curvature images. *Geografiska Annaler: Series A, Physical Geography* 94:33–42.
- Scarlatos, L. L. 1989. A compact terrain model based on critical topographic features. <https://citeseerx.ist.psu.edu/viewdoc/download?doi=10.1.1.566.2204&rep=rep1&type=pdf>.
- Shao, Z., H. Fu, D. Li, O. Altan and B. Hu. 2019. Remote sensing monitoring of multi-scale watersheds impermeability for urban hydrological evaluation. *Remote Sensing of Environment*, 232.
- Shao, Z., Y. Li, X. Huang, B. Cai and Y. Zhang. 2021. Monitoring urban ecosystem service value using dynamic multi-level grids. *arXiv:2104.09307*.
- Shen, J. 2020. Influence of uncertainties in DEM resolution and surface friction to the building treatment methods in urban inundation modelling. *IOP Conference Series: Earth and Environmental Science* 428.
- Sholichin, M. and W. Qadri. 2020. Predicting flood hazards area using SWAT and HEC-RAS simulation in Bila River, South Sulawesi. *IOP Conference Series: Earth and Environmental Science* 437.
- Stelling, G. S. 2012. Quadtree flood simulations with sub-grid digital elevation models. *Proceedings of the Institution of Civil Engineers* 165:567–580. <https://doi.org/10.1680/wama.12.00018>.
- Yang, B., R. Huang, Z. Dong, Y. Zang and J. Li. 2016. Two-step adaptive extraction method for ground points and breaklines from lidar point clouds. *ISPRS Journal of Photogrammetry and Remote Sensing* 119:373–389.
- Zhang, H., X. Cheng, L. Jin, D. Zhao, T. Feng and K. Zheng. 2020. A method for dynamical sub-watershed delimitating by no-fill digital elevation model and defined precipitation: A case study of Wuhan, China. *Water-Sui* 12 (2), 486. <https://doi.org/10.3390/w12020486>.

Improving Land Cover Classification over a Large Coastal City Through Stacked Generalization with Filtered Training Samples

Feilin Lai and Xiaojun Yang

Abstract

To improve remote sensing-based land cover mapping over heterogeneous landscapes, we developed an ensemble classifier based on stacked generalization with a new training sample refinement technique for the combiner. Specifically, a group of individual classifiers were identified and trained to derive land cover information from a satellite image covering a large complex coastal city. The mapping accuracy was quantitatively assessed with an independent reference data set, and several class probability measures were derived for each classifier. Meanwhile, various subsets were derived from the original training data set using the times of being correctly labeled by the individual classifiers as the thresholds, which were further used to train a random forest model as the combiner in generating the final class predictions. While outperforming each individual classifier, the combiner performed better when using the class probabilities rather than the class predictions as the meta-feature layers and performed significantly better when trained with a carefully selected subset rather than with the entire sample set. The novelties of this work are with the insight into the impact of different training sample subsets on the performance of stacked generalization and the filtering technique developed to prepare training samples for the combiner leading to a large accuracy improvement.

Introduction

Research Background

While the importance of land cover information for environmental sustainability and the role of remote sensing in deriving this critical information have been discussed elsewhere (e.g., Turner *et al.* 2007; Wulder *et al.* 2018), the remote sensing community has been enthusiastic in developing different strategies and methodologies towards thematic mapping accuracy improvement (e.g., Zhu *et al.* 2019). While comprehensive reviews on the progress of the subject can be found elsewhere (e.g., Khatami *et al.* 2016), this research focuses on ensemble classification, which has rapidly gained the popularity in pattern recognition and machine learning communities (Ho *et al.* 1994; Ho 2000; Jain *et al.* 2000; Ranawana and Palade 2006; Wozniak *et al.* 2014; Shi and Yang 2017a).

Ensemble classification can potentially achieve high performance in pattern recognition due to the capability of capturing diverse characteristics of a feature space when using a combination of classifiers with different feature descriptors and classification procedures simultaneously (Xu *et al.* 1992). Moreover, it can flexibly deal with multisensor data, multifeature extraction, and multiple algorithm fusion (Benediktsson *et al.* 2007), which may be critical for complex scenarios like heterogeneous landscape mapping (e.g., Zhu *et al.* 2019). Nevertheless, the success of a classifier ensemble method depends upon not only the individual classifiers and the combination techniques but also other factors such as input data, feature attributes, and training

data (Dara 2007). Current efforts made by the remote sensing community, however, have been overly unbalanced with the overwhelming attention on the two major issues, i.e., the selection of individual classifiers and the design of various combination methods (e.g., Pal 2008; Du *et al.* 2012; Shi and Yang 2017a; Bian *et al.* 2019).

There have been some classifier ensemble methods proposed over the years (see Jain *et al.* 2000; Wozniak *et al.* 2014), most of which can fall within either cascading, parallel, or hierarchical in terms of the topology (Lu 1996). Note that ensemble learning methods, such as bagging, boosting, and random forests (e.g., Chan *et al.* 2001) are considered as single classifiers rather than the ensemble results of multiple classifiers (Jain *et al.* 2000). In the cascading topology, individual classifiers are sequentially invoked to reduce the number of possible identities for the input data so that the decision can gradually become more focused. The major drawback is that later classifiers are not able to correct the errors from earlier classification. In the parallel topology, individual classifiers are executed independently, and their results are combined through different methods ranging from simple ones, such as majority voting, to complex ones, such as weighted average and logarithmic regression. The hierarchical topology uses a tree-like structure combining cascading and parallel configurations to obtain the optimal performance (Ranawana and Palade 2006). Despite the rich pool of topologies, most of the classifier ensemble methods developed for task-specific applications have been structured in the parallel topology (Wozniak *et al.* 2014).

There have been some efforts modifying the classic cascading topology towards improving the performance of remote sensor image classification. For example, Waske and Benediktsson (2007) proposed a modified cascading topology by executing a support vector machine (SVM) classification over the two maps generated by an SVM from synthetic aperture radar (SAR) and optical multispectral data, respectively. Their method outperformed a single SVM model with the input from the fusion of SAR and optical data and the parallel combination of the SVM output from each data set through majority vote or absolute maximum. Du *et al.* (2012) proposed a topology by conducting a SVM classification over a set of class probability layers generated by multilayer perceptron (MLP) neural networks, SVM, radial basis function neural networks, decision tree, and minimum Mahalanobis distance from a very-high-resolution multispectral image. Their method outperformed the parallel combination using strategies such as Bayesian average, logarithmic consensus, linear consensus, majority vote, evidence theory, or fuzzy integral, although the latter included a slightly different set of individual classifiers. Chen *et al.* (2017) designed a classifier ensemble topology with a boosted classifier as the combiner of the land cover maps derived from medium-resolution satellite images using three individual classifiers, i.e., SVM, C4.5 decision tree, and MLP neural networks. Their method surpassed the three individual classifiers in terms of the thematic accuracy.

Department of Geography, Florida State University, Tallahassee, FL 32306 (xyang@fsu.edu).

Contributed by Filiz Sunar, June 14, 2021 (sent for review August 30, 2021; reviewed by Ali Ozgun Ok, Timothy A Warner, Taskin Kavzoglu).

Photogrammetric Engineering & Remote Sensing
Vol. 88, No. 7, July 2022, pp. 451–459.

0099-1112/22/451–459

© 2022 American Society for Photogrammetry
and Remote Sensing

doi: 10.14358/PERS.21-00035R3

**PEER-REVIEWED CONTENT
IS ONLY AVAILABLE TO
ASPRS MEMBERS AND SUBSCRIBERS**

**FOR MORE INFORMATION VISIT
MY.ASPRS.ORG**

**PEER-REVIEWED CONTENT
IS ONLY AVAILABLE TO
ASPRS MEMBERS AND SUBSCRIBERS**

**FOR MORE INFORMATION VISIT
MY.ASPRS.ORG**

**PEER-REVIEWED CONTENT
IS ONLY AVAILABLE TO
ASPRS MEMBERS AND SUBSCRIBERS**

**FOR MORE INFORMATION VISIT
MY.ASPRS.ORG**

**PEER-REVIEWED CONTENT
IS ONLY AVAILABLE TO
ASPRS MEMBERS AND SUBSCRIBERS**

**FOR MORE INFORMATION VISIT
MY.ASPRS.ORG**

**PEER-REVIEWED CONTENT
IS ONLY AVAILABLE TO
ASPRS MEMBERS AND SUBSCRIBERS**

**FOR MORE INFORMATION VISIT
MY.ASPRS.ORG**

**PEER-REVIEWED CONTENT
IS ONLY AVAILABLE TO
ASPRS MEMBERS AND SUBSCRIBERS**

**FOR MORE INFORMATION VISIT
MY.ASPRS.ORG**

**PEER-REVIEWED CONTENT
IS ONLY AVAILABLE TO
ASPRS MEMBERS AND SUBSCRIBERS**

**FOR MORE INFORMATION VISIT
MY.ASPRS.ORG**

**PEER-REVIEWED CONTENT
IS ONLY AVAILABLE TO
ASPRS MEMBERS AND SUBSCRIBERS**

**FOR MORE INFORMATION VISIT
MY.ASPRS.ORG**

IN-PRESS ARTICLES

- Yaping Zhang, Nan Yang, and Qian Luo. A Matching Optimization Algorithm About Low-Altitude Remote Sensing Images Based on Geometrical Constraint and Convolutional Neural Network.
- Aus Najim, Jwan Al-Doski, Faez M. Hassan, Hussein Abdelwahab Mossa. Incorporation of Digital Elevation Model, Normalized Difference Vegetation Index and Landsat 8 Data for Land Use Land Cover Mapping.
- Heqing Zhang, Zhenxin Wang, Jun-feng Song, and Xueyan Li. Transformer for the Building Segmentation of Urban Remote Sensing.
- Zhihua Zhang, Xiaowen Wu, Yikun Li, Kun Yan, Fan Zhang, Shuwen Yang, and Jun Yang. Monitoring Environment Transformation along the BTIC Railway Based on Remote Sensing by utilizing the R-RSEL.
- Wang Yue, Changgang Yu, A. Antonidoss, and Anbarasan M. Deep learning-based monitoring sustainable decision support system for energy building to smart cities with Remote Sensing Techniques.
- Ya Zhang, Zhenfeng Shao, Xiao Huang, Xiaoxiao Feng, Zifan Zhou, and Yong Li. Impact of spatial configuration of urban green space and urban impervious surface on land surface temperature: a multi-grid perspective.
- Seyed Mohammad Ayazi and Mohammad SaadatSeresht. A Boundary-Based Ground Point Filtering Method for Photogrammetric Point Cloud Data.
- Xiaohua Li, Hao Chen, Jiliu Zhou, Yuan Wang. TPPI: A Novel Network Framework and Model for Efficient Hyperspectral Image Classification.
- Weiwei Liu. Managing earth hazards using deep reinforcement learning algorithm for industrial IoT network.
- Tingting He, Youke Wang, and Zhipeng Shi. The Effect of Mulching Films on the Temporal and Spatial Distribution of Soil Water in Semiarid Hilly Area.
- Bhaskar Dubey, B. Kartikeyan. A novel residual attitude estimation approach using georeferenced satellite imagery.
- Edmond Lo, En-Kai Lin, Velautham Daksiya, Kuo-Shih Shao, Yi-Rung Chuang, Tso-Chien Pan. Efficient Building Inventory Extraction from Satellite Imagery for Megacities.
- Fei Yang, Jun Li, Tianyu Guo, Chengye Zhang, Xiao Sang. The fractional vegetation cover (FVC) and associated driving factors modelling in mining areas.
- Junyuan Yao, Shuanggen Jin. Long-term changes of Land use and land cover in the Yangtze River Basin from 1990-2020 Landsat data.

Evaluation of Urban Vegetation Phenology Using 250 m MODIS Vegetation Indices

Hongxin Zhang, Xiaoyue Wang, and Dailiang Peng

Abstract

The dynamics of urban vegetation phenology play an important role in influencing human activities. Previous studies have shown high-resolution remote sensing as a tool for urban vegetation mapping, but the low temporal resolution of these data limits their use for phenological modeling. Therefore, it is of great significance to evaluate Moderate Resolution Imaging Spectroradiometer (MODIS) imagery for urban vegetation phenology monitoring. Here, we extracted the start and end of growing season (SOS and EOS) in urban ecosystems based on both the Normalized Difference Vegetation Index (NDVI) and the Enhanced Vegetation Index (EVI) from the 250 m MODIS vegetation indices product (MOD13Q1). Then the accuracies of the satellite-derived SOS and EOS were evaluated through comparing phenological observations at 18 ground sites. Results showed that SOS was most consistent with the prime of leaf unfolding date and EOS was most consistent with the beginning of leaf coloring date. Overall, EVI was found to have stronger predictive strength than NDVI in detecting urban vegetation phenology in terms of both higher correlation coefficients and lower root-mean-square errors. In addition, the dynamic threshold method was more accurate in deriving SOS, while the double logistic method had relatively higher accuracy in deriving EOS.

Introduction

Vegetation is an important link in ecosystems because it plays a significant role in regulating climate, surface radiation balance, carbon budget, and emissions by virtue of its own characteristics (Piao *et al.* 2008; Wan and Gao 2020). By 2050, more than half of the world's population will live in urban areas, and many cities in Asia and Africa are already vulnerable to climate change and hazards caused by urbanization (Ding *et al.* 2021; Kabano *et al.* 2021; Tang *et al.* 2021). Urban vegetation, which is the ecological guarantee of the urban environment, effectively alleviates the urban heat island effect (Li *et al.* 2019a) and regulates the local climate (Clinton and Gong 2013; Cong *et al.* 2012; Qiu *et al.* 2020; Wang *et al.* 2020). The urban environment is regarded as a natural laboratory for understanding the impact of global future climate warming and related factors (i.e., atmospheric carbon dioxide (CO₂) and nitrogen (N) deposition, human activities, light pollution) on vegetation phenology (Guo *et al.* 2021; Jia *et al.* 2018; Yao *et al.* 2019). Studies on urban phenology can be used for the assessment of global warming impacts on phenology due to the urban heat island effect

Hongxin Zhang is with the Hebei Technology Innovation Center for Remote Sensing Identification of Environmental Change, Shijiazhuang 050024, China; and the College of Geographical Sciences, Hebei Normal University, Shijiazhuang 050024, China.

Xiaoyue Wang is with the Key Laboratory of Land Surface Pattern and Simulation, Institute of Geographic Sciences and Natural Resources Research, Chinese Academy of Sciences, Beijing 100101, China; and the University of the Chinese Academy of Sciences, Beijing 100049, China (wangxy@igsnrr.ac.cn).

Dailiang Peng is with the Key Laboratory of Digital Earth Science, Aerospace Information Research Institute, Chinese Academy of Sciences, Beijing 100094, China.

Contributed by Zhenfeng Shao, August 7, 2021 (sent for review October 8, 2021; reviewed by Linjing Zhang, Nan Yang).

(Jochner and Menzel 2015). Furthermore, the change in urban vegetation phenology affects the start and duration of the pollen season in urban domains, which has become a major influence on public health due to the potential risks of pollen-induced respiratory allergies (e.g., asthma) (Li *et al.* 2017b; Li *et al.* 2019b). Therefore, with the acceleration of urbanization, studying the changes in urban vegetation phenology will provide a decision-making basis for relevant departments in urban planning and design and public health safety management.

Remote sensing technology provides an efficient way to monitor seasonal changes in terrestrial vegetation on a regional to global scale using satellite-mounted synoptic sensors (Wu *et al.* 2016; Wu *et al.* 2017). Different types of remote sensing data and vegetation indices were used to determine the phenological phases of vegetation (e.g., start of growing season (SOS), end of growing season (EOS)) through different phenological identification methods for the large-scale research area (Cong *et al.* 2012; Helman 2018; Kosmala *et al.* 2016; Piao *et al.* 2006; Yang *et al.* 2019). Moreover, some studies have shown that the random combination of different types of remote sensing data and algorithms will lead to various phenological results (Fisher and Mustard 2007; Hou *et al.* 2014; Misra *et al.* 2016; Peng *et al.* 2021; Piao *et al.* 2019; Studer *et al.* 2007; Wu *et al.* 2014; Zhang *et al.* 2018). Previous studies found that the SOS dates estimated from different methods show similar spatial patterns along latitudinal or altitudinal gradients but with significant variances in the data (Cong *et al.* 2012; Ding *et al.* 2015). In addition, the regional mean satellite-derived growing season clearly started earlier and terminated slightly later than the regional mean ground-based growing season in China (Chen *et al.* 2013).

Ground phenology data are often used to evaluate the accuracy of vegetation phenology, which is extracted by remote sensing data. However, the validation of remote sensing-based urban vegetation phenology has not been well documented. In addition, ground observations usually record a series of specific events during the growing season, such as leaf-out, flowering, leaf coloring, etc. Nevertheless, which event is the best indicator to validate remote sensing-based SOS and EOS of urban vegetation has not been well investigated. To date, most studies have focused on the spatiotemporal variation in urban vegetation and its influencing factors. For example, Li *et al.* (2020) used Landsat Thematic Mapper (TM) to study the impact of urbanization and climate change on urban vegetation dynamics in China and concluded that the contribution of urbanization to vegetation in urban fringe areas is greater than that in urban core areas, while the contribution of climate change to vegetation in urban core areas is greater. Zipper *et al.* (2016) found that the effect of urban heat islands on vegetation phenology was related to land cover composition. Liang *et al.* (2016) used MOD13A2 to analyze the relationship between urban SOS and land surface temperature (LST), precipitation, and sunshine duration in middle temperate cities of China and found that the spatial differences of temperature and altitude will lead to spatial heterogeneity of urban SOS. Zhang *et al.* (2021) explored the response of vegetation phenology to urbanization in Beijing and found that the change rates of vegetation phenology in urban areas were 1.3 and 1.1 days per year

Photogrammetric Engineering & Remote Sensing
Vol. 88, No. 7, July 2022, pp. 461–467.

0099-1112/22/461-467
© 2022 American Society for Photogrammetry
and Remote Sensing
doi: 10.14358/PERS.21-00049R3

**PEER-REVIEWED CONTENT
IS ONLY AVAILABLE TO
ASPRS MEMBERS AND SUBSCRIBERS**

**FOR MORE INFORMATION VISIT
MY.ASPRS.ORG**

**PEER-REVIEWED CONTENT
IS ONLY AVAILABLE TO
ASPRS MEMBERS AND SUBSCRIBERS**

**FOR MORE INFORMATION VISIT
MY.ASPRS.ORG**

**PEER-REVIEWED CONTENT
IS ONLY AVAILABLE TO
ASPRS MEMBERS AND SUBSCRIBERS**

**FOR MORE INFORMATION VISIT
MY.ASPRS.ORG**

**PEER-REVIEWED CONTENT
IS ONLY AVAILABLE TO
ASPRS MEMBERS AND SUBSCRIBERS**

**FOR MORE INFORMATION VISIT
MY.ASPRS.ORG**

**PEER-REVIEWED CONTENT
IS ONLY AVAILABLE TO
ASPRS MEMBERS AND SUBSCRIBERS**

**FOR MORE INFORMATION VISIT
MY.ASPRS.ORG**

**PEER-REVIEWED CONTENT
IS ONLY AVAILABLE TO
ASPRS MEMBERS AND SUBSCRIBERS**

**FOR MORE INFORMATION VISIT
MY.ASPRS.ORG**



ASPRS AERIAL DATA CATALOG

“THE SOURCE FOR FINDING AERIAL COLLECTIONS”

[HTTP://DPAC.ASPRS.ORG](http://dpac.asprs.org)

The ASPRS Aerial Data Catalog is a tool allowing owners of aerial photography to list details and contact information about individual collections.

By providing this free and open metadata catalog with no commercial interests, the Data Preservation and Archiving Committee (DPAC) aims to provide a definitive metadata resource for all users in the geospatial community to locate previously unknown imagery.

DPAC hopes this Catalog will contribute to the protection and preservation of aerial photography around the world!

ASPRS Members: We Need Your Help!
There are three ways to get involved

- 1**
USE
Use the catalog to browse over 5,000 entries from all 50 states and many countries. Millions of frames from as early as 1924!
- 2**
SUPPLY
Caretakers of collections, with or without metadata, should contact DPAC to add their datasets to the catalog free of charge!
- 3**
TELL
Spread the word about the catalog! New users and data collections are key to making this a useful tool for the community!

For More Details or To Get Involved Contact:

DAVID RUIZ • DRUIZ@QUANTUMSPATIAL.COM • 510-834-2001 OR DAVID DAY • DDAY@KASURVEYS.COM • 215-677-3119

Monocular Video Frame Optimization Through Feature-Based Parallax Analysis for 3D Pipe Reconstruction

Zhijia Xu, Xingzheng Lu, Wenliang Wang, Ershuai Xu, Rongjun Qin, Yiru Niu, Xu Qiao, Feng Yang, and Rui Yan

Abstract

Structure-from-motion (SfM) techniques have been widely used for three-dimensional (3D) scene reconstruction from sequential video frames. However, for reconstructing narrow and confined spaces such as the interior of drainage pipes, selecting geometrically optimal frames is a major challenge, not only to reduce the number of needed frames but also to yield better geometry. This paper introduces a coarse-to-fine method to optimize the selection of monocular video frames based on a geometric criterion called feature-based parallax analysis for 3D pipe reconstruction. The proposed method was applied in two experiments with a monocular camera fixed on a customized robot. Experimental results show that our approach only requires respectively 9.66% and 3.15% of the number of frames. The spatial distribution of the retrieved frames was uniform and reasonable, enabling the successful SfM process to achieve a complete reconstruction of the pipe geometry.

Introduction

Drainage pipes are critical infrastructures for urban water supply and sewage, as a basis of the sustainable development of cities and residents' daily life (Sinha and Karray 2002; Jung and Kim 2017). It is essential to inspect these drainage pipes frequently to identify deteriorations due to aging and rupture to ensure their function properly. Traditional visual inspection is labor-intensive with low efficiency, which does not meet daily maintenance needs. With the rapid development of various sensor levels, measurements from lasers (Zheng and Krys 2012; Lepo *et al.* 2017), ultrasonic (Carballini and Viana 2015; Teixeira *et al.* 2016), and cameras (Su *et al.* 2011; Huang *et al.* 2010) have been used for pipe inspection. Nevertheless, each of these methods comes with varying advantages and drawbacks, either in terms of the sensor cost or computational complexity or robustness.

Zhijia Xu is with the College of Geoscience and Surveying Engineering, and with the State Key Laboratory of Coal Resources and Safe Mining, China University of Mining and Technology (Beijing), Beijing 100083, China (z.xu@cumt.edu.cn).

Xingzheng Lu, Ershuai Xu, and Yiru Niu are with the College of Geoscience and Surveying Engineering, China University of Mining and Technology (Beijing), Beijing 100083, China.

Wenliang Wang is with the CSSC (Zhe Jiang) Ocean Technology Co., Ltd, Zhoushan 316000, China.

Rongjun Qin is with the Department of Electrical and Computer Engineering, The Ohio State University (OSU), Columbus, OH 43210.

Xu Qiao and Feng Yang are with the School of Mechanical Electronic & Information Engineering, China University of Mining and Technology (Beijing), Beijing 100083, China.

Rui Yan is with the Research and Development Center of Beijing Drainage Group Co. Ltd, Beijing 100124, China.

Contributed by Jan Dirk Wegner, September 10, 2021 (sent for review October 27, 2021; reviewed by Kaichang Di, Sagar Deshpande, Jianyu Gu, Hai Huang, Xun Geng, Han Hu).

Structure-from-motion (SfM)-based three-dimensional (3D) reconstruction techniques (Westoby *et al.* 2012) can obtain an accurate and textured geometry of drainage pipes, which provides detailed 3D models for evaluating pipe quality or operational status. Good examples of such work can be found in (Qin and Gruen 2020; Tian *et al.* 2017; Zhang *et al.* 2019). Nevertheless, for drainage pipes within narrow and confined spaces, the collecting geometry through video recording is usually not optimal, such as short baseline, motion blur, and the excessive number of redundant frames from the video. Therefore, a significant challenge is to optimally identify a subset of keyframes for efficient and accurate 3D reconstruction. The optimization is viewed as a decision-making process that considers multiple factors (e.g., conjunction matrix among frames, degree of blur), which are difficult for 3D reconstruction (Dong *et al.* 2014). Existing methods on frame optimization can mainly be classified into three categories, each focusing on different aspects of the optimal data collection: path planning, model prediction, and topological analysis. The path planning method initially uses a “three-step” strategy that collects new images, tests the model accuracy, and then adjusts the camera pose for further image collection (Sakane *et al.* 1991; Yi *et al.* 1995). With a small number of collected images with optimal poses, new images are gradually added to the image set to enhance the completeness and accuracy of the reconstructed point cloud. To this end, genetic algorithm (Olague and Mohr 2002) and fuzzy logic inference methods (Saadatseresht *et al.* 2005) have generally been used. The latter is highly reliable but poorly generalized, resulting in difficulties in formulating the optimization models.

Alternatively, there exist the public availability of data sets (e.g., Karlsruhe Institute of Technology and Toyota Technological Institute (KITTI) (Geiger *et al.* 2013), Densely Annotated Video Segmentation (DAVIS) (Barranco *et al.* 2016), and Carnegie Mellon University (CMU)-MUCC (Fernando *et al.* 2008)) labeled with a large amount of a priori information, and prediction methods which make use of these as examples to learn knowledge from, are increasingly used for keyframe optimization in image-based reconstruction. In this category, Zhao *et al.* (2017) and Rupnik *et al.* (2018) used the matching quality of image features as the loss function for model training to achieve key image preferences with and without the aid of topographic data. Li *et al.* (2020) extracted video keyframes from the first-person view, which projects the multi-modal sensor signals on common space, leading to a set of keyframes with low noise and a significant amount of information, thus improving the coverage of the video sequences.

The topological analysis methods aim to analyze the geometric configurations between conjunct image pairs, e.g., baseline, overlap (Xu *et al.* 2017), intersection angle (Qin 2019), and feature distributions. Gharbi *et al.* (2019) successfully selected keyframes from videos by extracting interest points on candidate frames and then calculated the repeatability values between frames in the form of a directed graph. They performed the keyframe selection by graphical clustering, successfully

Photogrammetric Engineering & Remote Sensing
Vol. 88, No. 7, July 2022, pp. 469–478.
0099-1112/22/469-478

© 2022 American Society for Photogrammetry
and Remote Sensing
doi: 10.14358/PERS.21-00066R3

**PEER-REVIEWED CONTENT
IS ONLY AVAILABLE TO
ASPRS MEMBERS AND SUBSCRIBERS**

**FOR MORE INFORMATION VISIT
MY.ASPRS.ORG**

**PEER-REVIEWED CONTENT
IS ONLY AVAILABLE TO
ASPRS MEMBERS AND SUBSCRIBERS**

**FOR MORE INFORMATION VISIT
MY.ASPRS.ORG**

**PEER-REVIEWED CONTENT
IS ONLY AVAILABLE TO
ASPRS MEMBERS AND SUBSCRIBERS**

**FOR MORE INFORMATION VISIT
MY.ASPRS.ORG**

**PEER-REVIEWED CONTENT
IS ONLY AVAILABLE TO
ASPRS MEMBERS AND SUBSCRIBERS**

**FOR MORE INFORMATION VISIT
MY.ASPRS.ORG**

**PEER-REVIEWED CONTENT
IS ONLY AVAILABLE TO
ASPRS MEMBERS AND SUBSCRIBERS**

**FOR MORE INFORMATION VISIT
MY.ASPRS.ORG**

**PEER-REVIEWED CONTENT
IS ONLY AVAILABLE TO
ASPRS MEMBERS AND SUBSCRIBERS**

**FOR MORE INFORMATION VISIT
MY.ASPRS.ORG**

**PEER-REVIEWED CONTENT
IS ONLY AVAILABLE TO
ASPRS MEMBERS AND SUBSCRIBERS**

**FOR MORE INFORMATION VISIT
MY.ASPRS.ORG**

**PEER-REVIEWED CONTENT
IS ONLY AVAILABLE TO
ASPRS MEMBERS AND SUBSCRIBERS**

**FOR MORE INFORMATION VISIT
MY.ASPRS.ORG**

**PEER-REVIEWED CONTENT
IS ONLY AVAILABLE TO
ASPRS MEMBERS AND SUBSCRIBERS**

**FOR MORE INFORMATION VISIT
MY.ASPRS.ORG**

Monitoring and Analysis of Urban Sprawl Based on Road Network Data and High-Resolution Remote Sensing Imagery: A Case Study of China's Provincial Capitals

Lin Ding, Hanchao Zhang, and Deren Li

Abstract

The primary prerequisite for sustainable urban development is to accurately grasp the development of the city. The dynamic changes in the urban area can reflect the urban expansion process and spatial development model. Carrying out urban expansion monitoring and extracting urban areas is of great importance for grasping the law of urban development and promoting the sustainable development of cities. However, the related research reveals several problems such as insufficient accuracy and low intelligence of urban boundary extraction. In response to these problems, this paper proposes a new method for urban area extraction based on the progressive learning model. By combining prior knowledge and image features, the number of training samples required for machine learning is reduced, and the problem of using high-level semantic information expression in the process of urban areas is avoided by using the classification method, and thus the accuracy of urban area extraction is improved. The method uses urban road network data to divide the city into blocks. It applies the scene classification method to extract the urban areas and uses the pyramid layer-by-layer to carry out the space constraint method to integrate the urban extraction principle into the machine learning process, which can be obtained and kept artificial under a small sample condition. Extracting the effect of the urban area is very close, greatly reducing the workload and providing a new solution for high-precision automatic extraction of urban areas. Through the analysis of urban expansion, the following results were obtained: (1) from 2000 to 2015, China's provincial capital cities maintained a high-speed growth trend with a total area increased by 90%; (2) urban expansion showed significant regional differences. The eastern expansion rate gradually slowed down, the western and northeast regions accelerated their expansion, and the central region expanded steadily; (3) 61% of the provincial capital cities expanded exponentially; (4) the development of China's provincial capital cities was highly correlated with national urban development policies and regional development strategies.

Introduction

Rapidly developing cities have caused dramatic changes in the surrounding environment by transforming ecological land into living and production land. How to quickly and accurately monitor urban expansion is of great significance for future urban planning, land management, and ecological environmental protection. The emergence of satellite technology in the 1960s made the use of remote sensing data for

urban expansion monitoring and research. Satellite remote sensing data become the main information source for urban expansion research.

In the early days, Moderate Resolution Imaging Spectroradiometer (MODIS) (Bartholome and Belward 2005; Costa *et al.* 2016; Friedl *et al.* 2002; Wan *et al.* 2015) and Landsat series imagery (Angiuli and Trianni, 2013; Bagan and Yamagata, 2012; Gao *et al.* 2012; Guindon *et al.* 2004; Son and Chen 2012; Sun *et al.* 2017; Wang *et al.* 2012; Shao *et al.* 2019a; Shao *et al.* 2019b) were the main data sources in urbanization monitoring. However, there are some problems, such as pixel mixture and precision validation (Bicheron *et al.* 2011; Deng and Wu 2013; Li *et al.* 2015; Mayaux *et al.* 2006). With the rapid development of remote sensing technology, the spatial resolution of remote sensing images continues to increase, and many scholars have begun to study how to use high-resolution images to automatically extract urban areas (Chao *et al.* 2010; Chen *et al.* 2013; Lin and Ning 2017; Ni *et al.* 2017; Ning and Lin 2017). However, most of the methods are not suitable for application; they are mainly in the experimental stage at the city scale. The existing urban area extraction based on a high spatial resolution remote sensing image adopts the object-oriented image processing method; that is, the image is first segmented to obtain the unit object, and then the classification criterion is established according to the object (Lu *et al.* 2011). A multi-agent segmentation and classification algorithm is proposed to introduce the shape information of the object and improve the extraction precision (Zhou *et al.* 2010). Hu and Weng use the fuzzy classification method and the high-resolution remote sensing images to extract the object-level urban area, and high extraction precision is obtained (Hu and Weng 2011). The idea of hierarchical classification is adopted for urban extraction (Li *et al.* 2011; Liu *et al.* 2013). Sirmacek and Unsalan propose an unsupervised urban automatic extraction method (Sirmacek and Unsalan 2010). In this method, the local feature points are extracted by Gabor filtering, and then the urban area is obtained by spatial voting. A method of bottom-up and top-down integration iteration for urban land cover and functional area extraction is proposed by Zhang *et al.* (Zhang *et al.* 2018). The method integrates the hierarchical semantic cognitive model and the reverse hierarchical semantic cognitive model through low levels. The combination of spectral, textural, and geometrical features with high-level regional categories, spatial patterns, and other human prior knowledge, first makes multi-level segmentation, uses the hierarchical semantic cognitive model for bottom-up classification, and then makes the reverse segmentation. The layer-based semantic cognition model performs top-down classification and then iterative optimization, which significantly improves the extraction precision. It proves the effectiveness of combining top-level human prior knowledge with the underlying image features to improve the accuracy of urban extraction.

Lin Ding and Deren Li are with the School of Remote Sensing and Information Engineering, Wuhan University, Wuhan 430079, China (dinglin@whu.edu.cn).

Hanchao Zhang is with Key Laboratory of Natural Resources Monitoring in Tropical and Subtropical Area of South China, Ministry of Natural Resources, Beijing 100830, China; the Institute of Photogrammetry and Remote Sensing, Chinese Academy of Surveying and Mapping, Beijing 100830, China.

Contributed by Zhenfeng Shao, January 20, 2022 (sent for review February 9, 2022; reviewed by Weixun Zhou, Min Chen).

Most of the methods are based on artificial features. However, the design of artificial features is difficult, which is hard to cope with in the complicated situations in urban areas. In recent years, more and more scholars have begun to use deep learning methods for urban extraction (Taha and Sharawi 2018; Cheng *et al.* 2021; Wang *et al.* 2022). Khelifa *et al.* proposed a new method (Khelifa *et al.* 2017). Firstly, the image is subpixel segmented, and then the pretrained Convolutional Neural Networks (CNN) are used to extract the depth features. Finally, the random forest is used to classify the urban and nonurban areas, and the results are obtained. He *et al.* used night-time lighting data, normalized difference vegetation index (NDVI), surface temperature, and other data and a full convolutional neural network to monitor the global urban expansion. The overall accuracy reached 90.9% and the kappa coefficient was 0.47, which achieved good results (He *et al.* 2019).

The use of deep learning for urban extraction is accurate and effective but requires a large number of labeled samples for training to have a good effect. Small, sample machine learning methods based on fine-tuning networks, based on distance metrics such as twin networks, matching network (Snell *et al.* 2017; Vinyals *et al.* 2016), prototype network (Snell *et al.* 2017), graph-based neural networks (Garcia and Bruna 2017), recursive memory models based on meta-learning (Santoro *et al.* 2016), and optimizer learning and model independent adaptation (Finn *et al.* 2017). However, these models do not include prior knowledge information, and are difficult apply in urban extraction, and the accuracy is low. The best of the five categories and five samples is 68.2%. Therefore, a deep learning method that can

be operated under the conditions of a small number of samples is developed, and it is an urgent need to further improve the accuracy by adding prior knowledge and artificial features.

In this paper, a semi-automated extraction methods of urban areas with computer automatic recognition and manual interpretation based on road network data and high-resolution imagery was proposed. The urban boundaries of China's 31 provincial capitals in year 2000, 2005, 2010, and 2015 were extracted by using high-resolution images under the unified standard. Then the results of the urban areas were compared with other products to assess the accuracy. At last, urban areas were used as the representation of "land" urbanization to carry out the urban spatiotemporal sprawl analysis.

Study Area and Data

Study Area

In this study, 31 provincial capitals, including municipalities directly under the central government, were selected. The provincial capital cities are the aggregation of resource in provinces and play a leading role in the development of the whole province, which has certain representativeness in the national urban development in recent years. The distribution of provincial capitals in the four major regions is shown in Figure 1.

Data Preparation

High-resolution remote sensing images and China's first national geo-information survey data were collected for urban area extraction and



Figure 1. Study area.

urban sprawl analysis. Remote sensing images with the resolution better than 2 meters were geometrically corrected and projected onto the CGCS2000 coordinate system, which were obtained from the Surveying and Mapping Department. China's first national geo-information survey data includes urban road network data, geographical name and address data, township-level, and county-level administrative divisions. This data provides an important reference for urban area extraction. Table 1 shows remote sensing data used in this research.

The Definition of Urban Area

Based on many previous studies, the concept of "urban area" is proposed in this paper. The urban area is a concentrated and contiguous spatial range within the administrative boundary, based on the location of the government, with urban functions and landscape features (including housing construction areas, structures, urban roads, urban green spaces, urban water areas, etc.), including the central area of the city: residential areas with urban public facilities and urban landscape characteristics, as well as large communities, colleges and universities, scientific research institutions, high-tech development zones, industrial and mining land, etc.

Compared with the urban area defined under the condition of medium-resolution and low-resolution remote sensing images, this paper takes into account more urban landscape and functional characteristics. Compared with the built-up area, it focuses more on objectively reflecting the development of the city from the perspective of remote sensing monitoring.

Method

A new method of urban area extraction based on the progressive learning model is proposed. By combining prior knowledge and image features, the number of training samples required for machine learning is reduced. The method uses urban road network data to divide the city into blocks, the scene classification method to extract the urban area, and the layer-by-layer pyramid to apply the space constraint method in integrating the urban extraction principle into the machine learning process, which can be obtained artificially under a small sample condition. The workflow of the proposed method is shown in Figure 2.

Image Segmentation and Refinement Based on Road Network Data

The image data is segmented according to the road network data to generate an image for machine learning scene classification. For the mixed elements of urban fringe areas that are difficult to be distinguished between urban and nonurban areas, the watershed algorithm is used to segment the images to form multiple image blocks containing only urban or nonurban features.

The basic idea is to treat the image as DEM. The size of the gray scale on the image represents the elevation of the point. The image is segmented by simulating the water harvesting process. The watershed algorithm is generally divided into two steps of sorting and submerging, which is an iterative process. The watershed algorithm can deal with various image segmentation problems, but it is more prone to over-segmentation. In practice, the gradient image is often limited by the threshold to achieve excessive segmentation caused by small changes in gray value, and an appropriate segmentation region is obtained.

Initial Urban Sample Selection

The selection of the initial samples of the urban area mainly refers to the point geography unit data BUCP, the planar geographic unit

data BUCA layer, the BERA layer, the LCTL layer in the national first national census results, and the 2016 basic geographical situation monitoring results data. The scope of the government agency and the development zone is obtained, and the images obtained by the segmentation of the road network are spatially superimposed to obtain initial urban samples.

CNN Scene Classification with Artificial Features

Convolutional neural network is a kind of deep learning method that has been developed in recent years and has attracted extensive attention. It is most commonly used for visual image analysis, and it has a good performance for the recognition and classification of large images. This article uses the basic LeCun-Net5.

The convolutional neural network can automatically extract machine features from images, convert artificial features into image distribution rules, generate artificial feature, add images, and input them as convolutional neural network training samples, which can achieve the combination of the two. The specific method is as follows:

1. Calculate artificial features of the samples. Some features require road network data in the calculation. Some features were obtained

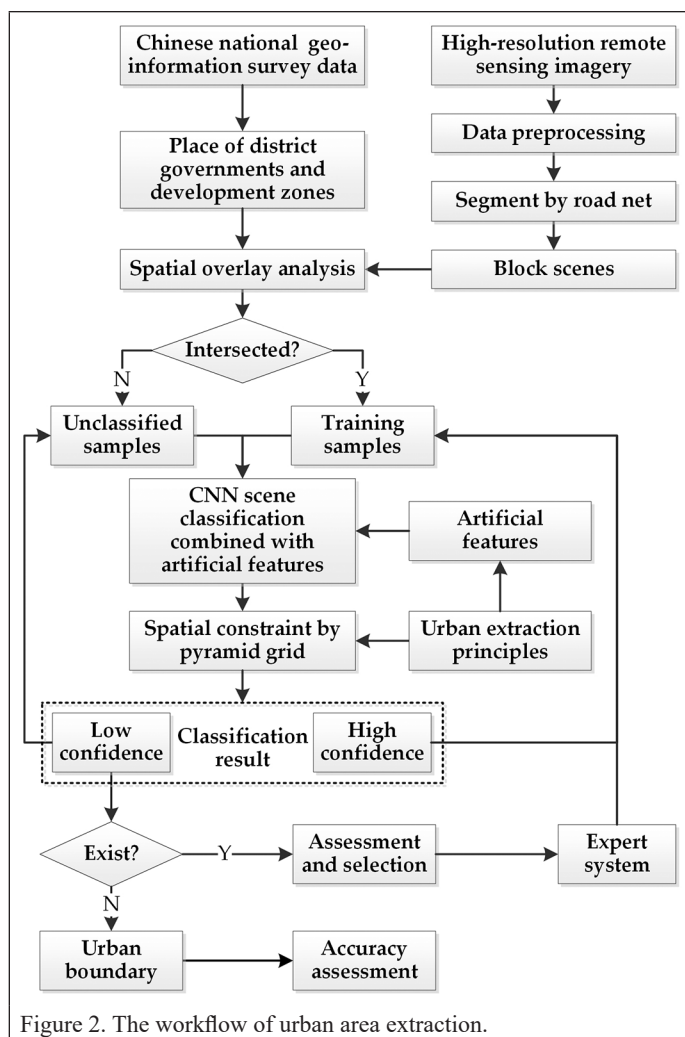


Table 1. The remote sensing data.

Year	Type of the Data (Resolution Unit: Meter)
1	2000 Aerial images (1), IKONOS (1)
2	2005 Quickbird (0.61), Aerial images (1), IKONOS (1), SPOT5 (2.5)
3	2010 Worldview-1 (0.5), Worldview-2 (0.5), Quickbird (0.61), Aerial images (1), SPOT5 (2.5), ALOS (2.5), CIRS-P5 (2.2)
4	2015 Worldview-1 (0.5), Worldview-2 (0.5), Pleiades (0.5), Aerial images (0.5), SPOT-6 (1.5), SPOT-7 (1.5), Mapping Satellite-I (2), ZY-3 (2.1)
Ratio	Worldview-1/2 (26.52%), Aerial images (22.34%), IKONOS (18.87%), Others (32.37%)

separately for each band and normalized. The normalization method selects the maximum and minimum values.

2. Generate a single-band image of the same size as the image sample.
3. The generated single-band image is evenly divided into blocks. Each block needs to be square, and the number of blocks needs to exceed the number of artificial features.
4. The calculated artificial features are sequentially filled into the respective blocks of the newly generated single-band image.
5. Add the single-band image containing artificial features to the original image and input as a new image.
6. Perform conventional convolutional neural network training and classification.

Pyramid Grid Space Constraint

The traditional urban extraction method ignores the spatial distribution information between the urban interior features, making the extraction results fragmented and scattered. In order to overcome its shortcomings, this paper proposes a pyramid grid space constraint method, which further verifies and constrains the classification results by judging the patches and grid classification results around the patches in the urban area, and successfully determines the most critical concentration in urban judgment. The contiguous principle is integrated into it. Specifically, it can be divided into the following steps:

1. The city is divided by the method of space pyramid. The level of the pyramid is recorded as $1 = B, B - 1, B - 2, \dots, U - 2, U - 1, U$. (B is the bottom of the pyramid, which is the lowest layer; U is the top of the pyramid, which is the highest layer.) The pyramid needs to cover the entire administrative division of the city. The size of the grid can be set to a specific value according to the specific conditions of the city. The setting of the highest layer is generally less than one third of the urban area.
2. After determining the pyramid structure, according to the coordinates of the middle point of the block image segmented by the road network, it is distributed to the specific grid unit of each layer to store the information.
3. Mark the category of the pyramid grid from the upper layer to the bottom layer according to the classification result of the image. First, mark the top grid type of the pyramid. If the image categories accessed by the pyramid grid are all urban, mark the category of the grid as urban, and vice versa; if there are mixed categories, record as uncertain; then for the already marked grid, the categories of all the lower level of the grid needs to be consistent with the upper layer; the mixed area is further refined according to the rules of the mark.
4. Correct the marking result according to the principle of centralized contiguous images. Judging from the upper level to the bottom level, if a grid is a nonurban area and the surrounding grid is all urban areas, the grid is considered to be incorrectly marked and corrected; otherwise, if the grid is an urban area, it is first determined whether it contains the initial urban area samples. If it is included, it will not be corrected. If it is not, it will be corrected to a nonurban area according to the rules. If there is both nonurban grid and urban grid around it, calculate and record its label

probability by quantity, and the labels of the surrounding meshes that are undefined are recorded as unknown meshes, and the mesh categories of all the edges of the lower layer are updated according to the correction results.

5. Make confidence evaluation and sample screening. The mark of the samples belonging to the inside of the mesh is updated according to the markup result of the mesh, and the internal sample mark of the mesh of the undetermined mark is unchanged. The inner samples of the mesh surrounded by the same type of mesh are added to the training samples set as high confidence samples and final tagged results. The others are low-confidence samples, and the samples with similar probability of two categories in the unknown grid are screened out and provided to the experts for further confirmation of the labels.
6. Iterative training and classification until all the sample categories are determined.

Accuracy Evaluation

The artificially extracted high-precision urban boundary is selected as the true value, and the accuracy of the quantitative extraction of the extraction results is verified. The accuracy of the overall classification accuracy, misclassification error, missing error, and Kappa coefficient based on the confusion matrix is mainly used for accuracy evaluation. In addition, in the classification experiment of the municipal area, because the nonurban area is often much larger than the urban area, the imbalance of sample distribution and the low misclassification rate of nonurban areas can easily lead to the high overall classification accuracy. In order to objectively reflect the results of urban extraction, this paper adds relative error as an indicator of the accuracy.

Result and Discussion

Accuracy Assessment of Results

The accuracy evaluation results of Beijing, Xining, Lanzhou, and Kunming are shown in Table 2. Using the high-resolution remote sensing image and the national survey results in the above experimental areas, the urban vector is extracted as the true value by artificial delineation. Comparing the two results for qualitative analysis, Figure 3 shows the results of this method and the true value of the urban area. It can be seen from the results in the figure that the extraction results of this method are highly consistent with the spatial shape of the artificial extraction results. The extracted urban areas are concentrated and contiguous without obvious scattered areas. The initial results of urban areas only using segmentation results by the road network are slightly larger than the manual extraction results. The main reason is that many houses around the urban area are built on both sides of the road, while the outer edge of the houses has no road network data. The results of the road network segmentation include both urban building information and nonurban areas such as cultivated land, forest land, and grassland, which are equivalent to mixed pixels in remote sensing classification. However, there are some unavoidable errors in the rough classification results by giving a label in progressive learning scene classification. The solution is to perform “de-mixing” on the object scale; that is, using the segmentation algorithm to segment the

Table 2. Experimental result accuracy evaluation.

City	Result	Training Samples	Total Samples	OA	Commission Errors	Omission Errors	Kappa	Relative Error
Beijing	Initial extraction	974	10 738	98.54%	18.23%	0.87%	0.89	21.23%
	Refinement		10 847	98.59%	17.73%	0.72%	0.89	20.68%
Kunming	Initial extraction	897	9678	97.03%	16.87%	7.02%	0.86	11.85%
	Refinement		10 926	97.41%	14.61%	6.65%	0.88	9.33%
Lanzhou	Initial extraction	645	1082	95.05%	19.69%	10.88%	0.82	10.97%
	Refinement		1118	95.45%	19.38%	7.99%	0.83	14.12%
Xining	Initial extraction	574	1990	94.61%	14.98%	9.84%	0.84	6.05%
	Refinement		2023	96.46%	12.15%	3.56%	0.90	9.77%

road network unit with both urban and nonurban features, and obtain the unit containing only urban or nonurban features, and then proceed scene classification, and finally get the urban extraction results. According to the results of this idea, the segmentation of the hybrid road network unit in the urban area can further improve the urban extraction results, and the degree of improvement is closely related to the detailed level of the road network.

The evaluation results in Table 2 show that the accuracy of the urban area extracted by the method is accurate. The average overall classification accuracy is above 95%, the misclassification error is less than 20%, the omission error is less than 10%, and the Kappa coefficient is above 0.8, indicating that the results of this paper are highly consistent with the artificial extraction results, and the relative errors are also kept below 15%, except Beijing. Compared with the initial extraction results, the refined results have a certain degree of improvement, and the relative reduction of the omission error is relatively helpful. The main reason is to reduce the probability of missing buildings in urban fringe. Table 2 shows that the results of the initial extraction in Beijing are the least improved. The reason is that the road network system in Beijing is very precise, and the proportion of mixed road network units is small, so the improvement effect is the least obvious.

Urban Spatiotemporal Sprawl Process Analysis

In the past 15 years, the average expansion area of China's provincial capital cities was 189.62 km². The average expansion area of the three periods is 54.76 km², 69.14 km², and 65.72 km², respectively. The expansion speed generally shows a trend of increasing first and then decreasing. Overall, the provincial capital city in the eastern part of China has the largest average area, followed by the northeast and the western region, indicating that the provincial capital of eastern China

has the highest level of development, and the western region needs further development. The expansion rate and the expansion strength are calculated by time-sharing, subcity, and subregion, and the specific expansion of each provincial capital is obtained and combined with the analysis of the area distribution of the provincial capital cities.

From the perspective of expansion speed, the average expansion rate of the provincial capital cities in the eastern region is the fastest, but the expansion speed is gradually decreasing; in the west, the average expansion rate is slowing down, but the expansion speed is on the rise; the northeast region is similar to the west, and the expansion speed is also rising; while the central region shows a trend of rising first and then decreasing, and the expansion speed is the smallest among the four regions. In terms of cities, Shanghai has the fastest expansion, with an expansion area of 760.44 km². Six of the top ten cities in the expanded area are located in the eastern region, namely Shanghai (760.44 km²), Tianjin (594.52 km²), Hangzhou (368.2 km²), Nanjing (258.8 km²), Guangzhou (255.19 km²), and Beijing (241.89 km²), indicating that the eastern cities are developing rapidly. There are Chongqing (447.47 km²) and Chengdu (415.92 km²) in the western region, Xi'an (324.75 km²) in the central region, and Shenyang (253.05 km²) in the northeast. In contrast, cities in the eastern region are the fastest growing, and other regions need further development.

Table 3 shows the urban expansion result of China's provincial cities from 2000 to 2015. From the perspective of expansion intensity, from 2000 to 2015, the expansion intensity of the western region was the largest. In 2015, the expansion ratio was 136.87% compared with that of 2000. The expansion intensity in the eastern region was the smallest, and the expansion ratio was only 75.76%. The expansion strength of the northeast region and the central region has not changed too much, but the central region's expansion ratio is only 74.69%. In terms of

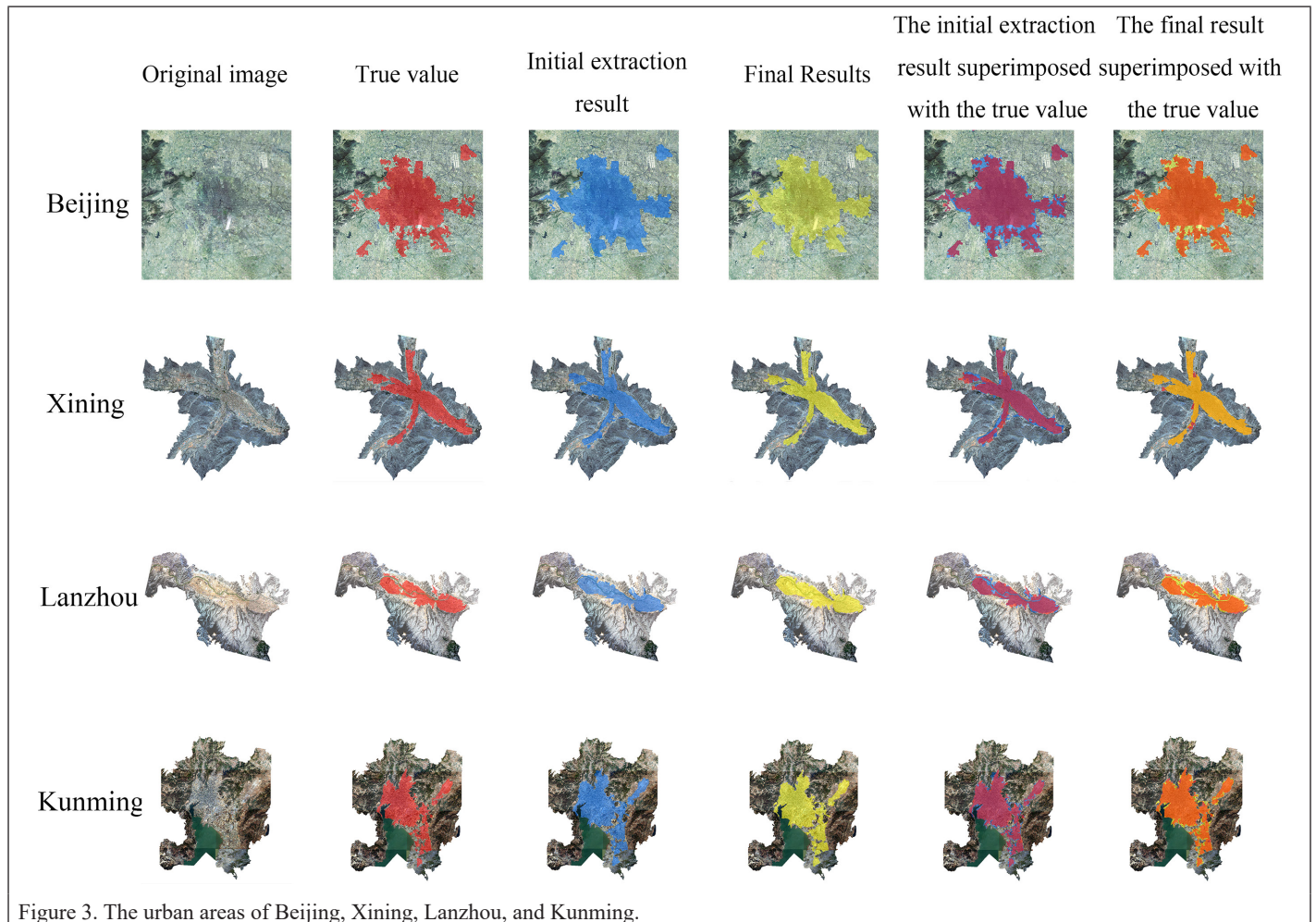


Figure 3. The urban areas of Beijing, Xining, Lanzhou, and Kunming.

Table 3. The urban expansion result of China's provincial cities from 2000 to 2015.

City	Urban Sprawl Speed				Urban Sprawl Intensity, %			
	2000–2005	2005–2010	2010–2015	2000–2015	2000–2005	2005–2010	2010–2015	2000–2015
Beijing	16.00	23.25	9.13	16.13	2.02	2.67	0.92	2.04
Shanghai	58.20	59.03	34.85	50.70	7.39	5.47	2.54	6.44
Tianjin	55.30	29.01	34.60	39.63	10.53	3.62	3.66	7.55
Guangzhou	27.46	16.95	6.62	17.01	6.14	2.90	0.99	3.80
Wuhan	12.40	14.33	12.31	13.01	3.79	3.68	2.67	3.97
Shenyang	14.69	14.75	21.17	16.87	5.15	4.11	4.90	5.91
Chongqing	20.26	33.52	35.72	29.83	8.52	9.89	7.05	12.55
Nanjing	18.18	15.90	17.68	17.25	8.33	5.14	4.55	7.91
Chengdu	11.13	16.08	55.98	27.73	5.40	6.14	16.36	13.46
Urumqi	2.53	11.27	21.00	11.60	1.26	5.27	7.77	5.76
Xi'an	13.66	20.91	30.38	21.65	6.92	7.88	8.21	10.97
Jinan	4.16	4.12	5.83	4.70	2.12	1.90	2.45	2.39
Hangzhou	20.91	39.60	13.14	24.55	10.72	13.22	2.64	12.59
Changchun	7.83	10.56	11.26	9.88	4.29	4.76	4.10	5.42
Shijiazhuang	2.60	0.75	2.45	1.93	1.44	0.39	1.24	1.07
Taiyuan	4.88	4.97	3.43	4.43	2.72	2.44	1.50	2.47
Zhengzhou	3.11	13.42	6.59	7.71	1.87	7.36	2.64	4.62
Harbin	6.87	10.08	12.62	9.86	4.57	5.46	5.37	6.56
Changsha	0.83	10.79	3.78	5.13	0.65	8.13	2.02	3.99
Kunming	2.13	15.50	6.81	8.15	1.85	12.33	3.35	7.08
Lanzhou	1.57	1.80	3.91	2.43	1.59	1.68	3.38	2.45
Hefei	11.65	10.70	8.98	10.44	11.85	6.84	4.27	10.63
Nanning	2.35	13.53	8.75	8.21	2.53	12.94	5.08	8.84
Fuzhou	2.48	2.98	2.32	2.59	2.76	2.91	1.98	2.88
Hohhot	4.74	4.45	4.99	4.73	5.45	4.02	3.75	5.43
Haikou	1.50	4.00	2.31	2.60	1.99	4.84	2.25	3.46
Nanchang	3.21	10.86	9.32	7.80	4.32	12.03	6.44	10.50
Guiyang	0.93	4.78	2.97	2.89	1.70	8.08	3.58	5.31
Yinchuan	4.17	6.34	12.42	7.65	8.41	9.00	12.15	15.41
Xining	3.61	3.38	5.64	4.21	8.74	5.70	7.40	10.20
Lhasa	0.16	1.07	0.49	0.57	0.41	2.67	1.07	1.46

cities, Yinchuan is the most expanding city in China's capital cities, with 15.41%, among the top ten provincial capital cities in terms of expansion intensity, Yinchuan, Chengdu, Chongqing, Xining, and Nanning in the west, Hangzhou and Nanjing in the east, Xi'an, Hefei, and Nanchang in the central region, and no cities in the eastern region. Overall, between 2000 and 2015, urban development in the western region were at a low level, but the relative growth was the fastest, while the eastern region had the highest starting point, but the relative growth was the slowest, with the central region and the northeast region being centered.

In summary, the average expansion area of the provincial capital cities in the eastern region is the largest, but the expansion intensity is the smallest. and the expansion speed is decreasing; the western region is just the opposite, the expansion intensity is the largest, and the average expansion area is the smallest, and the expansion speed is rising; the northeast region with the type of western region, the expansion speed is gradually increasing, and the expansion strength ranks second. The expansion speed of the central region is first rising and then decreasing, and the average expansion intensity and expansion area are the smallest. The above situation shows that between 2000 and 2015, the eastern part of China has the highest starting point for urban development, but the urban space expansion is gradually slowing down,

gradually shifting to intensive conservation, while the western region has the lowest starting point and is currently accelerating development. The northeast region is in the same type with western region, while the provincial capital cities in the central region have encountered certain bottlenecks in the development process.

Relationship between Urban Sprawl and Regional Development Policies

To a certain extent, the research results reflect the implementation of major strategies such as the country's coastal economic development strategy, the development of the western region, the rise of the central region, the revitalization of the northeast, and the national central city planning.

The economic development strategy of coastal areas was proposed during the period of reform and opening up and was one of the earliest regional strategies to be implemented. Under the influence of the economic development strategy of the coastal areas, the eastern region of China has taken the lead in accelerating development and has become the earliest and best-developed region among the four major regions of China. The analysis results show that the average urban area and expansion area of the provincial capital cities in the eastern region far exceed those of other regions, indicating that the economic development strategy of the coastal areas has achieved extremely significant results. At the same time, with the implementation of other regional strategies

and the improvement of the development of eastern cities, after 2005, the expansion of provincial capital cities in the eastern region gradually slowed down and began to develop towards intensive conservation.

The strategy for the development of the western region began in 2000. Since 2000, the expansion rate of the western provincial capitals has been steadily rising. The expansion rate in 2010–2015 is the largest, which is consistent with the strategic development stage of the western development.

The strategy for the rise of Central China was proposed and implemented in 2004. The analysis results in this chapter show that from 2005 to 2010, the speed of urban expansion in central China has increased significantly compared to 2000–2005, indicating that the implementation of the strategy for the rise of Central China has achieved remarkable results. At the same time, however, there has been a certain decline since 2010, indicating that there are still some difficulties in the rise of the central region that need to be further resolved (Table 4).

The strategy of revitalizing the Northeast and the strategy of the rise of the Central China were almost simultaneously proposed. After that, the expansion rate of the capital cities in the Northeast region with regional and resource advantages has also been greatly improved, indicating that the strategy of revitalizing the Northeast has also achieved good results.

The first five central cities in China are Beijing, Shanghai, Tianjin, Guangzhou, and Chongqing. Among the five cities, Beijing, Shanghai, Tianjin, and Guangzhou have been the four largest provincial capital cities in China. Chongqing closely follows. Later, in 2010, it surpassed Wuhan to become the fifth largest provincial capital city in China. This result is highly consistent with the names of the five national central cities initially identified in China. Among the four national central cities that have been added, Zhengzhou is also ranked in the top ten, which confirms that the results of this study can play an important reference role in national urban system planning.

Conclusion

In this study, a semi-automated method of urban area extraction with automatic recognition and manual interpretation by using high-resolution images was proposed. A series of standard rules and processes was proposed to guarantee the consistent and comparative result of urban area. Using this method, a set of consistent and high-precision urban boundaries of China's provincial capitals in year 2000, 2005, 2010, 2015 were obtained. Compared with other urban area products, the results in this study have the highest accuracy.

Based on the urban area and other reference data, urban sprawl was measured with analysis indicators. The results can be concluded as follows:

Table 4. National regional strategy and characteristics of urban regional change.

National Regional Strategy	Implementation Time	Main Characteristic
Coastal Economic Development Strategy	1988	Since 1988, both urban area and expansion area of the provincial capital cities in the eastern region have far exceeded other regions
Western Development Strategy	2000	Since 2000, the expansion rate of western provincial capital cities has steadily increased
Central Rise Strategy	2004	In 2005–2010, cities in central China expanded rapidly, and expansion slowed after 2010
Revitalizing the Northeast Strategy	2004	After 2005, the speed of expansion of provincial capital cities in Northeast China has increased significantly
National Central City Strategy	2010	The first batch of five national central cities are ranked in the top five, and currently eight of the nine national central cities are ranked in the top ten

1. In 2015, the total urban area of China's provincial capitals was 12 398.3 km². From year 2000 to 2015, the total urban area increased by 90.0%. Urban sprawl intensity of provincial capitals in West China was higher than that in other regions, and East China had the lowest urban sprawl intensity.
2. Beijing, Shanghai, Tianjin, and Guangzhou have consistently been the top four of urban areas from 2000 to 2015. In 2015, Chongqing became the fifth largest city. The result reaches a high degree of consistency with the first five national central cities.
3. From year 2000 to 2015, China's provincial capitals tended to be intensive from aspects of gross domestic product per urban area and urban morphology change.
4. From year 2000 to 2015, China's provincial capitals faced the double disharmony between urban sprawl rate and urban population growth rate. Provincial capitals in East China lagged behind urban population growth rate generally. Provincial capitals in Northeast China and Central China were ahead of urban population growth rate generally.
5. From year 2000 to 2015, cultivated land, which occupied 60.6% of the total urban sprawl areas of China's provincial capitals, was the major source of urban sprawl areas. Construction land, which occupied 27.1% of the total urban sprawl area, was the second major source of urban sprawl areas.

The future work will include: 1) the optimization of the algorithms, and the transformation of manual interpretation rules into a machine learning algorithm to improve the efficiency of urban area extraction; and 2) the application of the high precision urban area product of China's provincial capitals to government and public areas by integrating thematic data.

Acknowledgments

This work was supported in part by the National Natural Science Foundation of China under Grants 42090012, in part by the Key Laboratory of Natural Resources Monitoring in Tropical and Subtropical Area of South China, Ministry of Natural Resources (No.2022NRMZ01); 03 special research and 5G project of Jiangxi Province in China (20212ABC03A09); Zhuhai industry university research cooperation project of China (ZH22017001210098PWC); Sichuan Science and Technology Program (2022YFN0031) and Zhizhuo Research Fund on Spatial-Temporal Artificial Intelligence (Grant No.ZZJJ202202).

References

- Angiuli, E. and G. Trianni. 2013. Urban mapping in landsat images based on normalized difference spectral vector. *IEEE Geoscience & Remote Sensing Letters* 11:661–665.
- Bagan, H. and Y. Yamagata. 2012. Landsat analysis of urban growth: How Tokyo became the world's largest megacity during the last 40 years. *Remote Sensing of Environment* 127:210–222.
- Bartholome, E. M. and A. S. Belward. 2005. GLC2000: A new approach to global land cover mapping from Earth observation data. *International Journal of Remote Sensing* 26:1959–1977.
- Bicheron, P., P. Defourny, C. Brockmann, L. Schouten, C. Vancutsem, M. Huc, S. Bontemps, M. Leroy, F. Achard and M. Herold. 2011. GLOBCOVER: Products description and validation report. *Foro Mundial De La Salud* 17:285–287.
- Chao, T., Y. Tan, H. Cai, D. U. Bo and J. Tian. 2010. Object-oriented method of hierarchical urban building extraction from high-resolution remote-sensing imagery. *Acta Geodaetica et Cartographica Sinica* 39:39–45.
- Chen, H., C. Tao, Z. Zou and F. Yu. 2013. Automatic urban area extraction using a Gabor filter and high-resolution remote sensing imagery. *Geomatics and Information Science of Wuhan University* 38:1063–1067.
- Cheng, Q., Y. Xu, P. Fu, J. Li, W. Wang and Y. Ren. 2021. Scene classification of remotely sensed images via densely connected convolutional neural networks and an ensemble classifier. *Photogrammetric Engineering & Remote Sensing* 87(4):295–308.

- Costa, J.N.D., E. Bielecka, B. Calka, J.N.D. Costa, E. Bielecka, B. Calka, J.N.D. Costa, E. Bielecka and B. Calka. 2016. Uncertainty quantification of the global rural-urban mapping project over polish census data. *Environmental Engineering*. <https://doi.org/10.3846/enviro.2017.221>.
- Deng, C. and C. Wu. 2013. A spatially adaptive spectral mixture analysis for mapping subpixel urban impervious surface distribution. *Remote Sensing of Environment* 133:62–70.
- Djerriri, K., R. Adjouj and D. Attaf. 2017. Convolutional neural networks for the extraction of built-up areas from Sentinel-2 images. In *Proceedings the Agile International Conference on Geographic Information Science*, held in Wageningen, the Netherlands, 9–12 May 2017. <https://doi.org/10.48550/arXiv.2006.03267>.
- Finn, C., P. Abbeel and S. Levine. 2017. Model-Agnostic Meta-Learning for Fast Adaptation of Deep Networks. In *Proceedings of the 34th International Conference on Machine Learning*, held in Sydney, Australia. <https://doi.org/10.48550/arXiv.1703.03400>.
- Friedl, M. A., D. K. Mciver, J.C.F. Hodges, X. Y. Zhang, D. Muchoney, A. H. Strahler, C. E. Woodcock, S. Gopal, A. Schneider and A. Cooper. 2002. Global land cover mapping from MODIS: Algorithms and early results. *Remote Sensing of Environment* 83:287–302.
- Gao, F., E. B. De Colstoun, R. Ma, Q. Weng, J. Masek, J. Chen, Y. Pan and C. Song. 2012. Mapping impervious surface expansion using medium-resolution satellite image time series: A case study in the Yangtze River Delta, China. *International Journal of Remote Sensing* 33:7609–7628.
- Garcia, V. and J. Bruna. 2017. Few-shot learning with graph neural networks. In *Proceedings ICLR 2018*, held in Vancouver, BC, Canada. <https://doi.org/10.48550/arXiv.1711.04043>.
- Guindon, B., Y. Zhang and C. Dillabaugh. 2004. Landsat urban mapping based on a combined spectral–spatial methodology. *Remote Sensing of Environment* 92:218–232.
- He, C., Z. Liu, S. Gou, Q. Zhang and L. Xu. 2019. Detecting global urban expansion over the last three decades using a fully convolutional network. *Environmental Research Letters* 14:034008.
- Hu, X. and Q. Weng. 2011. Impervious surface area extraction from IKONOS imagery using an object-based fuzzy method. *Geocarto International* 26:3–20.
- Li, P., J. Guo, B. Song and X. Xiao. 2011. A multilevel hierarchical image segmentation method for urban impervious surface mapping using very high resolution imagery. *IEEE Journal of Selected Topics in Applied Earth Observations & Remote Sensing* 4:103–116.
- Li, X., G. Peng and L. Lu. 2015. A 30-year (1984–2013) record of annual urban dynamics of Beijing City derived from Landsat data. *Remote Sensing of Environment* 166:78–90.
- Lin, X. and X. Ning. 2017. Extraction of human settlements from high resolution remote sensing imagery by fusing features of right angle corners and right angle sides. *Acta Geodaetica et Cartographica Sinica* 46:83–89.
- Liu, C., Z. Shao, M. Chen and H. Luo. 2013. MNDISI: A multi-source composition index for impervious surface area estimation at the individual city scale. *Remote Sensing Letters* 4:803–812.
- Lu, D., S. Hetrick and E. Moran. 2011. Impervious surface mapping with Quickbird imagery. *International Journal of Remote Sensing* 32:2519–2533.
- Mayaux, P., H. Eva, J. Gallego, A. H. Strahler, M. Herold, S. Agrawal, S. Naumov, E.E.D. Miranda, C.M.D. Bella and C. Ordoyne. 2006. Validation of the global land cover 2000 map. *IEEE Transactions on Geoscience & Remote Sensing* 44:1728–1739.
- Ni, H., X. Lin and X. Ning. 2017. A method for extracting human settlements from remote sensing image using right angle corners features. *Wuhan Daxue Xuebao* 42:648–655.
- Ning, X. and X. Lin. 2017. An index based on joint density of corners and line segments for built-up area detection from high resolution satellite imagery. *ISPRS International Journal of Geo-Information* 6:338.
- Santoro, A., S. Bartunov, M. Botvinick, D. Wierstra and T. Lillicrap. 2016. One-shot learning with memory-augmented neural networks. <https://doi.org/10.48550/arXiv.1605.06065>.
- Shao, Z., H. Fu, D. Li, O. Altan and T. Cheng. 2019a. Remote sensing monitoring of multi-scale watersheds impermeability for urban hydrological evaluation. *Remote Sensing of Environment* 232:111338.
- Shao, Z., J. Cai, P. Fu, L. Hu and T. Liu. 2019b. Deep learning-based fusion of Landsat-8 and Sentinel-2 images for a harmonized surface reflectance product. *Remote Sensing of Environment* 235:111425.
- Sirmacek, B. and C. Unsalan. 2010. Urban area detection using local feature points and spatial voting. *IEEE Geoscience & Remote Sensing Letters* 7:146–150.
- Snell, J., K. Swersky and R. S. Zemel. 2017. Prototypical networks for few-shot learning. *Advances in Neural Information Processing Systems*:4077–4087.
- Son, N. T. and C. R. Chen. 2012. Urban growth mapping from Landsat data using linear mixture model in Ho Chi Minh City, Vietnam. *Journal of Applied Remote Sensing* 6:100–106.
- Sun, Z., C. Wang, H. Guo and R. Shang. 2017. A modified normalized difference impervious surface index (MNDISI) for automatic urban mapping from Landsat imagery. *Remote Sensing* 9:942.
- Taha, E. D. and A. Sharawi. 2018. Urban land cover from GF-2 satellite images using object based & neural network classifications. In *Proceedings ICGE 2018: International Conference on Geomatics Engineering*.
- Vinyals, O., C. Blundell, T. Lillicrap, K. Kavukcuoglu and D. Wierstra. 2016. Matching networks for one shot learning. In *Proceedings 30th Conference on Neural Information Processing Systems (NIPS 2016)*, held in Barcelona, Spain. <https://doi.org/10.48550/arXiv.1606.04080>.
- Wan, B., Q. Guo, F. Fang, Y. Su and R. Wang. 2015. Mapping US urban extents from MODIS data using one-class classification method. *Remote Sensing* 7:10143–10163.
- Wang, L., C. C. Li, Q. Ying, X. Cheng and X. Wang. 2012. China's urban expansion from 1990 to 2010 determined with satellite remote sensing. *Science Bulletin* 57:2802–2812.
- Wang, X., Z. Shao, X. Huang, and D. Li. 2022. Spatiotemporal temperature fusion based on a deep convolutional network. *Photogrammetric Engineering & Remote Sensing* 88(2):93–101.
- Zhang, X., S. Du and Q. Wang. 2018. Integrating bottom-up classification and top-down feedback for improving urban land-cover and functional-zone mapping. *Remote Sensing of Environment* 212:231–248.
- Zhou, Y., Y. Wang, A. J. Gold and P. V. August. 2010. Modeling watershed rainfall-runoff relations using impervious surface-area data with high spatial resolution. *Hydrogeology Journal* 18:1413–1423.

WHO'S WHO IN ASPRS

Founded in 1934, the American Society for Photogrammetry and Remote Sensing (ASPRS) is a scientific association serving thousands of professional members around the world. Our mission is to advance knowledge and improve understanding of mapping sciences to promote the responsible applications of photogrammetry, remote sensing, geographic information systems (GIS) and supporting technologies.

BOARD OF DIRECTORS

BOARD OFFICERS

President

Christopher Parrish, Ph.D
Oregon State University

President-Elect

Lorraine B. Amenda, PLS, CP
Towill, Inc.

Vice President

Bandana Kar
Oak Ridge National Lab

Past President

Jason M. Stoker, Ph.D,
U.S. Geological Survey

Treasurer

Stewart Walker, Ph.D.
photogrammetry4u

Secretary

Harold Rempel
ESP Associates, Inc.

COUNCIL OFFICERS

ASPRS has six councils. To learn more, visit <https://www.asprs.org/Councils.html>.

Sustaining Members Council

Chair: Ryan Bowe
Deputy Chair: Melissa Martin

Technical Division Directors Council

Chair: Bill Swope
Deputy Chair: Hope Morgan

Standing Committee Chairs Council

Chair: David Stolarz
Deputy Chair: TBA

Early-Career Professionals Council

Chair: Madeline Stewart
Deputy Chair: Kyle Knapp

Region Officers Council

Chair: Demetrio Zourarakis
Deputy Chair: Jason Krueger

Student Advisory Council

Chair: Lauren McKinney-Wise
Deputy Chair: Oscar Duran

TECHNICAL DIVISION OFFICERS

ASPRS has seven professional divisions. To learn more, visit <https://www.asprs.org/Divisions.html>.

Geographic Information Systems Division

Director: Denise Theunissen
Assistant Director: Jin Lee

Lidar Division

Director: Ajit Sampath
Assistant Director: Mat Bethel

Photogrammetric Applications Division

Director: Ben Wilkinson
Assistant Director: Hank Theiss

Primary Data Acquisition Division

Director: Greg Stensaas
Assistant Director: Srinidhi Dharmapuri

Professional Practice Division

Director: Bill Swope
Assistant Director: Hope Morgan

Remote Sensing Applications Division

Director: Amr Abd-Ehrahman
Assistant Director: Tao Liu

Unmanned Autonomous Systems (UAS)

Director: Jacob Lopez
Assistant Director: Bahram Salehi

REGION PRESIDENTS

ASPRS has 13 regions to serve the United States. To learn more, visit <https://www.asprs.org/regions.html>.

Alaska Region

Cascadia Region

Robert Hariston-Porter

Eastern Great Lakes Region

Michael Joos, CP, GISP

Florida Region

Xan Fredericks

Heartland Region

Whit Lynn

Intermountain Region

Robert T. Pack

Mid-South Region

David Hughes

Northeast Region

North Atlantic Region

Pacific Southwest Region

John Erickson, PLS, CP

Potomac Region

Dave Lasko

Rocky Mountain Region

Western Great Lakes Region

Adam Smith

SUSTAINING MEMBERS

ACI USA Inc.

Weston, Florida
<https://acicorporation.com/>
 Member Since: 2/2018

Aerial Services, Inc.

Cedar Falls, Iowa
www.AerialServicesInc.com
 Member Since: 5/2001

Airworks Solutions Inc.

Boston, Massachusetts
 Member Since: 3/2022

Applanix

Richmond Hill, Ontario, Canada
<http://www.applanix.com>
 Member Since: 7/1997

Ayres Associates

Madison, Wisconsin
www.AyresAssociates.com
 Member Since: 1/1953

CT Consultants

Mentor, Ohio
 Member Since: 3/2022

Dewberry

Fairfax, Virginia
www.dewberry.com
 Member Since: 1/1985

Esri

Redlands, California
www.esri.com
 Member Since: 1/1987

GeoCue Group

Madison, Alabama
<http://www.geocue.com>
 Member Since: 10/2003

Geographic Imperatives LLC

Centennial, Colorado
 Member Since: 12/2020

GeoWing Mapping, Inc.

Richmond, California
www.geowingmapping.com
 Member Since: 12/2016

Half Associates, Inc.

Richardson, Texas
www.half.com
 Member Since: 8/2021

Keystone Aerial Surveys, Inc.

Philadelphia, Pennsylvania
www.kasurveys.com
 Member Since: 1/1985

Kucera International

Willoughby, Ohio
www.kucerainternational.com
 Member Since: 1/1992

L3Harris Technologies

Broomfield, Colorado
www.l3harris.com
 Member Since: 6/2008

Merrick & Company

Greenwood Village, Colorado
www.merrick.com/gis
 Member Since: 4/1995

NV5 Geospatial

Sheboygan Falls, Wisconsin
www.quantumspatial.com
 Member Since: 1/1974

Pickett and Associates, Inc.

Bartow, Florida
www.pickettusa.com
 Member Since: 4/2007

Riegl USA, Inc.

Orlando, Florida
www.rieglusa.com
 Member Since: 11/2004

Robinson Aerial Surveys, Inc.(RAS)

Hackettstown, New Jersey
www.robinsonaerial.com
 Member Since: 1/1954

Sanborn Map Company

Colorado Springs, Colorado
www.sanborn.com
 Member Since: 10/1984

Scorpius Imagery Inc.

Newark, Delaware
aerial@scorpiusimagery.com
 Member Since: 6/2021

Surdex Corporation

Chesterfield, Missouri
www.surdex.com
 Member Since: 12/2011

Surveying And Mapping, LLC (SAM)

Austin, Texas
www.sam.biz
 Member Since: 12/2005

T3 Global Strategies, Inc.

Bridgeville, Pennsylvania
<https://t3gs.com/>
 Member Since: 6/2020

Terra Remote Sensing (USA) Inc.

Bellevue, Washington
www.terraremote.com
 Member Since: 11/2016

Towill, Inc.

San Francisco, California
www.towill.com
 Member Since: 1/1952

Woolpert LLP

Dayton, Ohio
www.woolpert.com
 Member Since: 1/1985

SUSTAINING MEMBER BENEFITS

Membership

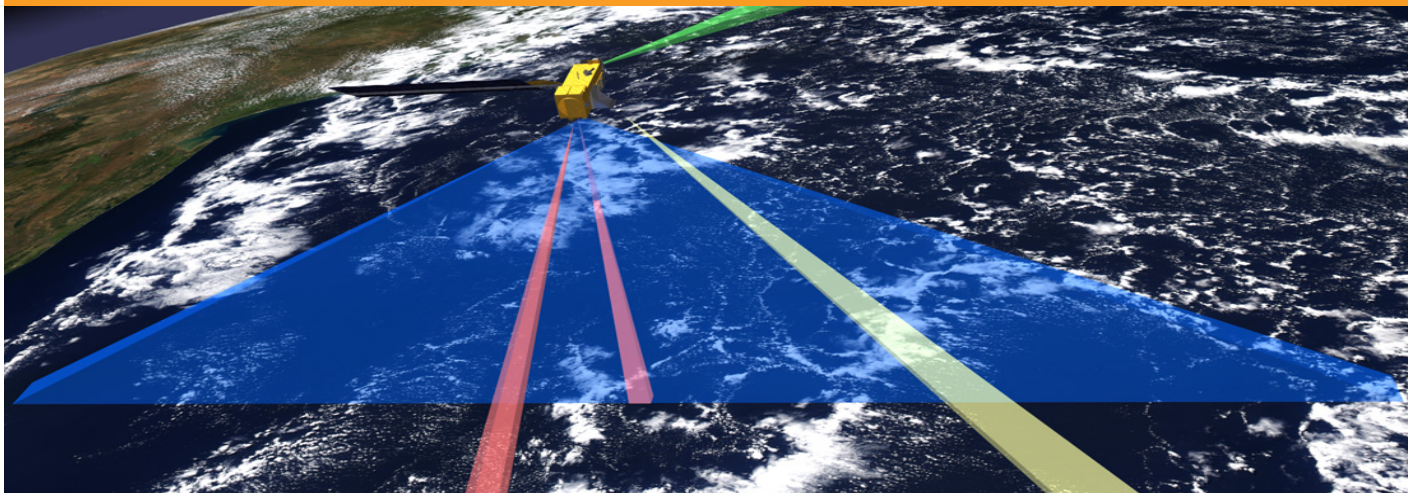
- ✓ Provides a means for dissemination of new information
- ✓ Encourages an exchange of ideas and communication
- ✓ Offers prime exposure for companies

Benefits of an ASPRS Membership

- Complimentary and discounted Employee Membership*
- E-mail blast to full ASPRS membership*
- Professional Certification Application fee discount for any employee
- Member price for ASPRS publications
- Discount on group registration to ASPRS virtual conferences
- Sustaining Member company listing in ASPRS directory/website
- Hot link to company website from Sustaining Member company listing page on ASPRS website
- Press Release Priority Listing in PE&RS Industry News
- Priority publishing of Highlight Articles in PE&RS plus, 20% discount off cover fee
- Discount on PE&RS advertising
- Exhibit discounts at ASPRS sponsored conferences (exception ASPRS/ILMF)
- Free training webinar registrations per year*
- Discount on additional training webinar registrations for employees
- Discount for each new SMC member brought on board (Discount for first year only)

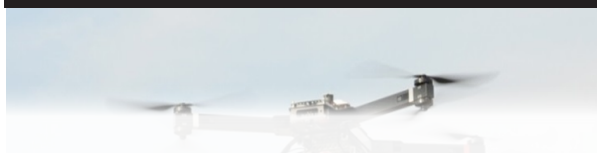
*quantity depends on membership level

The 4th Edition of the *Manual of Remote Sensing*!



MANUAL OF REMOTE SENSING

Fourth Edition



The *Manual of Remote Sensing, 4th Ed.* (MRS-4) is an “enhanced” electronic publication available online from ASPRS. This edition expands its scope from previous editions, focusing on new and updated material since the turn of the 21st Century. Stanley Morain (Editor-in-Chief), and co-editors Michael Renslow and Amelia Budge have compiled material provided by numerous contributors who are experts in various aspects of remote sensing technologies, data preservation practices, data access mechanisms, data processing and modeling techniques, societal benefits, and legal aspects such as space policies and space law. These topics are organized into nine chapters. MRS4 is unique from previous editions in that it is a “living” document that can be updated easily in years to come as new technologies and practices evolve. It also is designed to include animated illustrations and videos to further enhance the reader’s experience.

MRS-4 is available to ASPRS Members as a member benefit or can be purchased by non-members. To access MRS-4, visit <https://my.asprs.org/mrs4>.



edited by: Stanley A. Morain,
Michael S. Renslow and Amelia M. Budge

LEARN
DO
GIVE
BELONG

ASPRS Offers

- » Cutting-edge conference programs
- » Professional development workshops
- » Accredited professional certifications
- » Scholarships and awards
- » Career advancing mentoring programs
- » *PE&RS*, the scientific journal of ASPRS

asprs.org

ASPRS